Spring 2014

3D bioprinting of vasculature network for tissue engineering

Yahui Zhang
University of Iowa

3D BIOPRINTING OF VASCULATURE NETWORK FOR TISSUE ENGINEERING

by

Yahui Zhang

A thesis submitted in partial fulfillment
of the requirements for the Doctor of
Philosophy degree in Industrial Engineering
in the Graduate College of
The University of Iowa

May 2014

Thesis Supervisor: Assistant Professor Ibrahim Tarik Ozbolat

Graduate College
The University of Iowa
Iowa City, Iowa

CERTIFICATE OF APPROVAL

_____

PH.D. THESIS

_____

This is to certify that the Ph.D. thesis of

Yahui Zhang

has been approved by the Examining Committee
for the thesis requirement for the Doctor of Philosophy
degree in Industrial Engineering at the May 2014 graduation.

Thesis Committee: _____
Ibrahim T. Ozbolat, Thesis Supervisor

_____
Andrew Kusiak

_____
Hongtao Ding

_____
Edward Sander

_____
Eric E. Nuxoll

To my parents, Xu Zhang and Ping Yong, for their love, support and encouragement.

ACKNOWLEDGEMENTS

I would never have been able to finish my dissertation without the guidance of my committee members, help from friends, and support from my family.

I would like to express my deepest gratitude to my advisor, Dr. Ibrahim Tarik Ozbolat, for his excellent guidance, caring, and patience, and for providing me with an excellent atmosphere for doing research. I would like to express my deep gratitude and respect to my committee members, Dr. Andrew Kusiak, Dr. Edward Sander, Dr. Eric E. Nuxoll and Dr. Hongtao Ding, whose advice and insight were invaluable to me. I would also like to thank Yin Yu for cell viability and tissue histology tests, and Farzaneh Dolati for mechanical tests. Many thanks to all the workers in the Biomanufacturing Lab for helping me with my experiments. My research would not have been possible without their help.

I would also like to thank my parents. They were always supporting me and encouraging me with their best wishes. Also, I want to thank the National Institutes of Health (NIH) and the Institute for Clinical and Translational Science (ICTS) for providing funding for this project (grant number ULIRR024979).

ABSTRACT

Tissue engineering, with the ultimate goal of engineering artificial tissues or organs to replace malfunctioning or diseased ones inside the human body, provides a substitute for organ transplantation. Driven by the growing, tremendous gap between the demand for and the supply of donated organs, tissue engineering has been advancing rapidly. There has been great success in engineering artificial organs such as skin, bone, cartilage and bladders because they have simple geometry, low cell oxygen consumption rates and little requirements for blood vessels. However, difficulties have been experienced with engineering thick, complex tissues or organs, such as hearts, livers or kidneys, primarily due to the lack of an efficient media exchange system for delivering nutrients and oxygen and removing waste. Very few types of cells can tolerate being more than 200 μm away from a blood vessel because of the limited oxygen diffusion rate. Without a vasculature system, three-dimensional (3D) engineered thick tissues or organs cannot get sufficient nutrients, gas exchange or waste removal, so nonhomogeneous cell distribution and limited cell activities result. Systems must be developed to transport nutrients, growth factors and oxygen to cells while extracting metabolic waste products such as lactic acid, carbon dioxide and hydrogen ions so the cells can grow, proliferate and make extracellular matrix (ECM), forming large-scale tissues and organs. However, available biomanufacturing technologies encounter difficulties in manufacturing and integrating vasculature networks into engineered constructs.

This work proposed a novel 3D bioprinting technology that offers great potential for integration into thick tissue engineering. The presented system offered several advantages, including that it was perfusable, it could print conduits with smooth, uniform and well-defined walls and good biocompatibility, it had no post-fabrication procedure, and it enabled direct bioprinting of complex media exchange networks.

TABLE OF CONTENTS

LIST OF TABLES viii

LIST OF FIGURES ix

CHAPTER

I. INTRODUCTION 1

1.1 Background 2
1.2 Fabrication of Tissue-Engineered Constructs 3
1.3 Bioprinting 5
1.3.1 Bioprinting Technologies 6
1.3.2 Biomaterials for Bioprinting 7
1.4 Alginate and Chitosan as Biomaterial 10
1.5 Fabrication Technologies for Vasculature Network 12
1.6 Thesis Objective and Outline 15

II. FABRICATION OF VASCULAR CONDUITS 17

2.1 Materials and Methods 17
2.1.1 Materials 17
2.1.2 Cell Preparation 18
2.1.3 Fabrication System 18
2.1.3.1 Fabrication Process 19
2.1.3.2 Coaxial Nozzle 20
2.1.4 Cell Viability Analysis 21
2.2 Results 22
2.2.1 Sample Fabrication 22
2.2.2 Cell Viability Analysis 24
2.3 Discussion and Conclusion 27

III. MODELING AND ANALYSIS OF DISPENSING RHEOLOGY 29

3.1 Dispensing through the Coaxial Nozzle 29
3.2 Modeling of Dispensing Rheology 31
3.2.1 Determination of Pressure Gradient 32
3.2.2 Predicted Speed versus Experimental Speed 33
3.2.3 Printed Vasculature Networks 35
3.3 Shear Stress Model for the Coaxial Nozzle 36
3.3.1 Shear Stress Distribution inside the Coaxial Nozzle 38
3.3.2 Cell Viability Distribution over the Cross Section Profile in Conduit 40
3.4 Discussion and Conclusion 43

IV. LAYER-BY-LAYER FABRICATION STRATEGY 46

4.1 Prediction of the Minimum Gelation Time 46
4.2 Pre-printing Plan 48
4.3 Discussion and Conclusion 49

V. CHARACTERIZATION OF INFLUENCES OF FABRICATION PARAMETERS ON CONDUITS 51

5.1 Materials and Methods 51
5.1.1 Materials 51
5.1.2 Fabrication 51
5.1.3 Measurement and Statistical Analysis 52
5.1.4 Fractional Factorial Design 52
5.2. Results 54
5.2.1 Effect of Biomaterial Concentration 54
5.2.2 Effect of Crosslinker Concentration 57
5.2.3 Effects of Dispensing Parameters on Conduit Dimensions 58
5.2.4 Result of Fractional Factorial Design 61
5.2.4.1 Analysis of Conduit Diameter 61
5.2.4.2 Analysis of Wall Thickness 65
5.2.5 Cell Viability as a Function of Dispensing Parameters 69
5.3 Discussion and Conclusion 71

VI. EVALUATION OF MEDIA PERFUSION CAPABILITIES 74

6.1 Materials and Methods 74
6.1.1 Materials 74
6.1.2 Fabrication of Conduits for Perfusion 74
6.1.3 Media Perfusion System 75
6.1.4 Perfusion and Diffusion Characterization 77
6.1.5 Embedding a Vasculature System into Bulk Hydrogel 77
6.1.6 Quantitative Measurement of Diffusion 77
6.1.7 Statistical Analysis 79
6.2. Results 80
6.2.1 Fabrication of Chitosan and Alginate Conduits 80
6.2.2 Media Perfusion Rate Effect on Conduit Dimension 81
6.2.3 Media Perfusion Rate Effect on Conduit Diffusion Rate 82
6.2.4 Perfusion and Diffusion Characterization 84
6.2.5 Quantitative Measurement of Small Molecular Diffusivity 85
6.3. Discussion and Conclusion 87

VII. DEHYDRATION, SWELLING, DEGRADATION, AND MECHANICAL PROPERTIES AND TISSUE HISTOLOGY TEST 92

7.1 Materials and Methods 92
7.1.1 Materials 92
7.1.2 Cell Preparation 93
7.1.3 Dehydration, Swelling, and Degradation Tests 93
7.1.4 Dimensional Characterization of Conduits during Dehydration, Swelling, and Degradation 94
7.1.5 Mechanical Testing 95
7.1.6 Tissue Histology 95
7.1.7 Statistical Analyses 96
7.2. Results 96
7.2.1 Fabrication of Conduits 96
7.2.2 Dehydration, Swelling, and Degradation Tests 97
7.2.3 Dimensional Characterization 103
7.2.4 Mechanical Testing 105
7.2.5 Tissue Histology Testing 106

7.3. Discussion and Conclusion.....107

VIII..... .
SUMMARY, CONCLUSIONS AND FUTURE WORK
RECOMMENDATIONS.....112
2
8.1 Summary and Conclusion.....112
8.2 Future Work Recommendation.....114

REFERENCES 116

APPENDIX A CONDUIT SAMPLE PREPARATION PROCEDURE FOR SEM MICROSCOPY 126

APPENDIX B VALUES OF Λ 128

APPENDIX C MEASUREMENT OF FLOW RATE AND PRESSURE GRADIENT 129

APPENDIX D SHEAR STRESS VALUE OF DIFFERENT LOCATIONS INSIDE COAXIAL NOZZLE TIP.....131

APPENDIX E PRINTING PLAN CALCULATION.....132

APPENDIX F FACTORIAL DESIGN RESULT 134

LIST OF TABLES

Table 1.1 Bioprintable hydrogels....9

Table 3.1 Calculated maximum shear stress for G16-23 and G16-26.....44

Table 5.1 Low and high values of the five factors involved in the bioprinting process....53

Table 5.2 ANOVA table for conduit diameter....62

Table 5.3 ANOVA for the wall thickness....67

Table 7.1 Mechanical properties of conduits....106

Table 8.1 Important criteria to judge an artificial conduit.....114

Table B.1 Values of λ, which locates the position at which the velocity is at its maximum 128

Table C.1 Dispensing rheology: flow rate and pressure gradient of 3% alginate solution....130

Table D.1 Shear stress inside coaxial nozzle (G 16-23) 131

Table F.1 Factorial design result and predicted gelation time 134

LIST OF FIGURES

Figure 1.1 Chemical structure of alginate and chitosan. 11

Figure 2.1 The fabrication system: (a) experimental setup, (b) coaxial nozzle, and (c) a cross-section view of the coaxial nozzle tips. 19

Figure 2.2 Coaxial nozzle unit: (a) 3D model of the coaxial nozzle, (b) cross-sectional view of coaxial nozzle assembly model with fluid flow paths for hydrogel and crosslinker solutions. 21

Figure 2.3 Sample printed structures: (a) a printed conduit allowing media transport shown with a yellow food dye, (b) an image of a single conduit analyzed under a digital microscope, (c) a long vasculature network perfused with cell media, (d) alginate conduit under an SEM microscope, and (e) alginate hydrogel sponge-like structure. 24

Figure 2.4 Representative images of printed samples: (a) light microscopic image shows that cells were uniformly encapsulated, and lumen was clearly identified in the center, (b) an SEM image showing encapsulated cells, and (c) time course of CPC viability after the bioprinting process. Cell viability was analyzed using ImageJ. Each symbol represents the average of the results for three z-projections composed of six planes from confocal laser imaging. The error bars indicate standard deviations (n=3). 26

Figure 2.5 Confocal images showing the lumen: (a-f) z-projection from top to center of a sample, with 50 μm intervals showing the solid wall of samples and the lumen. 27

Figure 3.1 Dispensing process in a coaxial nozzle 30

Figure 3.2 Effect of pressure rate on (a) flow rate and (b)-$\Delta P/L$. 33

Figure 3.3 Predicted speed versus experimental speed with (a) 3% alginate, and (b) 4% alginate (data are mean ± SD, 3 samples). 35

Figure 3.4 Printed vasculature network: (a) a single layer of vasculature network pattern, and (b) eight layers of vasculature network. 36

Figure 3.5 A representative figure of non-Newtonian flow through a coaxial nozzle. 37

Figure 3.6 Dispensing rheology: (A) effect of alginate pressure rate on volume flow rate of 4% alginate solution, (B) effect of pressure rate on -$\Delta P/L$ 39

Figure 3.7 Shear stress inside the coaxial nozzle: (a) shear stress distribution inside the coaxial nozzles, and (b) maximum shear stress with various alginate dispensing pressures. 40

Figure 3.8 Representative figure of cell viability distribution along *r*: (b) a cross-section of conduit, and (c) cell viability distribution along *r*.....42

Figure 3.9 Laser confocal imaging for live/dead staining of the printed structure at 5 psi with G16-23 nozzle: CPCs labeled with calcein AM and ethidium homodimer after cell encapsulation and imaged with confocal laser scanning microscope: (a) quantifiable dead and alive cells; most of the cells that are viable post-printing are seen in live cell channel, and merging both channels shows the relative ratio and location of dead cells and live cells, (b) live and dead cells are fluorescent green and fluorescent red, respectively......43

Figure 3.10 Vasculature networks with spiral shape 45

Figure 5.1 Dimensional comparison of printed conduits per variation in hydrogel concentrations, including: (a) chitosan and (b) alginate (the single asterisk (*) indicates significant differences between groups $p<0.05$).....56

Figure 5.2 Effect of CaCl2 on conduit dimensions (the single asterisk (*) indicates significant differences between groups $p<0.05$).....58

Figure 5.3 Effect of flow rheology on the geometry of conduits: (a) varying alginate dispensing rate, and (b) varying $CaCl_2$ dispensing rate (the single asterisk (*) indicates significant differences between groups $p<0.05$).....59

Figure 5.4 Effect of flow rheology on the dimensions: (a) varying chitosan dispensing rate, and (b) varying sodium hydroxide dispensing rate (the single asterisk (*) indicates significant differences between groups $p<0.05$).....60

Figure 5.5 Lumen versus vascular conduit ratio with different relative speed between crosslinker and alginate flow.....61

Figure 5.6 Conduit diameter residual plot: (a) plot of residual versus fitted value, indicating that the data are normally distributed, and (b) plot of residual versus observation run number, indicating that the data are independently distributed.....64

Figure 5.7 Regression model predicted dimension versus experimental dimension: (a) conduit diameter, and (b) wall thickness (sorted from smallest to largest in dimension).....65

Figure 5.8 The wall thickness residual plot: (a) plot of residual versus fitted value indicates the data are normally distributed, and (b) plot of residual versus observation run number indicates the data are independently distributed.....68

Figure 5.9 Experimental and predicted cell viability (E: experimental; P: predicted): (A) for nozzle G16-23; (B) for nozzle G16-26.....70

Figure 5.10 Cell viability under different maximum shear stresses. 71

Figure 5.11 Issues in fabrication: (a) partially crosslinked alginate, (b)-(c) relatively weak structure bent and collapsed due to small wall thickness. 72

Figure 6.1 Media perfusion system. 76

Figure 6.2 Embedding vasculature system into bulk hydrogel: (a-c) the embedding process, and (d-e) embedding vasculature system into bulk hydrogel by (d) automatically printing, and (e) manually patterning. 78

Figure 6.3 Conduits: (a) alginate conduits have acceptable mechanical strength and structural integrity and (b) chitosan conduits are fragile and easy to rupture. 80

Figure 6.4 Media influence on conduit dimensions: (a) 1 hour perfusion experiment with changing perfusion rate, and (b) the influence of perfusion time on conduit dimensions 82

Figure 6.5 Influence of perfusion parameters on conduit dimensions: (a) 1-hour perfusion experiment, and (b) influence of perfusion time 83

Figure 6.6 Perfusion and diffusional characterization of 3%, 4% and 5% alginate conduits (the single asterisk (*) indicates significant differences between groups $p<0.05$). 85

Figure 6.7 Vascular system filled with fluorescent cell media. As soon as the vasculature system was filled, the perfusion was stopped. Fluorescent microscopy images showing the fluorescein intensity: (a) fluorescent image taken at 0 minutes, (b) 10 minutes, and (c) intensity over time. The fluorescent cell media was pumped through vasculature system at a flow rate of 3 ml/min. Fluorescent microscopy image showing the fluorescein intensity: (d) intensity over time, (e) fluorescent image taken at 0 minutes and (f) 10 minutes. 86

Figure 6.8 Clearance was observed between alginate vasculature system and bulk alginate hydrogel: (a) clearance was observed between alginate solution and alginate vasculature system, (b) manually patterned alginate conduit in bulk alginate hydrogel, and (c) printed alginate conduit in bulk alginate hydrogel. Bulk alginate was sliced and sectioned to show the clearance 89

Figure 6.9 A representative figure of the perfusion experiment. 91

Figure 7.1 5% conduits in dehydration test: (a) dehydrated samples, (b) dehydrated samples under microscope still demonstrating conduit shape, (c) an SEM image of dehydrated conduit, and (d) SRW of different alginate concentrations (the single asterisk * indicates significant difference between groups $p<0.05$). 97

Figure 7.2 Swelling test results of conduits with different alginate concentrations. Swelling ratio curve for (a) 3% alginate conduit, (b) 4% alginate conduit, and (c) 5% alginate conduit, (d) time to reach the maximum swelling ratio (T_{ms}), (e) maximum swelling ratio, and (f) liquid

reabsorption capability (W_{maxi}/W_o) (the single asterisk (*) indicates significant difference between groups $p<0.05$).....99

Figure 7.3 Swelling ratio curve over time. 101

Figure 7.4 Degradation process of vasculature: (a-b) SEM images of dehydrated conduit's luminal and outer surfaces, (c) light microscopy image of 3% alginate vasculature directly after fabrication, (d) at day 1, (e) day 7, (f) and day 10. 102

Figure 7.5 Dimensional characterization of the dehydration process: (a) dimension differences of conduits made of different alginate concentrations, (b) conduit diameter after dehydration, (c) diameter shrinkage rate (DSR) of conduits made of different alginate concentrations, and (d) conduits' dimensional changes over time (the single asterisk (*) indicates significant difference between groups $p<0.05$). 104

Figure 7.6 Histology test for six-week-cultured conduits: (a) reasonable collagen deposition can be observed on long-term-cultured vasculatures, (b) delamination of cell sheets observed in some samples during histology sectioning process, and (c-d) thick cell sheets were formed on the conduit walls, where arrowheads show intact cells encapsulated in alginate network. 107

Figure E.1 U-turn curvature.....132

Figure E.2 One layer of conduit network.....133

CHAPTER I

INTRODUCTION

Tissue engineering, which aims to engineer artificial organs or tissues to replace damaged or sick ones in the human body, has been a promising field of research, offering hope of bridging the gap between organ shortage and transplantation needs. Despite progress in tissue engineering, engineering thick tissues and organs such as the liver, heart, and kidney remains a great challenge. Without vascularization, three-dimensional (3D) engineered thick tissues or organs cannot get enough nutrients, gas exchange, and waste removal, all of which are needed for maturation during perfusion [1]. Systems must be developed to transport nutrients, growth factors, and oxygen to cells while extracting metabolic waste products such as lactic acid, carbon dioxide, and hydrogen ions so the cells can grow and fuse together, forming large-scale tissues and organs. Cells in a 3D organ structure cannot maintain their metabolic functions without this ability, which is traditionally provided by blood vessels. However, available biomanufacturing technologies encounter difficulties in manufacturing and integrating a vasculature network into an engineered construct [1]. The available biomanufacturing technology, on the other hand, currently does not allow multi-scale tissue fabrication where bifurcated vessels are required to be manufactured with capillaries to mimic natural vascular anatomy [2]. Although several researchers have investigated developing vascular trees using computer models, generating a massive amount of digital data [3], so far only a few attempts have been made toward fabricating bifurcated or branched conduits with a representative model fabricated using tissue spheroids [4]. Successful maturation toward functional mechanically integrated bifurcated vessels is still a challenge.

1.1 Background

Nowadays, the most popular treatment for loss or damage of tissues or organs is organ transplantation. Data from the U.S. Department of Health & Human Services

(DHH) shows that an average of 79 people receive organ transplants each day [5]. Although organ transplantation shows remarkable results in saving lives, several limitations restrict its application. The first and most important one is shortage of donors. Every year, thousands of people die while waiting for transplants. Data from DHH also shows that an average of 18 people die every day while waiting [5]. The demand for organ transplantation increases dramatically each year, but the number of donors increases relatively slowly. The second challenge is the difficulty of finding a serotype-matched donor. Furthermore, even after a successful transplantation, patients suffer from taking immune-suppression medicine for the rest of their lives to avoid transplant rejection. In addition, due to complication and rejection responses, the percentage of recipients still living five years after transplant is not very high [6]. Data from DHH shows that only 54.4% of lung transplant patients and 69.3% of kidney transplant patients are still alive five years after transplantation [6].

Due to the limitations of organ transplantation, tissue engineering was introduced in the early 1970s. Tissue engineering is a multidisciplinary field aimed at engineering organs or tissue to substitute for damaged or malfunctioning ones in human body. Tissue engineering integrates a variety of disciplines, including medicine engineering, materials science, chemistry and biology. The engineered substitute organs and tissues can be customized; tissue engineering allows a patient's own cells to be used to regenerate substitute tissues or organs without concern about immunization response and rejection. It is a promising but challenging field that could save patients months or years of waiting for matching transplant organs. Ever since its emergence in the 1970s, tissue engineering research has involved a range of human organs, from the earlier focus on human engineered skin [7-10], vascular graft [3, 4, 11-21], bone [22-24] and cartilage [25, 26], and bladder [27-29], to the recent focus on more complex organs such as the liver [30-32], heart [33-35], and kidneys [36, 37]. Several tissue engineering products have even been commercialized, including the artificial skin substitutes AlloDerm®, Dermagraft®,

Integra®, and Matrtiderm® and the artificial blood vessels Dacron® and Goretex®. Although great success has been achieved in simple organs like skin, bone, cartilage, and bladder, which have simple geometry, a low cell oxygen consuming rate and low requirement for blood vessels, difficulties have been experienced in engineering thick functional tissues or organs, such as the heart, liver, or kidney, primarily due to the lack of an efficient media exchange system to deliver nutrients and oxygen and to remove waste. Depending on cell types, very few cells can tolerate being more than 200 μm from a blood vessel due to the limited oxygen diffusion rate. Transplanted cells inside the engineered thick constructs cannot get enough oxygen or nutrients, so nonhomogeneous cell distribution and limited cell activity occurs. In order to successfully fabricate a human-sized functional organ, integration of an artificial vasculature system is essential.

1.2 Fabrication of Tissue-Engineered Constructs

The basic process of tissue engineering involves cell extraction, cell incubation and proliferation, engineered scaffold fabrication, and tissue generation and implantation. Cells can be extracted from either fluidic tissues, such as blood, or solid tissues. Categorized by cell source, there are basically three types of cells: allogeneic cells, xenogeneic cells, and autologous cells [38]. Scaffolds provide a temporary substrate for cell growth and proliferation. Cells, nutrients, and growth factor can be also involved in the scaffold design to facilitate cell activities. When cells reach an appropriate number, they will be seeded on the scaffold and cultured in a bioreactor. To promote cell attachment, various cell adhesion molecules such as laminin (LN) and cadherin have been used to coat the scaffold before seeding [38]. A uniform cell distribution and high cell viability are highly desired.

The strategy of tissue engineering is to manipulate the cell environment by guiding cell behavior. Cells are sensitive to their environment and will behave differently according to material properties, surface treatment, substrate mechanics, and property

degradation kinetics. The selection of a biomaterial, the design of a scaffold, and even the selection of tissue scaffolding fabrication technologies are all important factors for a successful mission in tissue engineering [39, 40].

Several technologies, such as solvent casting/particulate leaching [41, 42], gas foaming [43], freeze-drying [44, 45], electrospinning [46], and bioprinting [47-51], have been developed to fabricate a scaffold for tissue engineering. However, due to the lack of a fundamental understanding of tissue and organ formation, many challenges impede the further development of tissue engineering through tissue scaffolding [1]. One of the main challenges in tissue scaffolding is the inclusion of high cell seeding density. In order to achieve high cell viability, seeding a high number of cells is essential. However, this requirement is difficult to meet within the construction of large and complex functional tissues. Large tissues require a large volume of biomaterials. Even for hydrogels, which have gained more popularity due to their good oxygenation properties, diffusion is still limited to 200 μm [52]. Although high cell seeding density supports cell viability, the oxygenation issue limits cellular growth and tissue regeneration considerably. In order to sustain the desired high metabolic requirements of cells, efficient oxygen and nutrient transport and waste removal mechanisms are critical in the designed scaffold system. In addition to the limited media transportation rate, traditional scaffolding methods also include a high volume of scaffold base biomaterial into the engineered tissue construct, which does not allow high cell-seeding density, limiting cellular growth, cellular interactions, and tissue regeneration. The intrinsic limitation for scaffold-based approaches limited cell proliferation and colonization while cells are immobilized within hydrogels and not able to spread, stretch, and migrate to generate the new tissue. Another challenge in tissue scaffolding is locating spatially controlled multiple cell types. Traditional scaffold fabrication technologies do not allow spatial organization and thus cannot achieve multi-cellular integration.

In addition, degradation and its corresponding adverse effects, such as toxic or acidic byproducts, also diminish cell viability [38]. Physicochemical properties of biomaterials mostly change during degradation due to physical, chemical, mechanical, and biological interactions between biomaterial and the surrounding environment. This change may induce different biological responses to the cellular matrix. The extracellular matrix (ECM) formation and biomaterial matrix degradation rates need to be precisely controlled to ensure the structural integrity during tissue formation well as cell functionality upon stimulation by alternating matrix mechanical properties. Eliminating scaffolding biomaterial completely is not wise because it will trigger limitations related to mechanical integrity since cells need a temporary structure to attach, proliferate, and regenerate the new tissue. Therefore, it is not trivial to eliminate the inclusion of biomaterials; however, minimizing their inclusion will greatly lessen the aforementioned issues.

1.3 Bioprinting

Although lots of technologies have been introduced to fabricate tissue scaffold, most of them have great limitations in biocompatibility, precision control, and easy manipulation [53]. Bioprinting is a revolutionary new term recently introduced in developing artificial 3D tissue or organs. It is widely used in fabrication of the engineered tissue construct. In contrast to traditional tissue engineering approaches, where cells are seeded after scaffold fabrication, bioprinting technology enables seeding cells during the fabrication process by depositing cells within the scaffold matrix. It is a 3D layer-by-layer bioadditive process, where living cells in high density are printed through a computer-controlled robotic bioprinter [53]. According to the literature [47], bioprinting possesses several advantages: it is an automated approach that offers a pathway for scalable reproducible mass production of tissue engineered products; it allows a precise simultaneous 3D positioning of multiple cell types; it enables tissue reconstruction with a

high level of cell density; and finally, it can solve the problem of vascularization in thick tissue constructs.

1.3.1 Bioprinting Technologies

Although bioprinting is a newly established field, it has experienced rapid growth during the last decade. Several bioprinting methods have been developed, including inkjet-based bioprinting [48-50], extrusion-based bioprinting [51], acoustic bioprinting [54, 55], and laser based bioprinting [56-60]. Inkjet approaches print cell suspensions by creating and releasing droplets of fluid. Inkjet-based bioprinting is a high-throughput, easy-implementation technology that is suitable for printing low-viscous biomaterials. There are two types of inkjet-based bioprinting: continuous inkjet-based bioprinting and drop-on-demand inkjet-based bioprinting. Due to surface tension on the nozzle tip, the size of droplets is usually much larger than the nozzle size. Thus, the diameter of a single inkjet droplet is around 50-300 μm limited by the nozzle size [61]. Also, droplet deformation during the fabrication process is another concern in inkjet-based bioprinting. Laser-based bioprinting involves laser-guided direct cell printing [58-60], and laser-induced bioprinting [56, 57]. Laser-guided direct cell printing takes advantage of differences in the refractive index of the cell and the cell media, while laser-induced bioprinting patterns cells by the force of the pressure of laser-induced vapor bubbles. Laser-based bioprinting has high spatial resolution and precise control, whereas the printing speed of laser-guided bioprinting method is relatively low. The acoustic bioprinting method, on the other hand, has a high throughput that can reach up to 100,000 droplets per second [54]. No nozzle is used in this method, so the classic problems associated with nozzle inclusion, such as shear stress and nozzle clogging, can be eliminated. The acoustic bioprinting method utilizes acoustic waves to form an acoustic focal point at the interface between the air and fluid, generating acoustic droplets. The extrusion-based bioprinting method encapsulates cells into hydrogels. Cell-encapsulated

biomaterials are printed layer by layer in the form of solid filaments. The diameter of printed filaments is around the size of the nozzle tip. The bioprinting method used in this dissertation can be classified under extrusion-based bioprinting technology. The proposed system in this dissertation is capable of directly printing vasculature networks in forms of tubular conduits. Compared with the traditional bioprinting-based conduit, conduits fabricated in this work have a mechanically acceptable and biologically promising continuous vasculature network that can be fabricated in a wide range of cross-sectional dimensions [62, 63].

1.3.2 Biomaterials for Bioprinting

Biomaterials are defined as "any substance (other than a drug) or combination of substances, synthetic or natural in origin, which can be used for any period of time, as a whole or part of a system, which treats, augments, or replaces any tissue, organ or function of the body" in the literature [64]. Biocompatible biomaterials must be selected to fabricate a scaffold. The term refers to the ability of a material to perform with an appropriate host response in a specific situation [65]. No adverse response should be triggered by implantation of biocompatible material. A tissue scaffold is supposed to act as a template for tissue ingrowth and healing, so selection of the right biomaterial is critical.

Biomaterials can be classified into metals, ceramics, synthetic polymers, natural polymers, and various combinations of these [38]. When selecting a biomaterial, the material properties, implant site requirements and fabrication technologies should be all taken into consideration. In bioprinting, hydrogels are the most commonly used biomaterials. Defined by N. A. Peppas in 1987, hydrogels are jelly-like materials that are composed of mostly liquid; however, they can be developed into cross-linked structures via covalent bonds, physical chain entanglements or association bonds [66]. They have become more popular in tissue engineering and drug delivery fields in recent years

because of their appealing media transportation rates, biocompatibility, and biodegradability [57]. When cells are seeded into hydrogel, their highly swollen 3D crosslinked network facilitates media exchange inside the engineered construct. The hydrogel family is composed of natural and synthetic hydrogels. Up to now, hydrogels that have been used in bioprinting include natural hydrogels such as collagen, alginate, agarose, and chitosan, and synthetic hydrogels such as hyaluronan methylcellulose (HAMC), polyethylene glycol diacrylate (PEGDA), and various combinations of these [67] (see Table 1.1). In this work, alginate and chitosan are selected to fabricate a blood-vessel-like vasculature network due to their low cost, easy handling, compatibility with the proposed bioprinting system, and appealing media transport properties.

Table 1.1

Bioprintable Hydrogels

Property	*Collagen*	*Fibrin*	*Alginate*	*Chitosan*	*HAMC*	*PEGDA*
Gelation Method	Hydrophobic	Thrombin-catalyzed	$CaCl_2$	pH (basis)	room temperature	UV light
Gelation Time	Low	High	High	Medium	High	Medium
Swelling Ratio	Low	High	High	Low	Low	High
Cell Survival	Medium	Low	Low	Low	Medium	Medium
Biocompatibility	Low	High	High	High	High	High
Printability	Medium	Low	High	Low	Low	Medium
Cost	Low	High	Low	Low	Low	Medium
In vivo Testing	Human	Human	Human	Human	Rat	Human

Source: S.V. Murphy, A. Skardal, and A. Atala, Evaluation of hydrogels for bio-printing applications. Journal of Biomedical Materials Research, 2013. 101(1): p. 272-284.

1.4 Alginate and Chitosan as Biomaterial

Alginate is a natural biomaterial derived from seaweed. It can also be synthesized by bacteria. Alginate is an unbranched binary copolymer of (1-›4)-linked β-D-mannuronic acid (M) and α-L-guluironic acid (G) residue (as shown in Figure 1(a) [64]). The uronic acid residues are distributed along the polymer chain in a pattern of blocks [64]. Depending on the origin of alginate, the relative amount of two utonic acid monomers is different. Alginate has good hydrophilic property. It is capable of absorbing 200-300 times its own weight in water. Due to its abundant source, good biocompatibility, and mild crosslinking process, alginate is well known to the biomedical and pharmaceutical industries, especially for the treatment of topical wounds [68].

Many methods have been used to crosslink alginate, including ionic crosslinking, thermal crosslinking, and cell crosslinking [69]. The ionic crosslinking approach is the most commonly used method to prepare alginate hydrogels. The gelation process happens instantaneously with the presence of calcium and divalent cations except for magnesium. The divalent cations ionically interact with the carboxylate anions in G residues and form ionic bridges between different polymer chains. The gelation process of alginate occurs at room temperature, without changing pH value or producing any toxic byproduct, which makes alginate an ideal selection for cell encapsulation and other tissue engineering applications [64]. Although alginate is good for its biocompatibility, biodegradability, low toxicity, and immunological inertness, it still has several drawbacks. For example, there is no specific interaction between mammalian cells and alginate hydrogel, and it inhibits protein absorption due to a negative charge balance caused by electrostatic repulsion [69].

The history of chitosan fabrication dates back to the 19th century. It is abundant in the shells of crabs and shrimp. It is a linear polysaccharide composed of randomly districted D-glucosamine (D-unit) and N-acetyl glucosamine (A-unit) linked in a β(1-›4)

manner [64]. Chitosan has a wide usage in tissue engineering for applications such as nerve regeneration, membrane barriers, and inhibitors of blood coagulations [65]. No additive is needed to crosslink chitosan. The crosslinking process is based on the neutralization of chitosan amino groups [60, 71]. At a low pH level, amino groups obtain protonate and become positively charged, which makes chitosan water soluble. If the pH level is higher than six, amino groups deprotonate and lose charge. Then chitosan becomes an insoluble hydrogel [71, 72].

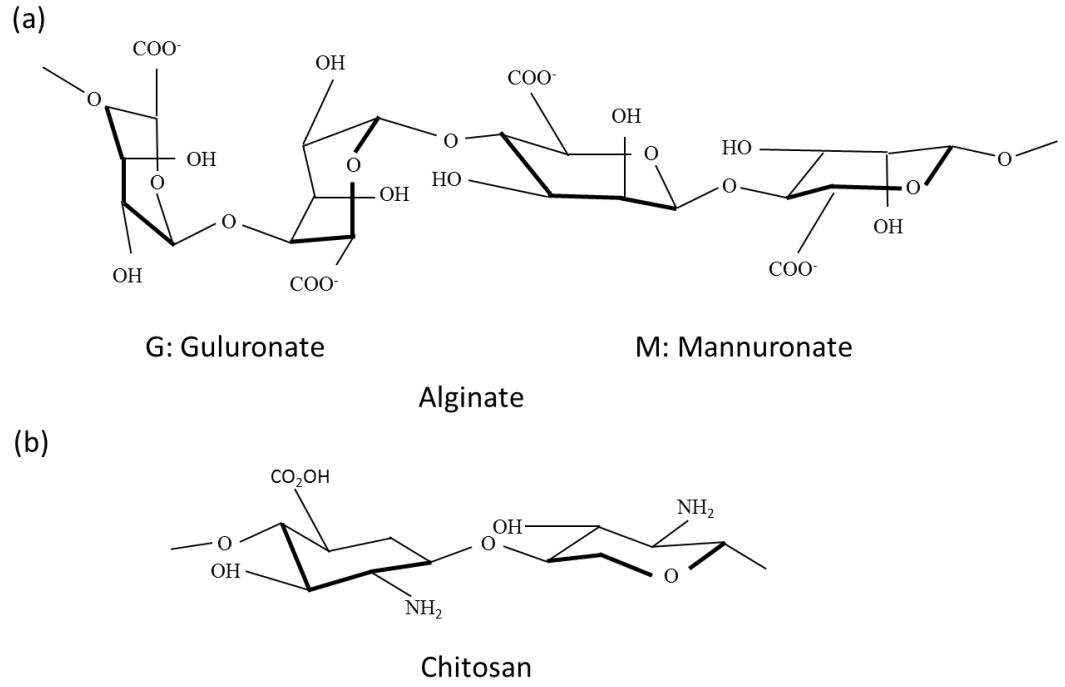

Figure 1.1

Chemical structure of alginate and chitosan.

Source: J. O. Hollinger, An Introduction to Biomaterial second ed. 2011: CRC Press, Taylor & Francis Group.

1.5 Fabrication Technologies for Vasculature Network

Although great progress has been made in biofabrication of tissue constructs over the past decades, the engineered constructs still have difficulty in biomimicking natural thick tissues or organs due to an inefficient media exchange rate [73]. Nonhomogeneous cell distribution and limited metabolic activities are often observed, since planted cells cannot get enough oxygen, growth factors, and nutrients for metabolic activities that are needed for maturation during perfusion [74]. Microfluidic system integration has shown great potential to alleviate current limitations. Lee et al. [75] showed a great difference in cell viability with or without an embedded vasculature network in hydrogel scaffolds. Ling et al. [76] demonstrated that vasculature networks were capable of delivering sufficient nutrients to encapsulated cells, and higher cell viability resulted in regions closer to the vasculature network. In addition, vasculature network systems were not only able to provide media to maintain cell metabolic activities, but also to deliver signals to guide cell activities.

To date, several methods have been used in microfluidic fabrication, including soft lithography [76-77], photo-patterning [79-81], laser-based technologies [82, 83], molding [17], and bioprinting [4, 49, 62, 84]. However, due to their intrinsic characteristics, each of the above-mentioned technologies has its own advantages and disadvantages. Soft lithography is the most popular method in vasculature network fabrication due to its accuracy, reproducibility, and low cost. Using soft lithography technology, Ling et al. [76] fabricated a microfluidic network in cell-laden agarose hydrogel, which resulted in a significant increase in cell viability during media perfusion compared to static controls. Cuchiara et al. [77] developed a soft lithography process to fabricate a poly(ethylene glycol) diacrylate hydrogel microfluidic network. With media perfusion, encapsulated mammalian cells maintained a high viability rate in bulk hydrogel. However, soft lithograph is not a viable option for fabrication of complex 3D constructs due to cumbersome procedures. Despite their superior accuracy and

repeatability, photo-patterning and laser-based methods may not be suitable for fabricating thick tissue constructs because of their limited light-penetrating depths in precursor solution. Offra et al. [79] proposed a focal laser photoablation method capable of generating micro-structures in transparent hydrogels. Cell behavior was successfully guided by the micro-conduit pattern. Molding is an inexpensive and scalable method, but complex 3D geometry is difficult to achieve and post-procedures are required after fabrication. Nazhat et al. [85] used a molding method to incorporate unidirectionally aligned soluble phosphate-based glass fibers into dense collagen scaffolds. The diameters of the achieved vasculature networks were around 30-40 μm, and a significant increase in cell viability was observed in hydrogel sheets. Despite the plethora of work in vasculature network fabrication, only a few researchers have developed strategies for bioprinting of vasculature networks, where bioprinting can be defined as a computer-controlled layer-by-layer bioadditive process enabling printing living cells precisely per predefined patterns [86]. Cell-encapsulated biomaterials can be directly patterned onto substrate without any pretreating steps (such as mold or mask preparation). It offers several advantages, including precise control [48, 87], automated fabrication capability [80, 81], and feasibility of achieving complex shapes [13, 63]. In this regard, Mironov et al. [47] proposed a technique in which tissue spheroids were used as building blocks to construct a vascular conduit. While tissue spheroids have high cell density (around 10,000 cells per spheroid), this strategy accelerates the tissue formation process and enables enhanced cell viability upon printing. His proposed work has been limited in both conduit length and diameter. Moreover, fusion of cells requires a relatively long period of time, which obstructs integration of the abovementioned technology with the fabrication of the rest of the tissues to assemble into organs. Zhao et al. [16] recently presented a methodology in bioprinting of perfusable straight vasculature network structures in thick hydrogels. They created a temporary structure to form the lumen, which was then removed by a post-process.

Despite several technologies applied in vasculature network fabrication, most are simply the creation of conduits inside bulk materials [17, 78-80, 85, 91]. A natural blood vessel network, on the other hand, is a complex hierarchical organization, where tubular vessels branch into smaller-scale vessels up to capillary scale. Biofabrication of a perfusable branched network remains a challenge. In past decades, several methodologies have been developed for vascular tissue fabrication, including decellularized tissues [11, 14, 34, 92, 93], cell sheet conduits [94, 95], biodegradable synthetic polymer-based constructs [19, 96, 97], and natural biomaterial-based blood vessel grafts [4, 15, 49, 63]. Decellularized tissues have several advantages, including that their composition consists purely of natural ECM, as well as their biocompatibility and good mechanical properties. However, significant shrinkage was observed during the decellularization process [92]. In addition, formation of aneurysm, thrombosis, infection, and residual antigenicity still remains a problem [93]. The cell sheet approach has achieved the best burst pressure results so far [95]. Yet, the ECM fibers did not exhibit circumferential alignment, which is a unique mechanical property of arteries [97]. One problem with the synthetic polymer-based approach is the lack of specific reactive groups within their surface chemistry. Difficulties were observed in cell attachment and signaling [98]. In addition, byproducts of synthetic polymers during the fabrication process are usually toxic or acidic, which further devastates the cell culture environment [38]. Natural biomaterials have great biocompatibility and biodegradability that provide an ideal substrate for cell attachment and proliferation. However, as an inherent weakness, the mechanical properties of natural biomaterials are limited. Ozawa et al. [15] approached vascular conduit fabrication using an alternative method called electrodeposition, where short vascular conduits with diameters ranging from 200 to 500 μm were fabricated through deposition of alginate around a Pt wire electrode. The wire electrode was then pulled away to create the lumen.

Bioprinting is a promising approach for tissue fabrication, providing high precision, high automation, and high flexibility [13, 99, 100]. Norotte et al. [4] used

tissue spheroids and printed them sequentially in cylindrical form to build multicellular short stretches of vessels ranging from 0.9 to 2.5 mm in diameter. In that study, agarose cylinder was used as the temporary support material to create the lumen until tissue maturation was achieved. Xu et al. [54] proposed a platform-assisted inkjet-based bioprinting system to fabricate zigzag cellular tubes vertically through fusion of droplets with encapsulated fibroblast cells. Although bioprinting brings more flexibility to fabricating artificial vascular constructs, incorporation of a vascular system in thick tissue fabrication is still a challenge.

1.6 Thesis Objective and Outline

In this research, a new fabrication approach is presented to fabricate vascular constructs and has a great potential in printing living organs [63]. The presented method has greater flexibilities compared to existing strategies in the literature. It offers several advantages, including that it has no post-fabrication procedure and that it enables direct bioprinting of complex media exchange networks. Complex 3D shapes can be achieved using a layer-by-layer bioadditive process through a computer-controlled system without a need for post-processing. The proposed method generates vasculature networks with an average diffusion distance considerably smaller than the hydrogel diffusion limit (approximately 200 μm), which, theoretically, allows the printed vasculature network to provide sufficient oxygen transport [85]. The printed vasculature network allows transport of media, including nutrients, water, and oxygen, via perfusion; the waste is removed from the system in the same manner. Eight-hour perfusion experiments were conducted, and no leakage or occlusion was observed.

The content of this work is structured as below:

Chapter 2: Fabrication of vascular conduits

Chapter 3: Modeling and analysis of dispensing rheology

Chapter 4: Layer-by-layer fabrication strategy

Chapter 5: Characterization of influences of fabrication parameters on conduits

Chapter 6: Evaluation of media perfusion capabilities

Chapter 7: Dehydration, swelling, degradation, mechanical properties, and histology test

Chapter 8: Summary, conclusions, and future work recommendations

CHAPTER II

FABRICATION OF VASCULAR CONDUITS

Tissue engineering is a complex and challenging process to execute due to the lack of a fundamental understanding of tissue and organ formation. One of the major challenges is the inclusion of blood-vessel-like conduits to support cell viability in terms of nutrients and oxygen transport. This work introduces a new approach in tissue engineering through fabrication of vessel-like printable vasculature networks, which can be processed in tandem with cellular assembly construction. This chapter investigates the manufacturability of printable vascular conduits. A pressure-assisted solid freeform fabrication platform is developed with a coaxial needle dispenser unit to print hollow hydrogel conduits, which will later be used to support nutrients and oxygen transport through the printed cellular assembly. Samples of vasculature networks were fabricated with the proposed system. A successful biofabrication method and bioprinting system should be biocompatible and relatively safe for biological cells and tissue growth. To further evaluate the system, cell viability and function analysis were evaluated. In this study, cartilage progenitor cells (CPCs) encapsulated in conduits maintained a viability of over 95% during prolonged culture.

2.1 Materials and Methods

2.1.1 Materials

Prior to making a hydrogel solution, sodium alginate powder (Sigma Aldrich, United Kingdom) and calcium chloride powder (Sigma Aldrich, United Kingdom) were treated with ultraviolet (UV) light for sterilization three times for a 30-minute cycle. Ultraviolet-sterilized sodium alginate was dissolved in deionized water to make 4% solutions. Solutions were mixed with a magnetic stirrer (HANNA Instruments, U.S.A.) until homogeneity was reached. Similarly, the crosslinking solution was prepared by

dissolving UV-sterilized calcium chloride in ultra-purified water (Invitrogen™ Life Technologies, U.S.A.) at 4% (w/v). A solution of 1.0 M sodium hydroxide (Fluka Analytical, Germany) was used to crosslink the chitosan solution.

2.1.2 Cell Preparation

Bovine cartilage progenitor cells (CPCs) were cultured at 37° C in 5% CO_2 in DMEM/F12 (1:1) supplemented with 10% fetal bovine serum (FBS), 50 µg/µl L-ascorbate, 100 µg/µl penicillin, 100 µg/ml streptomycin, and 2.5 µg/µl Fungi zone. Culture media was changed every other day. The CPCs were passaged onto tissue culture dishes, and passage 3 cells were used for bioprinting. Cells were harvested by 0.25% Trypsin-EDTA (Life Technologies, U.S.A.) prior to printing. The alginate solution was prepared by adding UV-sterilized sodium alginate powder to DMEM-base culture media. Cells were mixed with the sodium alginate solution (2% in DMEM-based media) immediately after harvesting and were kept at room temperature before printing.

2.1.3 Fabrication System

The vasculature network fabrication system consisted of five parts (as shown in Figure 2.1(a)): (A) a single-arm robotic printer (EFD® Nordson, U.S.A.); (B) a homemade co-axial nozzle unit; (C) a syringe pump (New Era Pump System Inc.,U.S.A.), which was used to dispense crosslinker; (D) a liquid dispenser (EFD® Nordson, U.S.A.), which was used to dispense biomaterial; and (E) a computer that was used for robotic control. Figure 2.1(b) is an enlarged view of the coaxial nozzle. The coaxial feature of the homemade co-axial nozzle unit is demonstrated in Figure 2.1(c). More detailed information about the coaxial nozzle is presented in Section 2.1.2.

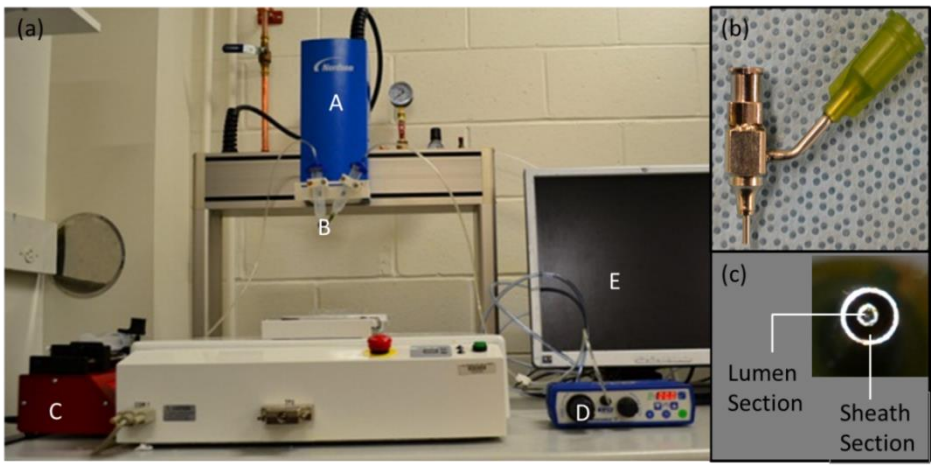

Figure 2.1

The fabrication system: (a) experimental setup, (b) coaxial nozzle, and (c) a cross-section view of the coaxial nozzle tips.

2.1.3.1 Fabrication Process

The biomaterial and its crosslinker solutions were loaded separately into the coaxial nozzle unit. The coaxial nozzle assembly consisted of three parts: a feed tube, an outer tube, and an inner tube. During the printing process, the coaxial unit was mounted on the single-arm robot, which was controlled by a computer. Hydrogel solutions were pumped into the feed tube, which was used to feed hydrogel solution (alginate or chitosan) into the sheath section (the space formed between the outer and inner tubes) (see Figure 2.1(c)). The hydrogel solution flowed through this space and dispensed from the outer tube tip. Crosslinker was dispensed through the lumen section (see Figure 2.1(c)). When the two solutions contacted, crosslinking (or gelation) started, and a tubular gel was formed with a vasculature network. A representative model of the coaxial nozzle with hydrogel and crosslinker solution flow paths is demonstrated in Figure 2.2(b). The gelation process was an instantaneous chemical reaction as the crosslinker ions bound the

hydrogel chains together. The penetration of crosslinker ions in the hydrogel solution depends on the concentration of crosslinker ions, diffusion time, and crosslinking kinetics. As soon as materials were dispensed from the coaxial nozzle tip, the conduit formed. The hydrogel solution dispensed from the outer tube was crosslinked and became the gel shell, where crosslinker flow through the inner part formed the hollow core.

2.1.3.2 Coaxial Nozzle

In this research, coaxial nozzles were fabricated using three fluid-dispensing tips. This nozzle assembly consists of a feed tube, an outer tube, and an inner tube, as shown in Figure 2.2(a). The feed tube is used to feed the hydrogel into the cavity formed between the outer and inner tubes while the crosslinker is fed through the inner tube to create the lumen of conduit, as shown in Figure 2.2(a). A cross-sectional view of this nozzle is also demonstrated in Figure 2.2(b). A hole with the same outer diameter as the feed tube was created in the barrel of the outer tube to attach the feed tube. The luer lock hub on the barrel of the outer tube was removed using a lathe, and the tip was ground to ensure that the inner and the outer dispensing tips were even. The feed tube was inserted until it was flush with the inner diameter of the barrel, sealed with J-B KWIK 4-minute epoxy, and reinforced with J-B STIK steel-reinforced epoxy putty. The two tubes were aligned concentrically using a stainless steel fixture manufactured using micro-milling. Then, the tubes were sealed with J-B KWIK 4-minute epoxy reinforced with J-B STIK steel-reinforced epoxy putty.

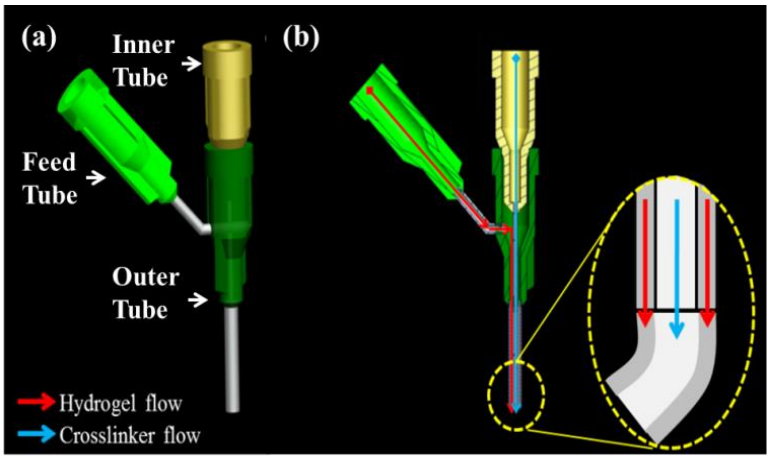

Figure 2.2

Coaxial nozzle unit: (a) 3D model of the coaxial nozzle, (b) cross-sectional view of coaxial nozzle assembly model with fluid flow paths for hydrogel and crosslinker solutions.

2.1.4 Cell Viability Analysis

For cell viability assay, CPCs were encapsulated in conduits through the coaxial printing process, as described in Section 2.2.2, and underwent confocal imaging studies at day 1, day 4, and day 7. Samples were stained with calcein acetoxymethylester (calcein AM) and ethidiumhomodimer-2 (Invitrogen), at a concentration of 1.0 mM each. Calcein AM is metabolized in living cells to form a bright green fluorescent product that accumulates in the cytosol. Ethidium homodimer is a red fluorophore that stains the DNA of nonviable cells but cannot penetrate into living cells with intact plasma membranes. The staining medium was aspirated, and new medium was added to wash off any residual stains on conduit surfaces before fluorescent illumination. After a 30-minute incubation period, conduits were imaged using an Olympus FluoViewTM FV1000 laser scanning confocal microscope (LSCM) (Olympus NDT Inc., MA). Z-axis projections were

assembled from images of the conduits from the surface to the bottom with a depth of 1600 μm at 50 μm intervals. ImageJ (National Institutes of Health, Bethesda, MD) was used for automated counting of red- and green-stained CPCs in z-axis projections, and percentages of viable cells were calculated. The percentage of viable cells for each sample was calculated by averaging the values of three different projections, each composed of six planes.

2.2 Results

2.2.1 Sample Fabrication

In this research, structural integrity was highly desired because printed conduits would later be used to transport media. Fabrication was performed with a 4% alginate solution with a dispensing rate of 0.2 ml/min, which has demonstrated acceptable cell viability and good structural integrity. A 4% crosslinker solution was dispensed at 1.5 ml/min for gelation purposes. The nozzle velocity was set at 14 mm/s. Coaxial nozzle assembly with a 23 gauge (330 μm inner diameter (I.D.), 650 μm outer diameter (O.D.)) inner needle and an 18 gauge (840 μm I.D., 1270 μm O.D.) outer needle was used for printing. Optimal dispensing parameters thus play a critical role in generating hollow lumen without occlusion. For instance, the relative speed of the coaxial nozzle (robot arm) and the dispensing speed determine the quality of the printed samples. When the nozzle velocity (the velocity of the robot arm holding the coaxial nozzle) was considerably greater than the dispensing speed, the sample was dragged away by the coaxial nozzle from their desired deposition location, and rupture was observed, which dramatically prevented media transport. If the nozzle velocity, on the other hand, was considerably slower than the dispensing speed, then samples were not printed straightly.

Figure 2.3(a) shows a sample printed conduit fabricated using alginate mixed with green food dye for visualization purposes, where a yellow food dye solution was transported through the conduit without any occlusion. Figure 2.3(b) illustrates the

smallest printed sample under a digital microscope showing uniform wall thickness. The average inner and outer diameters of the fabricated conduits were approximately 135 µm and 309 µm, respectively. Compared to the hydrogel diffusion limit of 200 µm presented in the literature [52], the printed samples with 87 µm wall thickness are promising for efficient oxygenation and for nutrient and waste transportation. Figure 2.2(c) shows a long sample patterned on a zigzag custom-made perfusion chamber with a length of approximately 1 m without any occlusion, demonstrating the potential of the printed vasculature network for continuous perfusion. We tested the perfusion capabilities of cellular structures in a perfusion chamber, where oxygenized cell culture media was perfused for 8 hours using a perfusion system (this is further discussed in Chapter 5). No occlusion or leakage was observed during the perfusion process.

Figure 2.2(d) is a scanning electron microscope (SEM) microscope view of conduit. The lumen feature can be easily observed. Deformation was observed during the dehydration process. Due to the nature of the sample, a 1 nm resolution of the SEM microscope cannot be achieved. A 50k magnification was the highest resolution that could be observed with the SEM microscope. A further magnification would burn the sample specimen, and the clarity of the picture would deteriorate significantly (see Figure 2.2(e)). Figure 2.2(e) is an example that was taken at the naturally fractured site of a sample. A 100k magnification was used. The clarity of the picture is low, but one can still see the sponge like structure of alginate.

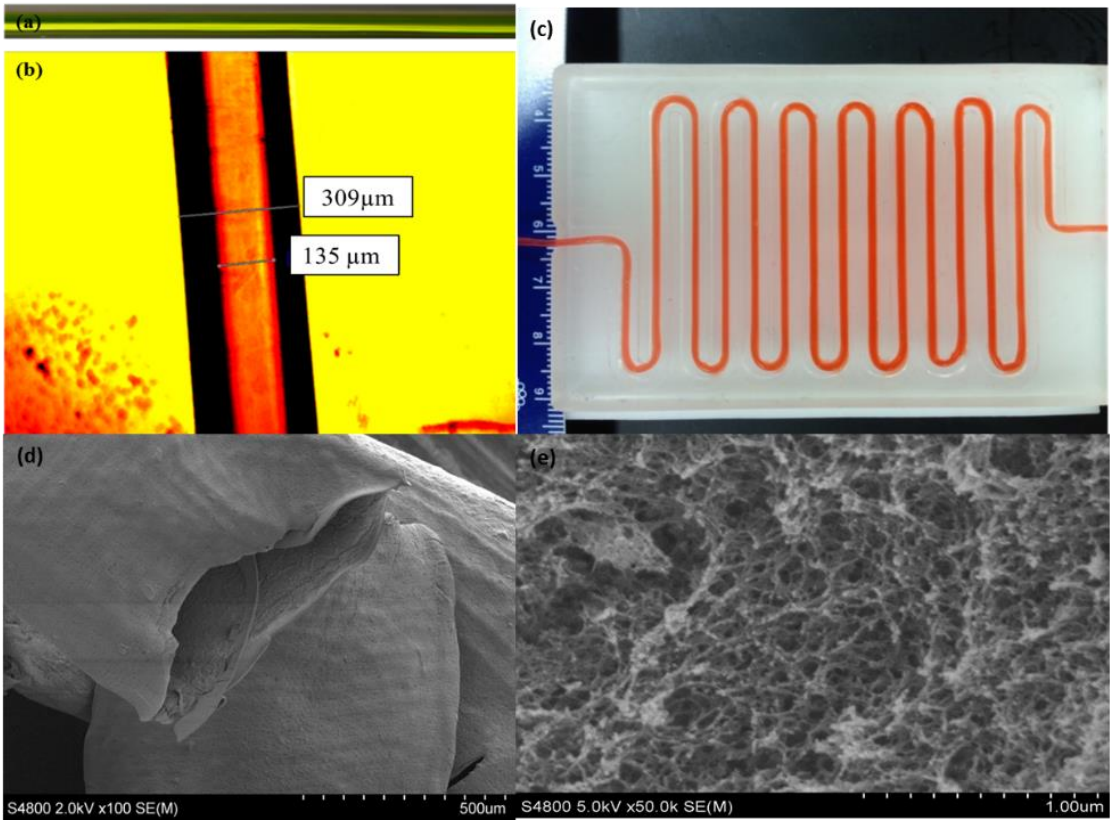

Figure 2.3

Sample printed structures: (a) a printed conduit allowing media transport shown with a yellow food dye, (b) an image of a single conduit analyzed under a digital microscope, (c) a long vasculature network perfused with cell media, (d) alginate conduit under an SEM microscope, and (e) alginate hydrogel sponge-like structure.

2.2.2 Cell Viability Analysis

Cells were evenly distributed in alginate solution before printing and were successfully encapsulated into a printed sample during the fabrication process (see Figure 2.4(a)). Individual cells in alginate matrix within the wall of the sample were highlighted in an SEM image as presented in Figure 2.4(b). Confocal imaging revealed that few cells

were dead (ethidium homodimer) and that most of the cells were stained with calcein AM (green) two days after cell encapsulation. On day 4 and day 7, although a few cells were stained with ethidium homodimer (red), most of the cells were still viable. ImageJ analysis revealed that initial cell viability was around 1 day (95.1±1.7%) post-encapsulation within samples and maintained high cell viability on day 4 (95.8±1.2%) and day 7 (97.6±1.2%) (see Figure 2.4(c)).

A z-axis stack of confocal images with 50 μm intervals is shown in Figure 2.5, demonstrating live/dead cells and their distribution. Samples were sliced in parallel to the direction of vascular walls layer by layer to show the lumen. Figures 2.5 (e)-(f) show the lumen.

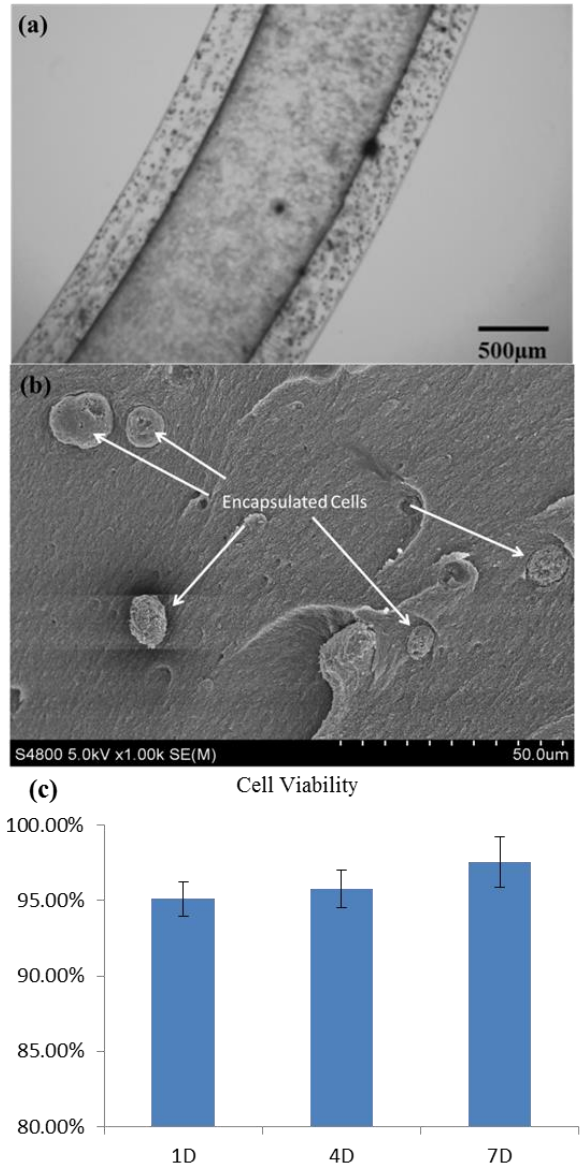

Figure 2.4

Representative images of printed samples: (a) light microscopic image shows that cells were uniformly encapsulated, and lumen was clearly identified in the center, (b) an SEM image showing encapsulated cells, and (c) time course of CPC viability after the bioprinting process. Cell viability was analyzed using ImageJ. Each symbol represents the average of the results for three z-projections composed of six planes from confocal laser imaging. The error bars indicate standard deviations (n=3).

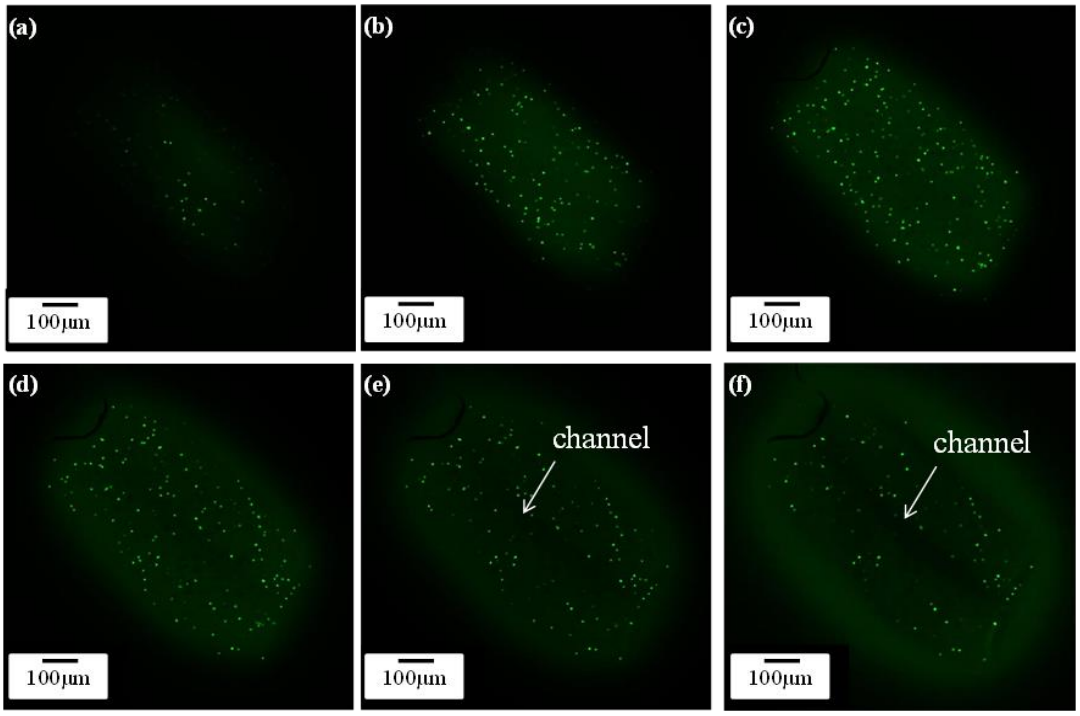

Figure 2.5

Confocal images showing the lumen: (a-f) z-projection from top to center of a sample, with 50 μm intervals showing the solid wall of samples and the lumen.

2.3 Discussion and Conclusion

In this thesis, a new process is presented for the biofabrication of a printable continuous vasculature network, which shows great potential in perfusing cell-type media that can be used to fabricate thick tissues or living organs in the near future. The proposed approach can be easily integrated with the cell-printing process in tandem, which is promising in terms of seeding co-cultured cells and developing heterogeneous organ and tissue structures. The printed vasculature networks have the potential to allow media transport, including nutrients, water, and oxygen, through perfusion.

Although CPCs were used to test the biological relevance of the fabrication system, the proposed bioprinter platform can be used to print other living cells, such as endothelial and smooth muscle cells, for biomimetic development of conduits.

CHAPTER III

MODELING AND ANALYSIS OF DISPENSING RHEOLOGY

In a traditional extrusion-based deposition system with a regular nozzle apparatus, the dispensed material is still in a solution (liquid) state during printing, and the material deposition speed can be controlled by controlling the nozzle travel velocity. However, in the presented coaxial nozzle system, conduits form as soon as the material is dispensed through the nozzle tip. The conduit deposition speed and conduit dimensions cannot be controlled simply by varying the nozzle travel velocity. The conduit deposition speed depends on several factors, such as biomaterial and crosslinker concentration, coaxial nozzle configuration and size, and dispensing rates. It is essential to set the nozzle travel velocity equal to the conduit deposition speed for patterned printing. If the nozzle travel velocity is set slower than the conduit deposition speed, the formation of a curl shape is observed during printing. A conduit cannot be printed on the desired position as the pattern is designed. On the other hand, if the nozzle travel velocity is set larger than the conduit deposition speed, the conduit is dragged away from the original printed location. In this chapter, predictive models were developed for conduit deposition speed, which is critical for precise printing based on designed patterns. In addition, the shear stress distribution inside coaxial nozzles was modeled to theoretically explain the cell viability behavior inside the printed conduits.

3.1 Dispensing through the Coaxial Nozzle

During the fabrication process, a change in deposition speed was observed. At the beginning, the conduit was dispensed slowly, and a larger diameter was obtained. The deposition speed increased due to gravity and eventually maintained a stable speed. It was observed that conduit diameters (lumen diameter and outer diameter) are always different from the diameters of nozzle tips ($D_{NO} \neq D_O$ and $D_{NI} \neq D_I$) (see Figure 3.1). D_{NO} and D_O are the outer diameter of the outer needle and inner diameter of the inner needle,

respectively. D_O and D_I are the outer diameter of conduit and the lumen diameter of the conduit. V_{Di} is the conduit dispensing velocity, and V_{De} is the network deposition speed.

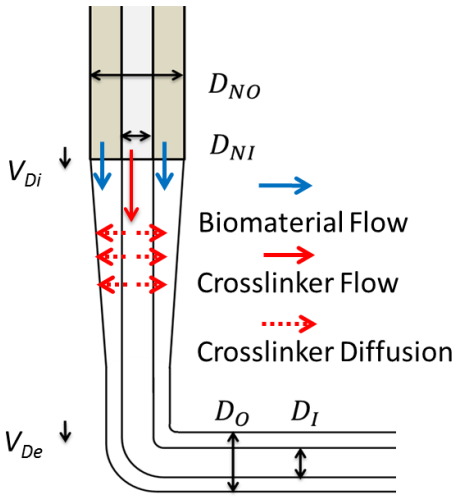

Figure 3.1

Dispensing process in a coaxial nozzle.

According to the literature [94], the volumetric flow rate of a non-Newtonian fluid through a concentric shape can be approximated as:

$$Q = \frac{n\pi D_{NO}^{\ 3}}{8(3n+1)}\left(\frac{-\Delta P}{L}\frac{D_{NO}}{4K}\right)^{1/n}\left\{(1-\lambda^2)^{(n+1)/n} - \sigma^{(n-1)/n}(\lambda^2-\sigma^2)^{(n+1)/n}\right\} \quad (1)$$

where n, K, ΔP, and L are power-law flow behavior index, power-law consistency coefficient, pressure drop, and length of capillary, respectively. The relation between its shear stress and the shear rate in Newtonian flow is linear. Its power-law flow behavior

index is n =1. However, in non-Newtonian flow, n is not equal to 1. Because the n of 3% alginate is 0.76 [46], the system is non-Newtonian. For non-Newtonian flow, $\sigma = D_{NI}/D_{NO}$. λ is a constant and depends on σ and n, which can be obtained from Appendix B.

3.2 Modeling of Dispensing Rheology

Assuming that dispensed conduits have uniform diameter and uniform deposition speed (V_{Di}), the flow rate can be calculated as:

$$Q = \pi\left(\frac{D_{NO}^2 - D_{NI}^2}{4}\right)V_{Di} \tag{2}$$

Assuming that the volume of alginate does not change considerably before and after crosslinking:

$$\pi\left(\frac{D_{NO}^2 - D_{NI}^2}{4}\right)V_{Di} = \pi\left(\frac{D_O^2 - D_I^2}{4}\right)V_{De} \tag{3}$$

The conduit deposition speed can be obtained by combining Equations (2) and (3) as below:

$$V_{De} = \frac{4nR^3}{(3n+1)(D_O^2 - D_I^2)}\left(\frac{-\Delta P}{L}\frac{R}{2K}\right)^{1/n}\left\{(1-\lambda^2)^{(n+1)/n} - \sigma^{(n-1)/n}(\lambda^2 - \sigma^2)^{(n+1)/n}\right\} \tag{4}$$

where R=D_{NO}/2. Three nozzles, one consisting of a 23 gauge inner needle (330 μm I.D., 650 μm O.D.) and a 16 gauge outer needle (1190 μm I.D., 1460 μm O.D.) (G16-23), another consisting of a 25 gauge inner needle (250 μm I.D., 520 μm O.D.) and an 18

gauge outer needle (840 µm I.D., 1270 µm O.D.) (G18-25), and a third consisting of a 23 gauge (330 µm I.D., 650 µm O.D.) inner needle and an 18 gauge (840 µm I.D., 1270 µm O.D.) (G18-23) outer needle, were used to understand the dispensing rheology of the coaxial nozzle in Section 2.5.2. A G18-25 coaxial nozzle was used in a predictive study for conduit deposition speed in Section 3.1.1.

3.2.1 Determination of Pressure Gradient

The values of independent variables in Equation (4) can be obtained from the literature, except $-\Delta P/L$. $-\Delta P/L$ is a variable dependent on pressure and the nozzle dimensions. It can be calculated by substituting the values of Q (flow rates were measured using rheological experiments), K (K=8587 for 3% alginate [51]), n (n=0.76 for 3% alginate [51]), σ ($\sigma = D_{NI}/D_{NO}$), λ (can be obtained in [99]), and D_{NO} into Equation (1). The volumetric flow rates were calculated from experimental measurements and plotted in Figure 3.2(a). The flow rate increased as the pressure increased. In this study, 3% alginate was used since $-\Delta P/L$ is independent of alginate concentration. The calculated $-\Delta P/L$ is presented in Figure 3.2(b). The calculated $-\Delta P/L$ is used in Equation (4) to calculate the predictive conduit deposition speed as presented in the next section. The measurement of flow rate and pressure gradient table can be obtained in Appendix C.

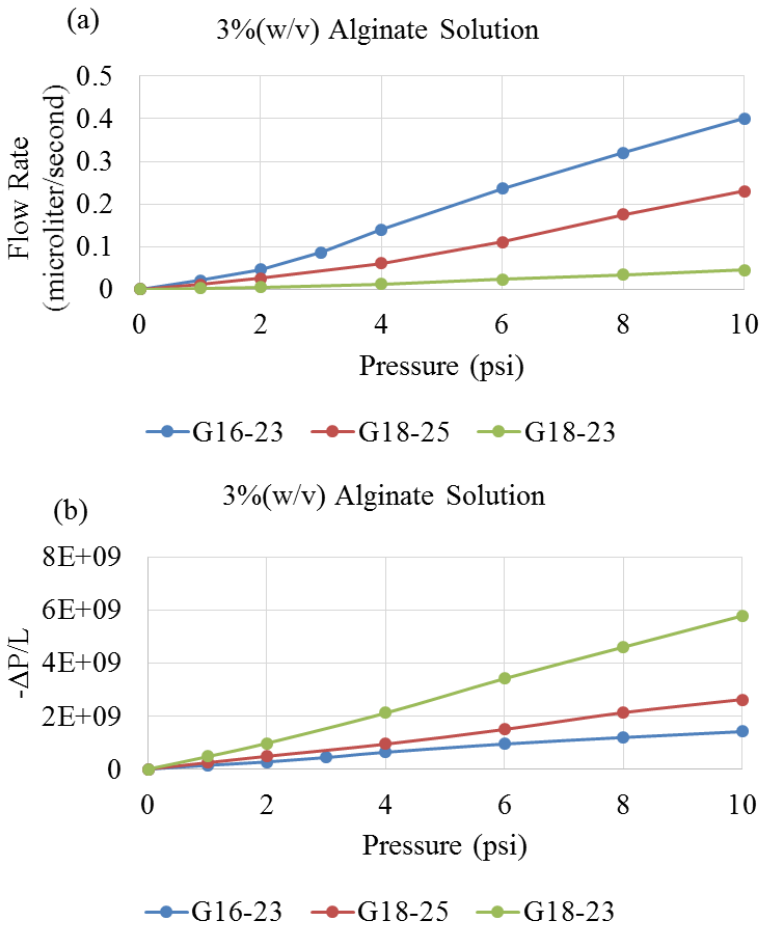

Figure 3.2

Effect of pressure rate on (a) flow rate and (b)-*ΔP/L*.

3.2.2 Predicted Speed versus Experimental Speed

In zigzag pattern printing, the nozzle travel speed needs to be set at the same value as the conduit deposition speed. Issues occur if the nozzle travel speed is too fast or too slow. The pressure gradient calculated in the previous section was used to calculate the predictive deposition speed. The calculated pressure gradient was measured using 3% alginate solution. Due to the concentration-independent property of the pressure gradient,

it can be used to calculate the deposition speed for alginate of any concentration. In this section, 3% and 4% alginate were used to test the accuracy of the deposition speed model.

In this experiment, 3% and 4% alginate aqueous solutions were prepared and used to verify the proposed predictive model for conduit deposition speed. By observation, 3%, 4%, and 5% alginate solutions were suitable for printing due to their acceptable mechanical properties along with good biocompatibility. Our previous work showed that cell viability decreased as alginate concentration increased [101]. Alginate solutions with concentrations higher than 5% have deteriorating cell viability. However, the mechanical property of alginate hydrogel increases as alginate concentration increases. Conduits with good structure integrity cannot be obtained using alginate solutions with concentrations lower than 3% [74]. The 4% alginate solution was randomly selected to test the prediction model.

The $CaCl_2$ concentration and dispensing rate were set to be 4% and 3 ml/min, respectively. Results of the predicted speed versus experimental speed for both 3% and 4% alginate are shown in Figures 3.3(a)-(b). The experimental speed data was obtained by measuring the length of the dispensed conduit and the dispensing time. The predicted speed was calculated using Equation (5) (K=8587 for 3% alginate, K= 14,960 [95] for 4% alginate, n=0.76 for 3% alginate and n=0.86 for 4% alginate). Differences between predictive and experimental speed were relatively small, where the average percentage of error was 3.7%. As shown in Figure 3.3, the conduit deposition speed increased as the alginate pressure increased. The 4% alginate conduit had a slower deposition speed than that of the 3% alginate conduit.

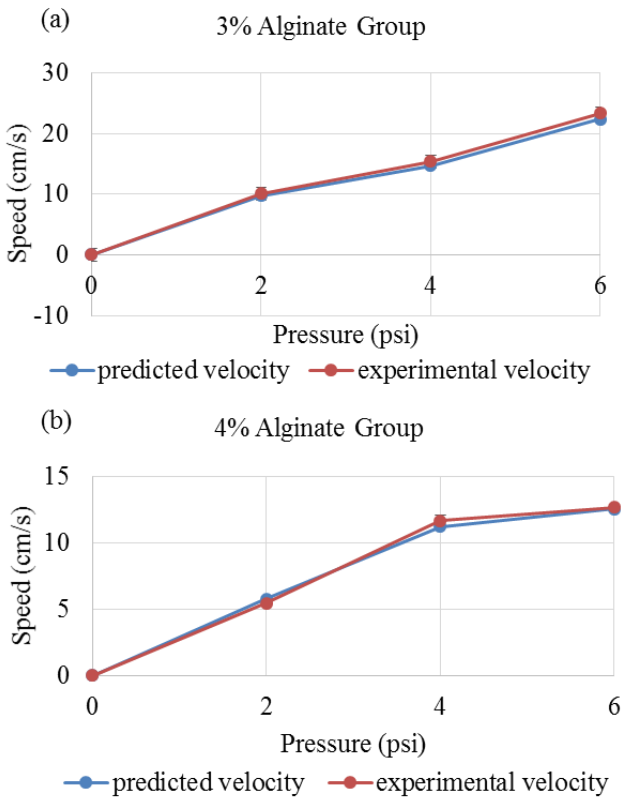

Figure 3.3

Predicted speed versus experimental speed with (a) 3% alginate, and (b) 4% alginate (data are mean ± SD, 3 samples).

3.2.3 Printed Conduits

As Figure 3.4 shows, conduits are printed in a 0°-90° lay-down pattern to develop a 3D network. Figure 3.4(b) is an eight-layer conduit. The nozzle speed was set at 14 mm/s. In order to eliminate occlusion of conduit, arc fitting was used at U-turns between two conduits during zigzag printing.

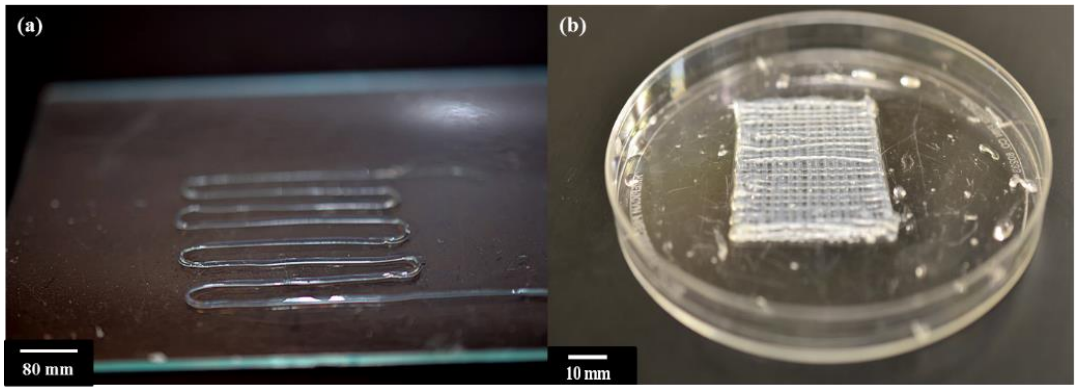

Figure 3.4

Printed conduit: (a) a single layer of conduit pattern, and (b) eight layers of conduit.

3.3 Shear Stress Model for the Coaxial Nozzle

According to the literature [94], the shear rate of a non-Newtonian flow through coaxial nozzle can be approximated as:

$$\tau = \left(\frac{-\Delta p}{L}\right)\frac{R}{2}\left(\xi - \frac{\lambda^2}{\xi}\right) \tag{5}$$

where Δp is the pressure changes, L is the length of the coaxial nozzle, R is the inner radius of the outer nozzle, and $\xi = r/R$ (r is fluid radius with boundary conditions as: $r_{minimum}$ =outer radius of the inner nozzle and $r_{maximum}=R$), respectively. λ is a constant that locates the position where the flow velocity is at its maximum. Its value is dependent on the power-law flow behavior index (n) and σ ($\sigma = r_{minimum}/R$). The theoretical shear stress distribution and liquid profile inside the coaxial nozzle were shown in Figure 3.5.

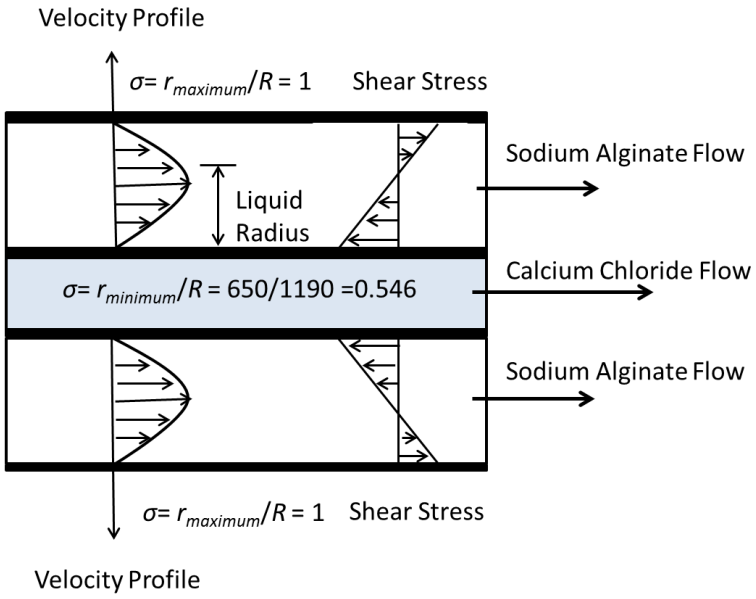

Figure 3.5

A representative figure of non-Newtonian flow through a coaxial nozzle

The values of the independent variables in Equation (4) can be calculated or obtained, except -*ΔP/L*. -*ΔP/L* is a variable that can be calculated as:

$$\frac{-\Delta P}{L} = \left[\frac{Q}{\frac{n\pi R^3}{(3n+1)} \left(\frac{R}{4K}\right)^{1/n} \left\{ (1-\lambda^2)^{(n+1)/n} - \sigma^{(n-1)/n} (\lambda^2 - \sigma^2)^{(n+1)/n} \right\}} \right]^n \tag{6}$$

where *K* is the power-law consistency coefficient and *Q* is the volumetric flow rate.

3.3.1 Shear Stress Distribution inside the Coaxial Nozzle

In order to calculate the coaxial nozzle shear stress, the value of $-\Delta P/L$ is needed. The $-\Delta P/L$ is calculated by Equation (1) with K (K=14960 for 4% alginate [95]), n (n=0.86 for 4% alginate [95]). The volumetric flow rates were calculated from experimental measurements and plotted in Figure 3.6(a). The calculated $-\Delta P/L$ is presented in Figure 3.6(b). The calculated $-\Delta P/L$ is used in Equation (5) to calculate shear stress. The calculated shear stress distribution in coaxial nozzles with 5psi, 10psi, and 20 psi alginate dispensing pressure is plotted in Figure 3.7. As depicted from the figure, shear stress reaches its maximum value on the outer surface of the inner nozzle. Then, the shear stress diminishes as r increases and vanishes at the inflection point somewhere around the middle point of the space between nozzles. The inflection point is not necessarily located in the middle of the space between nozzles; its location depends on the value of λ. Beyond the inflection point, the shear stress changes its direction and increases as r increases. The main cause of cell death during bioprinting process is shear stress.

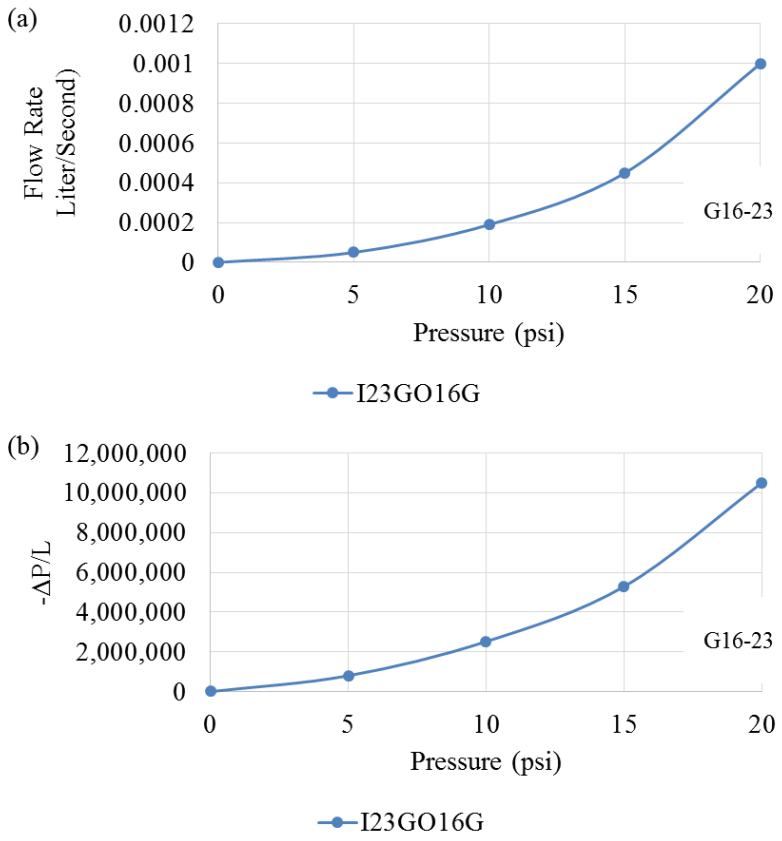

Figure 3.6

Dispensing rheology: (A) effect of alginate pressure rate on volume flow rate of 4% alginate solution, (B) effect of pressure rate on -*ΔP/L*

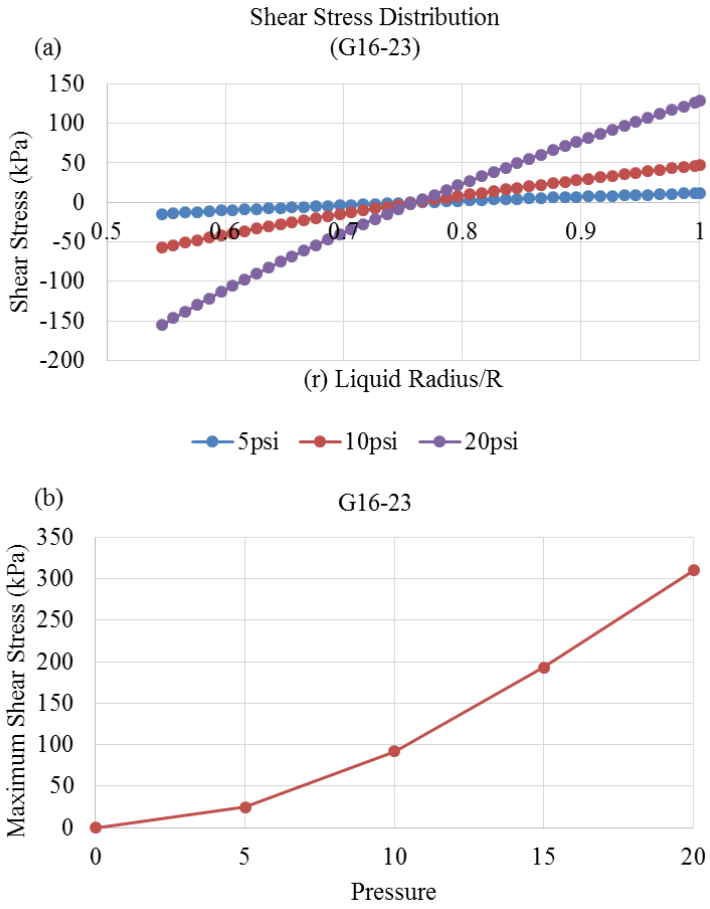

Figure 3.7

Shear stress inside the coaxial nozzle: (a) shear stress distribution inside the coaxial nozzles, and (b) maximum shear stress with various alginate dispensing pressures

3.3.2 Cell Viability Distribution over the Cross Section Profile in Conduit

Figure 3.8 (a) shows a cross section of a printed conduit. The conduit inner wall was made by alginate flow near the outer surface of the inner tube (see Figure 2.2), and the conduit outer wall was made by alginate flow near the inner surface of the outer tube.

Thus, the theoretical cell viability distribution along the radius of the conduit is shown in Figure 3.8(b). The minimum cell viability can be obtained at the conduit inner wall, and the maximum cell viability can be obtained at the middle of the alginate wall (corresponding to the shear stress vanishing point inside the coaxial nozzle, as shown in Figure 3.5). This result is consistent with the observations in Figure 3.9, in which the dead cells were mostly observed along the inner and outer conduit walls. In addition, more dead cells were observed on the inner wall than the outer wall. Figure 3.7(b) shows the maximum shear stress value under varying dispensing pressures. Maximum shear stress increases as the dispensing stress increases. The calculated share stress inside the coaxial nozzle under different pressures can be obtained in Appendix D.

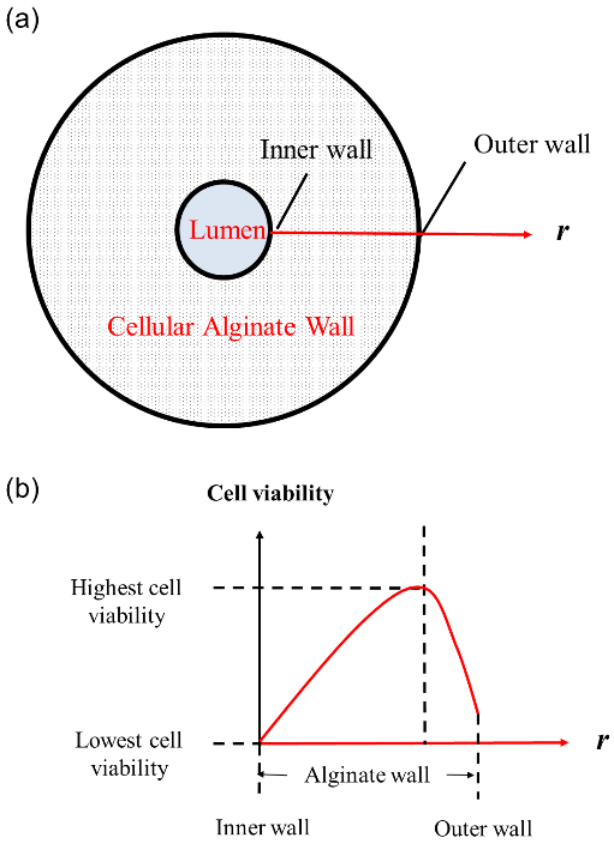

Figure 3.8

Representative figure of cell viability distribution along *r*: (b) a cross-section of conduit, and (c) cell viability distribution along *r*.

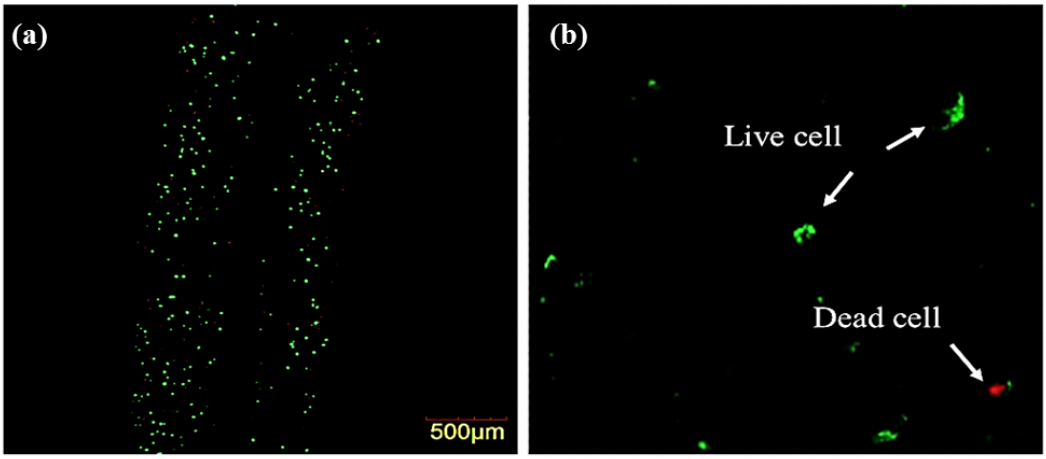

Figure 3.9

Laser confocal imaging for live/dead staining of the printed structure at 5 psi with G16-23 nozzle: CPCs labeled with calcein AM and ethidium homodimer after cell encapsulation and imaged with a confocal laser scanning microscope: (a) quantifiable dead and live cells; most of the cells that are viable post-printing are seen in live cell conduit, and merging both conduits shows the relative ratio and location of dead cells and live cells, (b) live and dead cells are fluorescent green and fluorescent red, respectively.

3.4 Discussion and Conclusion

In this chapter, the dispensing rheology of the coaxial nozzle was explored, and the conduit deposition speed was mathematically modeled. Prediction of printing parameters is important because the nozzle travel speed should be set at exactly the conduit deposition speed. The proposed deposition speed model has relatively good accuracy compared to the measured values. Also, the shear stress distribution inside the coaxial nozzle was modeled. The coaxial nozzle has its highest shear stress at the inner needle's outer surface, which can be proved by less cell viability at the inner wall of the alginate conduit.

Pressure gradient is a variable that depends on needle size, pressure, and the length of the needle. In coaxial needle fabrication, it is difficult to fix the length of the needle due to the variability in needle lengths and fabrication processes. Normally, under the same pressure, a bigger coaxial nozzle (which has a larger space between the inner and outer needles) is supposed to have a larger maximum shear stress under the same pressure. However, due to the variability in needle fabrication, the calculated result is not the case. The calculated maximum shear stress of nozzles G16-23 and G16-26 are listed in Table 3.1. G16-26, which consists of a 23 gauge inner needle (230 μm I.D., 470 μm O.D.) and a 16 gauge outer needle (1190 μm I.D., 1460 μm O.D.) has a larger space between the inner and outer needles than the G16-23 needle, which consists of a 23 gauge inner needle (330 μm I.D., 650 μm O.D.) and a 16 gauge outer needle (1190 μm I.D., 1460 μm O.D.).

Table 3.1

Calculated maximum shear stress for G16-23 and G16-26.

Pressure	*Needle Type*	
(psi)	G16-23	G16-26
5	14.35 kPa	23.8 kPa
10	57.37 kPa	89.6 kPa
15	108.79 kPa	170.7 kPa
20	155.1 kPa	270.4 kPa

One interesting finding is that a conduit with spiral shape resulted from improper fabrication parameters (see Figure 3.10). The formation of this spiral-shaped conduit was primarily due to the velocity difference between the conduit deposition speed and the static liquid in the collector. A spiral curl was formed as conduits approached the

collector. A similar phenomenon was observed in a previous study [104]. The higher the conduit deposition speed, the more significant the spiral curl phenomenon observed. One way to avoid the spiral shape formation is to use a lower alginate dispensing pressure. It was also observed that calcium chloride dispensing speed did not have much effect on the spiral formation.

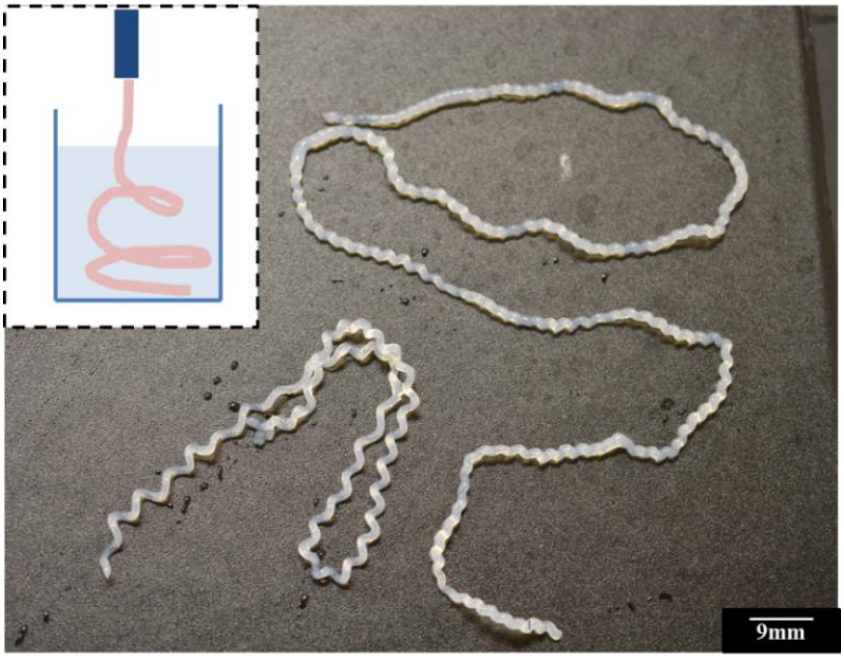

Figure 3.10

Conduits with spiral shape

CHAPTER IV

LAYER-BY-LAYER FABRICATION STRATEGY

During the printing process, crosslinking starts from the lumen site and proceeds through the outer surface, which provides the possibility of generating stronger joints between layers in layer-by-layer fabrication. When one layer is printed, since the crosslinking process is realized from the inner luminal wall, the outermost section of the conduit is still not fully crosslinked. It is possible for the proposed technology to fabricate a 3D conduit with stronger adhesion between layers as long as printing time is well planned with respect to the gelation time so that the previously printed layer is not fully crosslinked before printing the next layer. If the outermost sides of conduits in two consecutive layers (or contact surfaces of conduits in two layers) are not fully crosslinked at the moment when printing of the latter is completed, it is possible to facilitate adhesion between layers.

4.1 Prediction of the Minimum Gelation Time

The gelation process has a critical role in creating mechanically integrated conduits, particularly in constructing a 3D construct using layer-by-layer manufacturing, where each layer should adhere to adjacent ones with permanent bonding. The alginate gelation process is, indeed, an instantaneous chemical process in which divalent cations ionically interact with carboxylate anions of α-L-guluronic acid (G units) monomers, forming ionic bridges between different polymer chains. The gelation time mainly depends on the diffusion of the Ca^{2+} ions in the radial direction. According to the literature [104], formation of the process can be approximated by the following diffusion equation:

$$\frac{\partial C}{\partial t} = D\frac{\partial^2 C}{\partial r^2} - \frac{\partial S}{\partial t} \tag{7}$$

where D is the Ca^{2+} diffusion coefficient. In Equation (1), C is the Ca^{2+} concentration in the $CaCl_2$ solution and S is the concentration of Ca^{2+} that is already crosslinked at time t in radial distance r, assuming D is a constant ($D = 10^{-9}$ m^2/s [97]) However, in reality, the diffusion coefficient changes during the gelation process and decreases as the conduit begins to gel [98].

According to Equation 7, the Ca^{2+} gelation process can be approximated as:

$$\frac{\partial C + \partial S}{\partial t} = D\frac{\partial^2 C}{\partial r^2} \tag{8}$$

where $\partial C + \partial S$ is the concentration of Ca^{2+} in both the calcium chloride solution and the crosslinked Ca^{2+}. It is equal to the concentration of the originally prepared calcium chloride solution. Assuming all Ca^{2+} in chloride solution is used to crosslink alginate, Equation A.1 can then be approximated as:

$$\frac{Ca^{2+}}{t_{gel}} \approx D\frac{4Ca^{2+}}{D_O^2 - D_I^2} \tag{9}$$

Thus, the minimum gelation time, t_{gel}, can be approximated as:

$$t_{gel} \approx (D_O^2 - D_I^2) / 4D \tag{10}$$

Predicting the gelation time in this research thus enables one to predict the manufacturability of conduit in 3D.

4.2 Pre-printing Plan

For a square conduit with a width of W and the intended distance between consecutive conduits l, the number of straight conduits (n_c) can be calculated as:

$$n_c = \left\lfloor \frac{W - D_O}{l} \right\rfloor + 1 \tag{11}$$

While n_c is an integer, the distance between consecutive conduits should be updated using the inverse of Equation (5) as:

$$l^* = \frac{W - D_O}{n_c - 1} \tag{12}$$

Then, the length of the conduit on a layer can be calculated as (including arc-shape U-turns) (detailed calculation process can be obtained in Appendix E):

$$n_c\left(W - \left(D_o + l^*\right)\right) + \left(n_c - 1\right)\frac{\pi l^*}{2} \tag{13}$$

Thus, the printing time (t_p) for a layer can be calculated as:

$$t_p = \frac{n_c\left(W - \left(D_o + l^*\right)\right) + \left(n_c - 1\right)\frac{\pi l^*}{2}}{V_{De}} \tag{14}$$

where V_{de} is the conduit deposition speed defined in the previous chapter. In this study, the predicted minimum gelation time of fabricated conduits ranges from 0.6 min to 12 min. In order to get a strong adhesion between layers, the gelation time should be greater than the total printing time of two consecutive layers represented as in Equation (15):

$$t_{gel} \geq 2t_p \tag{15}$$

Thus, when one designs the conduit, the following inequality should be held to generate strong adhesion between layers:

$$\frac{(D_o^2 - D_I^2)}{8D} \geq \frac{n_c\left(W - \left(D_0 + l^*\right)\right) + \left(n_c - 1\right)\frac{\pi l^*}{2}}{V_{De}} \tag{16}$$

where l^* is the updated distance between conduits due to the requirement that the number of conduits should be an integer.

4.3 Discussion and Conclusion

In this chapter, the minimum gelation time of conduit was calculated. The minimum gelation time of a conduit depends on the conduit dimensions. In this study, the

predicted minimum gelation time ranges from 0.6 min to 12 min, depending on conduit geometry. The calculated gelation time can be obtained in Appendix F. Also, the strategy for layer-by-layer printing is proposed. With a carefully made preprinting plan, it is possible for the proposed technology to fabricate 3D vasculature networks with stronger adhesion between layers as long as printing time is well planned with respect to the gelation time so that the previously printed layer is not fully crosslinked before printing the next layer.

The minimum gelation time in the work is a theoretical gelation time for conduits and was assumed to be under static conditions. However, in reality, calcium chloride was dispensed using a syringe pump. Depending on the dispensing rate, an axial pressure could be present inside conduits, which might accelerate the calcium chloride diffusion process and thus further decrease the conduit gelation time.

CHAPTER V

CHARACTERIZATION OF INFLUENCES OF FABRICATION PARAMETERS ON CONDUITS

The main purpose of this chapter is to precisely control the dimensions of a fabricated conduit, the effects of printing parameters, and the media flow characteristics on structural dimensions so that we can readily manufacture conduit at various sizes, facilitating further fabrication of branched tubes used for mimicking the hierarchically organized natural vasculature.

5.1 Materials and Methods

5.1.1 Materials

Prior to making a hydrogel solution, sodium alginate powder (Sigma Aldrich, United Kingdom), chitosan powder (Sigma Aldrich, Iceland), and calcium chloride powder (Sigma Aldrich, United Kingdom) were treated with UV light for sterilization three times for 30 minutes per cycle. Ultraviolet-sterilized sodium alginate was dissolved in deionized water to make 3%, 4%, 5%, 6%, and 7% solutions, and UV-sterilized chitosan was dissolved in 1.0 M acetic acid (Fluka Analytical, Germany) to make 2%, 2.5%, 3%, and 4% solutions. Solutions were mixed with a magnetic stirrer (HANNA Instruments, Rhode Island, U.S.A.) until homogeneity was reached. Similarly, the crosslinking solution was prepared by dissolving UV-sterilized calcium chloride in ultra-purified water (Invitrogen^{TM} Life Technologies, Carlsbad, CA) at 4% (w/v). Then, 1.0 M sodium hydroxide (Fluka Analytical, Germany) was used to crosslink the chitosan solution.

5.1.2 Fabrication

Two coaxial nozzle assemblies are used in this chapter: an assembly with 26 gauge (230 μm I.D., 457 μm O.D.) inner needle and an 18 gauge (840 μm I.D., 1270 μm

O.D.) outer needle used for the experiment in Section 4.3, and another assembly with a 23 gauge (330 µm I.D., 650 µm O.D.) inner needle and an 18 gauge (840 µm I.D., 1270 µm O.D.) outer needle used for the experiment in Section 4.4. The coaxial nozzle used in Section 4.3 had an inner nozzle with a larger outer diameter that reduced the conduit thickness. This allowed us to further evaluate and understand the effect of dispensing parameters on the functional conduit wall.

5.1.3 Measurement and Statistical Analysis

In Sections 4.3 and 4.4, more than 70 pieces of data were obtained by measuring different conduits and different sections of printed conduits under a digital microscope (Motic®, BA310, Motic Incorporation Inc., Canada). The data shown in this chapter were an average of all 70 pieces of data. The statistical analysis was carried out using Minitab 16. For all data, normality and independent tests were performed to ensure the data used for statistical significance analysis followed the required test assumption. The statistical difference analysis among groups was conducted by analysis of variance (ANOVA). Groups with a significance level of $p<0.05$ were considered as significant.

5.1.4 Fractional Factorial Design

A resolution V factorial design was conducted using Minitab 16 software to study the effect of dispensing parameters and media flow characteristics on conduit dimensions (µm). In resolution V fractional factorial design, no mean effect or two-factor interaction is aliased with any other main effects or two-factor interactions, but two-factor interactions are aliased with three-factor interactions. Five factors, X_1-alginate concentration (%), X_2-calcium chloride concentration (%), X_3-alginate dispensing pressure (psi), X_4-calcium chloride dispensing rate (ml/min), and X_5-nozzle dimension factor (µm), were set at two levels, low and high, as presented in Table 5.1. In characterization experiments, the inner diameter of the outer needle (D_{io}) was used as the nozzle dimension factor. In wall thickness characterization experiments, the space

between the two nozzles (S_n) was the nozzle dimension factor. The space between two nozzles was obtained by subtracting the outer diameter of the inner needle from the inner diameter of the outer needle.

Table 5. 1

Low and high values of the five factors involved in the bioprinting process.

Variables	X_1	X_2	X_3	X_4	X_5	
Levels	Alginate Concentration (%)	Calcium Chloride Concentration (%)	Alginate Dispensing Pressure (psi)	Calcium Chloride Dispensing Rate (ml/min)	Nozzle Dimension factor (µm)	
					D_{io}	S_n
Low (-1)	3	4	3	1.5	840	190
High (1)	4	5	6	3	1190	540

Fractional factorial design was conducted with the factors in Table 3 to study their effects as well as the effects of their interactions on conduit diameter and wall thickness. Sixteen experiments were conducted for the fractional factorial design. Only main effects of five factors and their two-way interactions were considered.

Normality and independent tests were conducted on the data using normal probability plot and residual plot, respectively. Next, the average of the data was used as a data point in factorial design. A regression model was used to interpret the underlying relationship between five independent factors and resulting conduit diameter and lumen diameter. Two different coaxial nozzle units were used in the conducted experiments. One consisted of a 23 gauge inner needle (330 µm I.D., 650 µm O.D.) and a 16 gauge outer needle (1190 µm I.D., 1460 µm O.D.), and the other consisted of a 23 gauge inner

needle (330 µm I.D., 650 µm O.D.) and an 18 gauge outer needle (840 µm I.D., 1270 µm O.D.). The space between two nozzles was obtained by subtracting the outer diameter of the inner needle from the inner diameter of the outer needle. The regression model was used to interpret the underlying relationship between five independent factors and the conduit dimensions (conduit diameter (D_O) and wall thickness (WT)). Normality and independent tests were conducted on the data using the normal probability plot and the residual plot, respectively. Next, the average of the data was used as a data point in factorial design.

5.2 Results

5.2.1 Effect of Biomaterial Concentration

In this study, hydrogels including chitosan and alginate were explored to determine their fabrication feasibility. In the first experiment, 2%, 2.5%, 3%, and 4% chitosan solutions were prepared to print conduits, and 1.0 M sodium hydroxide was used to crosslink the chitosan solution. However, only 2.5% and 3% chitosan were feasible to fabricate structurally well-integrated conduits with the selected fabrication parameters. The mechanical integrity of 2% chitosan was weak; the conduit snapped before a uniform conduit formed. The viscosity of 4% chitosan was too high to be dispensed from the coaxial nozzle. It is possible that a higher dispensing pressure could allow ejecting the high viscous solution, but this could induce considerable shear stress and reduce cell viability. Thus, Figure 5.1(a) shows conduit dimensions data obtained from conduits with 2.5% and 3% solution concentrations. As chitosan concentration increased, conduit and lumen diameters and wall thickness decreased given the same dispensing pressure; however, more levels are required to perform a trend analysis.

Figure 5.1(b) shows the effect of alginate concentration on conduit dimensions. In this study, 3%, 4%, 5%, 6%, and 7% alginate and 4% $CaCl_2$ were used to fabricate conduits. In general, alginate with a solution concentration greater than 7% demonstrated

limited cell viability and is not recommended for cell encapsulation experiments. The 4% alginate group had the smallest conduit dimensions, including the lumen and the conduit diameter as well as the wall thickness. The results in Figure 5.1(b) revealed that there was no distinct trend between alginate concentration and conduit dimensions. Indeed, the dimensions of printed conduits were primarily affected by the diffusion rate of Ca^{2+} ions, which was a function of alginate concentration and the thickness of the alginate ejected from the coaxial nozzle. In other words, alginate concentration affected the diffusion rate of Ca^{2+} ions as well as the thickness of the conduit ejected from the nozzle per the fixed dispensing pressure.

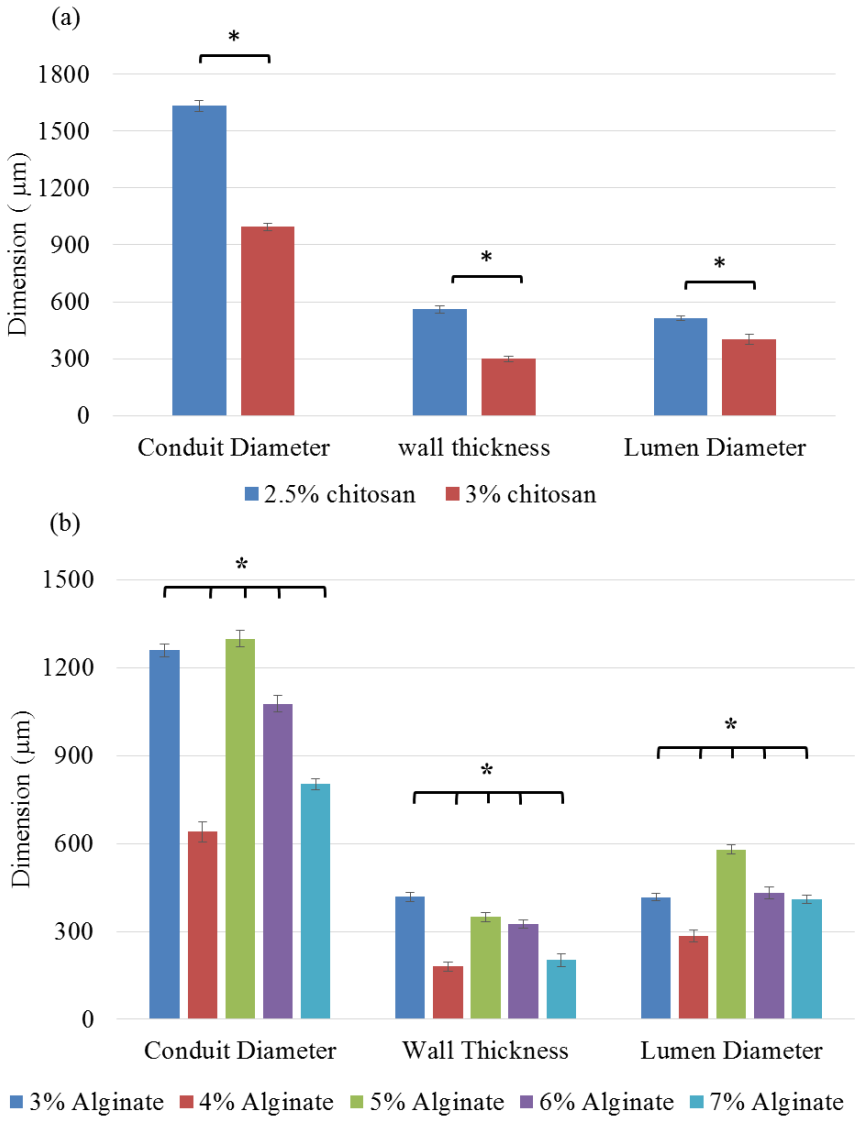

Figure 5.1

Dimensional comparison of printed conduits per variation in hydrogel concentrations, including: (a) chitosan and (b) alginate (the single asterisk (*) indicates significant differences between groups $p<0.05$).

5.2.2 Effect of Crosslinker Concentration

Similarly, the concentration of $CaCl_2$ also had an effect on the conduit diameter. The results shown in Figure 5.2 were obtained from an experiment conducted with 4% alginate cross-linked with different $CaCl_2$ concentrations. Alginate dispensing pressure and $CaCl_2$ dispensing rate were fixed at 6.6 ml/min and 4.15 ml/min, respectively. These parameters were selected because they resulted in functional conduits. The data showed a normal distribution with a p-value smaller than 0.05. Different crosslinker concentrations generated different conduit dimensions (luminal and outer diameter) due to a diffusion-dependent gelation process occurring throughout the cross-section of conduits. The results reveal that there is no distinct trend between crosslinker concentration and conduit dimensions (see Figure 5.2). This can be explained by the diffusion phenomena, where the diffusion process is not only mediated by the change in concentration values, but also affected by ion size, hydrodynamic resistance, and crosslinking chemistry. For 4% alginate concentration, the smallest conduit diameter was obtained at 2% $CaCl_2$, where the smallest conduit diameter was 617 μm with a wall thickness of 175 μm. The lumen versus conduit ratio (lumen diameter/conduit diameter) was approximately 44%, which indicated that 19% less biomaterial volume was used compared to the same diameter cylindrical strand printed using traditional nozzle systems.

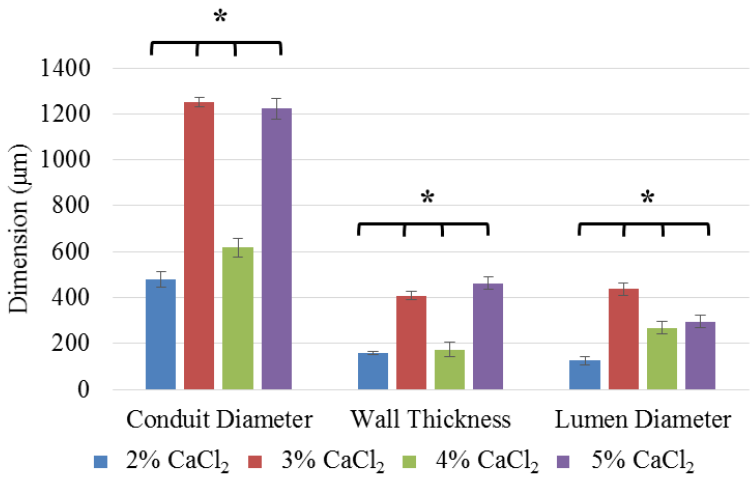

Figure 5.2

Effect of $CaCl_2$ on conduit dimensions (the single asterisk (*) indicates significant differences between groups $p<0.05$).

5.2.3 Effects of Dispensing Parameters on Conduit Dimensions

In this experiment, the effects of dispensing parameters on conduit dimensions were studied. 4% alginate and 4% $CaCl_2$ were used to fabricate alginate conduits, and 3% chitosan and 1.0 M sodium hydroxide were used to fabricate chitosan conduits. Alginate dispensing pressure, $CaCl_2$ dispensing rate, chitosan dispensing pressure, and sodium hydroxide dispensing rate were varied to understand the effect of dispensing rates on conduit dimensions. Figure 5.3 and Figure 5.4 illustrate the effect of the abovementioned parameters on conduit dimensions. Conduit diameter increased as biomaterial or crosslinker dispensing rates increased. Increasing the biomaterial dispensing rate resulted in a greater volume of biomaterial dispensed per unit time, generating enlarged conduits. These also brought thicker walls during extrusion (see Figure 5.3(a) and 5.4(a)).

Increasing the crosslinker flow rate generated more tension on the conduit wall in the radial direction, expanding conduits in a cross-sectional profile that increased both lumen and conduit diameter. No direct relationship was observed between wall thickness and the crosslinker flow rate (see Figure 5.3 (b) and 5.4(b)).

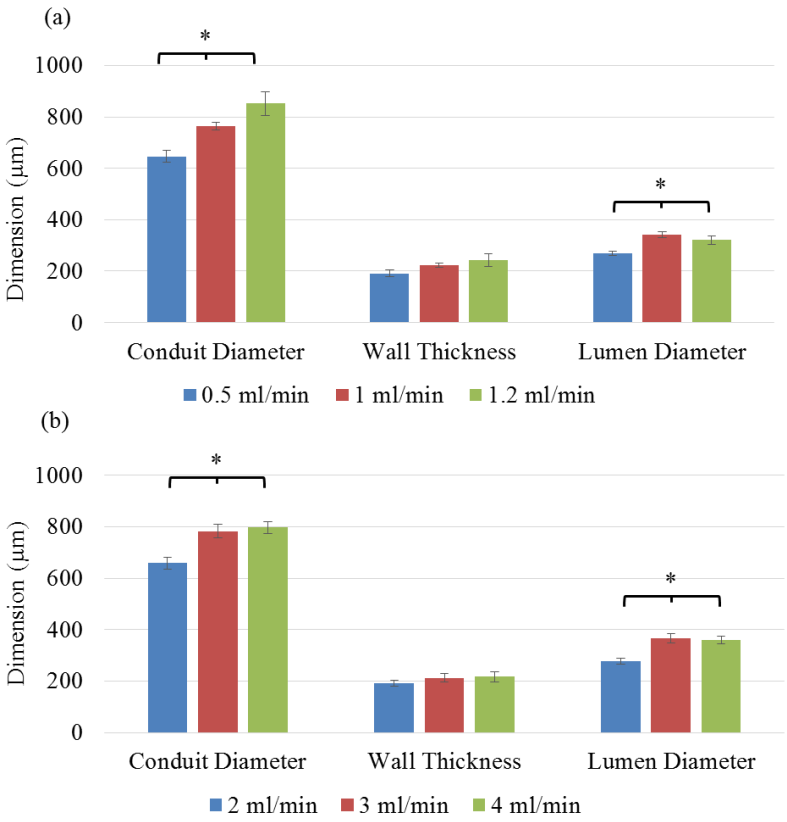

Figure 5.3

Effect of flow rheology on the geometry of conduits: (a) varying alginate dispensing rate, and (b) varying $CaCl_2$ dispensing rate (the single asterisk (*) indicates significant differences between groups $p<0.05$).

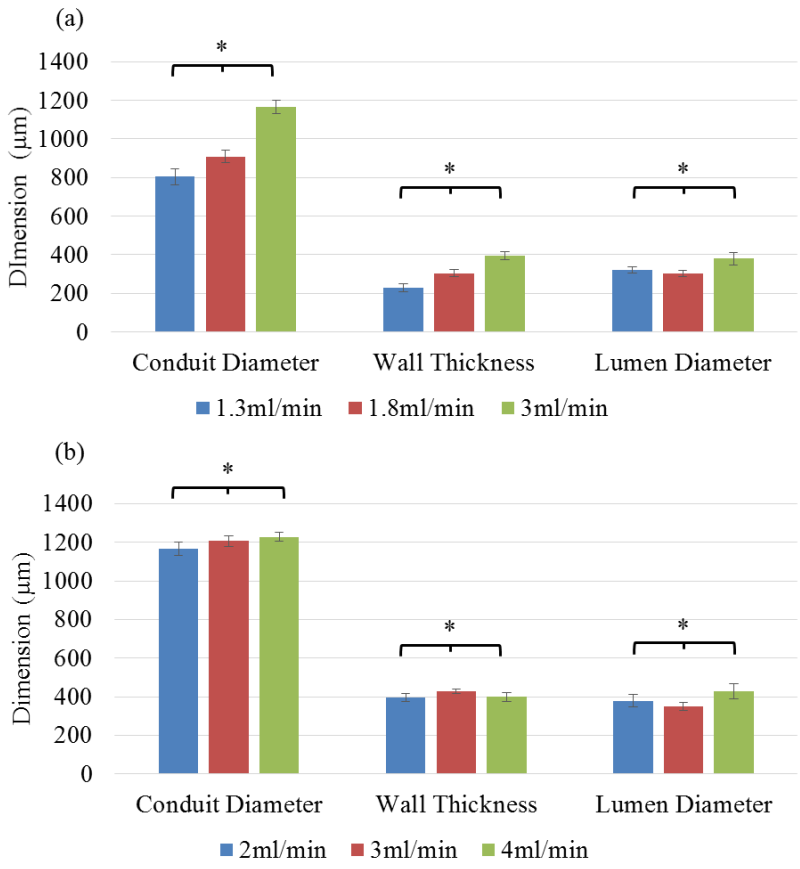

Figure 5.4

Effect of flow rheology on the dimensions: (a) varying chitosan dispensing rate, and (b) varying sodium hydroxide dispensing rate (the single asterisk (*) indicates significant differences between groups $p<0.05$).

Results in Figure 5.5 concluded that the lumen versus vascular conduit ratio (lumen diameter/ conduit diameter) increased as the relative speed between $CaCl_2$ flow and alginate flow increased. This could be explained by increased diffusion rate through the alginate network in addition to higher radial forces exerted on the conduit wall. Although smaller conduit wall thickness (in other words, higher lumen versus conduit

ratio) was desirable, a further increase in this ratio may degenerate the mechanical integrity of conduits and cause non-uniform conduits.

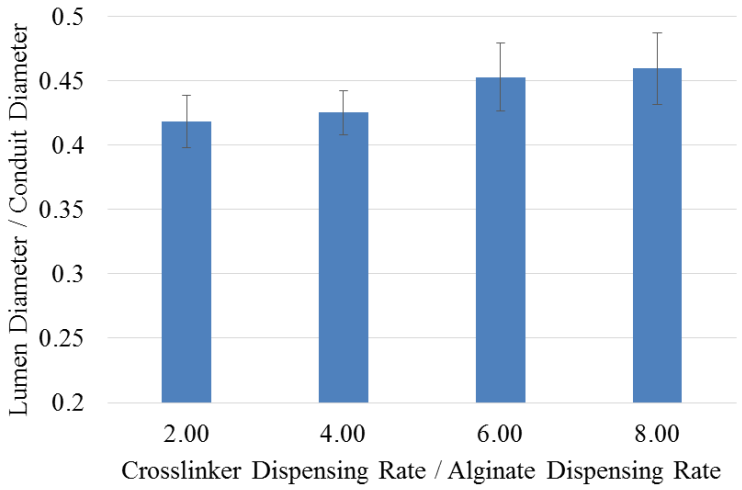

Figure 5.5

Lumen versus vascular conduit ratio with different relative speed between crosslinker and alginate flow.

5.2.4 Result of Fractional Factorial Design

5.2.4.1 Analysis of Conduit diameter

Analysis of variance (ANOVA) results for conduit diameter are presented in Table 5.2. Factors with p-value smaller than 0.05 are considered as significant influential factors, and factors with p-value smaller than 0.01 are considered as very significant influential factors.

Table 5. 2

ANOVA table for conduit diameter

Source	*Deg. of freedom*	*Adj. Mean Square*	*Adj. Sum of Square*	*F Value*	*P Value*	*Significant Level*
Main Effect	5	226837	1134187	176.72	0.001	**
X_1	1	55641	55641	43.35	0.002	**
X_2	1	30240	30240	23.56	0.037	*
X_3	1	12768	12768	9.95	0.006	**
X_4	1	26556	26556	20.69	0.048	*
X_5	1	3440	3440	2.68	0.000	**
2-Way Interaction	7	26519	185636	20.66	0.015	*
X_1X_2	1	6311	6311	4.92	0.113	
X_1X_5	1	55664	55664	43.36	0.007	**
X_2X_3	1	31218	31218	24.32	0.016	*
X_2X_5	1	31154	31154	23.27	0.024	*
X_3X_4	1	22893	22893	17.83	0.053	
X_4X_5	1	12338	12338	9.61	0.02	*
Residual Error	3	26058	26058	20.3		
Total	15	1284	3851			

(a single asterisk (*) represents a significant factor with p-value smaller than 0.05 factors, and a double asterisk (**) represents a very significant factor with p-value smaller than 0.01)

In terms of the resulting conduit diameter, all main factors, including X_1, X_2, X_3, X_4, and X_5, and interaction, including X_1-X_5, X_2-X_3, X_2-X_5, and X_4-X_5, have significant effects. The residual plot shown in Figure 5.6 indicates that the data are normally (Figure 5.6(a)) and independently (Figure 5.6(b)) distributed. There is no predictable pattern observed. An R-square value of 99.7% and an adjusted R-square value of 98.7% are obtained as part of the fractional factorial design. In addition, 30 groups of data were randomly selected from our experiments to build prediction models. Another 10 groups of data were to prove the accuracy of two prediction models. The relative error was calculated for each piece of testing data. The average relative error for conduit diameter prediction model was 13.02 % (see Figure 5.7 (a)). The prediction model was obtained as follows:

$$\begin{aligned} D_O =& -31.83 - 70.30X_1 - 136.58X_2 - 239.27X_3 - 83.49X_4 + 4.06X_5 + 24.90X_1X_2 \\ &+ 26.69X_1X_3 + 48.77X_1X_4 - 0.57X_1X_5 + 19.60X_2X_3 - 23.07X_2X_4 - 0.12X_2X_5 \\ &- 4.90X_3X_4 + 0.08X_3X_5 - 0.14X_4X_5 \end{aligned} \tag{17}$$

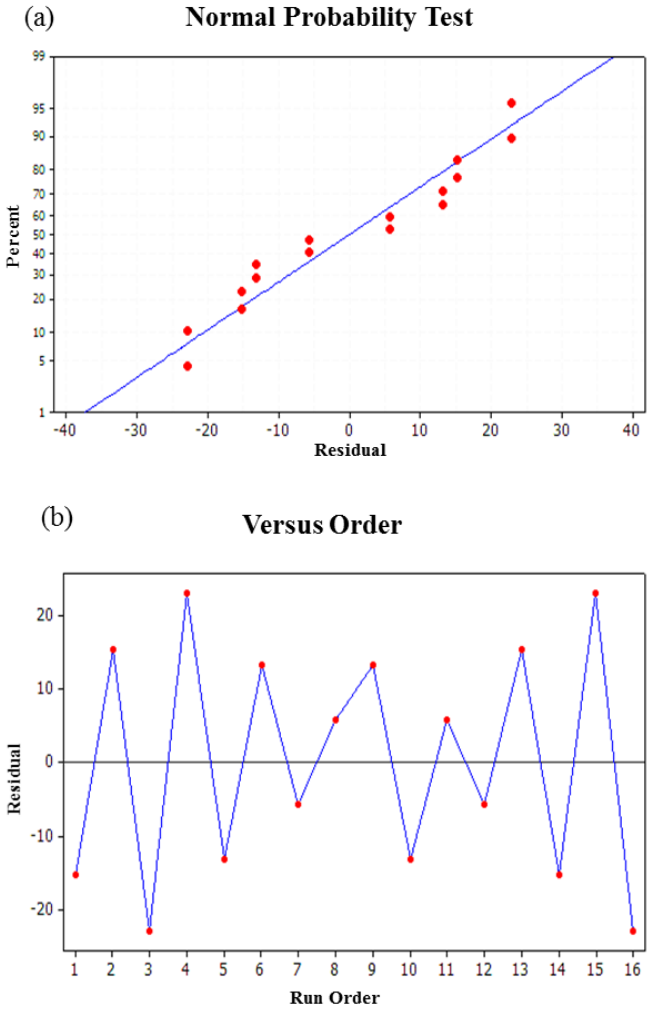

Figure 5.6

Conduit diameter residual plot: (a) plot of residual versus fitted value, indicating that the data are normally distributed, and (b) plot of residual versus observation run number, indicating that the data are independently distributed.

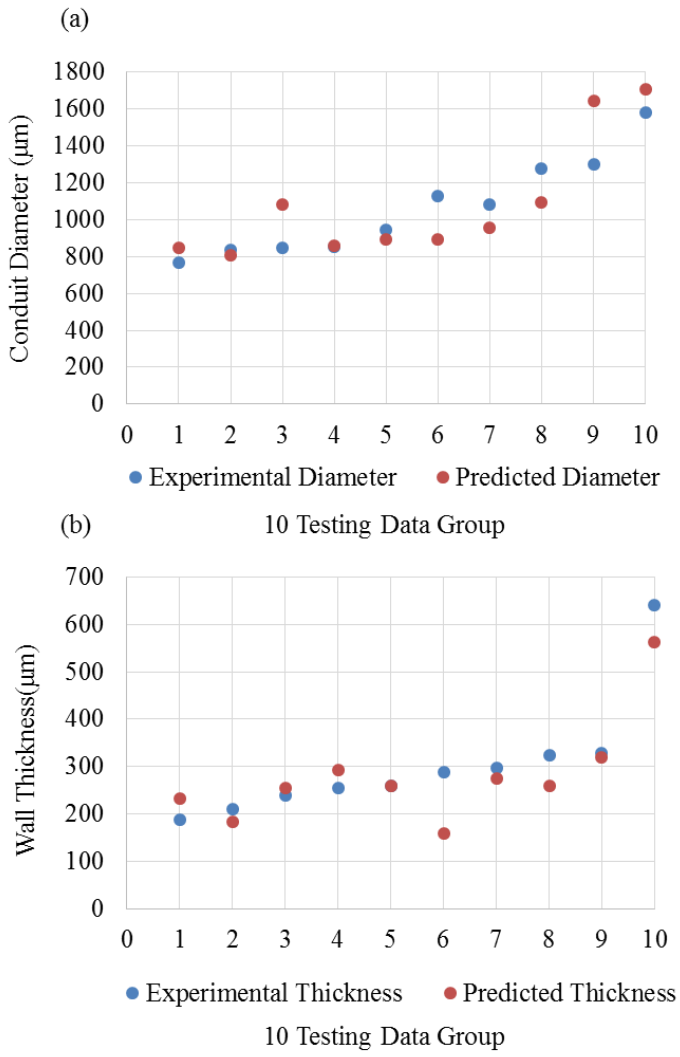

Figure 5.7

Regression model predicted dimension versus experimental dimension: (a) conduit diameter, and (b) wall thickness (sorted from smallest to largest in dimension)

5.2.4.2 Analysis of Wall Thickness

Table 5.3 also shows the significant factors for conduit wall thickness. Table 5.3 depicts that X_1, X_3, and X_5 are factors with significant influence. The influences of two-

way interactions, including X_1-X_5 and X_2-X_5, are significant. The residual plot shown in Figure 5.8 indicates that the data are normally (Figure 5.8(a)) and independently (Figure 5.8(b)) distributed. The *R-Sq* obtained in this model is 98.88%, and the *R-Sq* (*adj*) is 94.38%. Also, another model was obtained for the prediction of the wall thickness. The average relative error of the predictive model for wall thickness is 14.31%. The experimental and predicted data are compared in Figure 5.7(b). The predictive model for wall thickness is shown as follows:

$$WT = -11.46 - 30.49X_1 - 26.05X_2 - 75.73X_3 - 33.24X_4 + 4.09X_5 + 18.37X_1X_2 - 13.35X_1X_3 + 41.40X_1X_4 - 0.64X_1X_5 + 32.20X_2X_3 - 34.43X_2X_4 - 0.22X_2X_5 + 6.28X_3X_4 - 0.03X_3X_5 - 0.04X_4X_5 \quad (18)$$

Table 5. 3

ANOVA for the wall thickness.

Source	*Deg. of freedom*	*Adj. Mean Square*	*Adj. Sum of Square*	*F Value*	*P Value*	*Significant Level*
Main Effect	5	64192	320962	22.81	0.002	*
X_1	1	38388	38388	13.64	0.014	*
X_2	1	303	303	0.11	0.756	
X_3	1	36572	36572	13	0.015	*
X_4	1	2452	2452	0.87	0.393	
X_5	1	243246	243246	86.43	0.000	**
2-Way Interaction	5	19549	19549	6.95	0.027	*
X_1X_3	1	13386	13386	4.76	0.081	
X_1X_5	1	40195	40195	14.28	0.013	*
X_2X_4	1	10707	10707	3.8	0.190	
X_2X_5	1	22209	22209	7.89	0.038	*
X_3X_4	1	11247	11247	4	0.102	
Residual Error	5	2814	14071			
Total	15					

(The single asterisk (*) represents a significant factor with p-value smaller than 0.05 factors, and the double asterisk (**) represents a very significant factor with p-value smaller than 0.01).

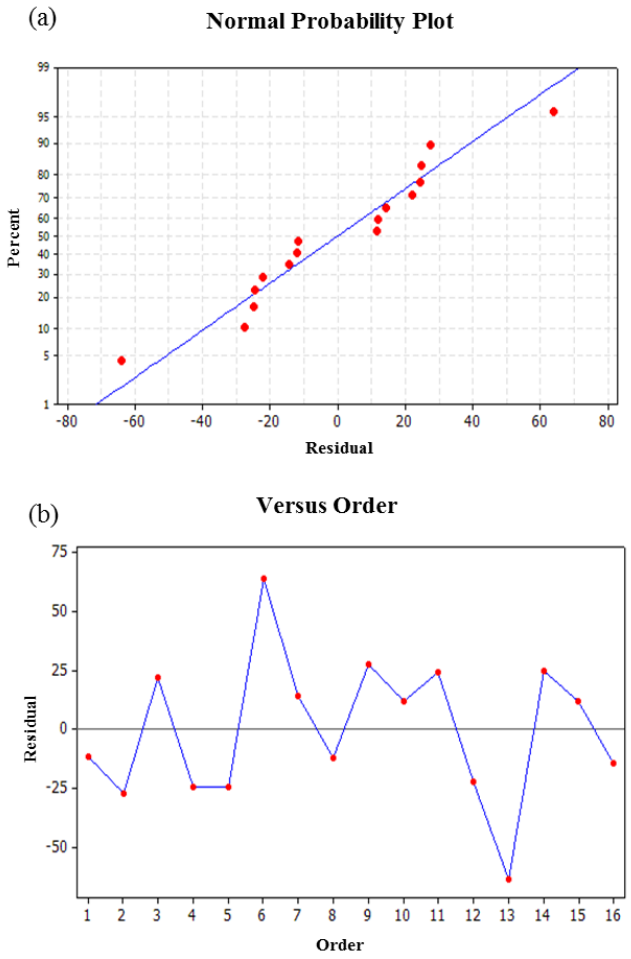

Figure 5.8

The wall thickness residual plot: (a) plot of residual versus fitted value indicates the data are normally distributed, and (b) plot of residual versus observation run number indicates the data are independently distributed.

Using the formulas obtained in Equations (17)-(18), conduit lumen diameter (D_l) can be calculated as in Equation (19). If the dimensions of a desired conduit are known, and the

material's concentrations and available nozzle size are also given, the fabrication parameters - alginate dispensing pressure and calcium chloride dispensing rate - can be calculated using Equations (17) and (18). By predicting the dimensional properties, conduits can be printed with controlled dispensing parameters (alginate dispensing pressure and calcium chloride dispensing rate), resulting in gradually changed dimensions to fabricate a network biomimetically. The result of factorial design can be obtained in Appendix F.

$$D_l = D_o - 2 * WT \tag{19}$$

5.2.5 Cell Viability as a Function of Dispensing Parameters

An empirical mathematical model was derived to predict cell viability V (%) at 12 hrs. Two variables, spaces between nozzles (X_1-cm) and alginate dispensing pressure (X_2-psi), are considered as independent prediction factors. The predicted cell viability and experimental cell viability are plotted in Figure 25 for both nozzle G16-23 and G16-26. According to Figure 5.9, the predicted cell viability value is relatively close to the experimental cell viability value. The average percentage of error of the prediction model is small (6.43%).

$$V = -213.68X_1^2 + 33.61X_1 - 0.07X_2 - 0.2 \tag{20}$$

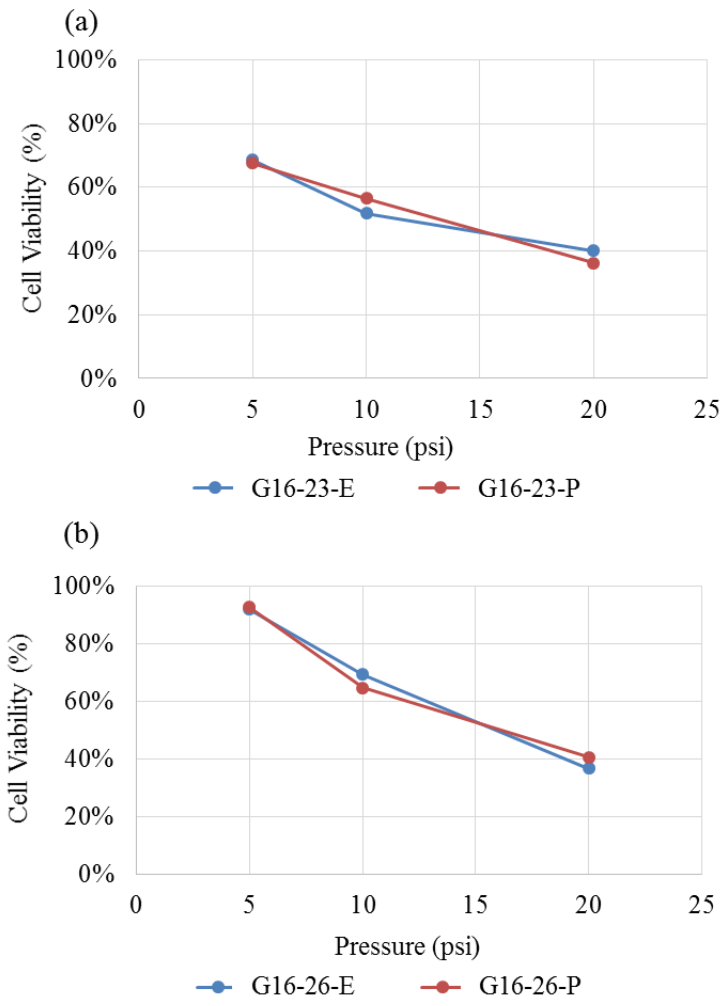

Figure 5.9

Experimental and predicted cell viability (E: experimental; P: predicted): (A) for nozzle G16-23; (B) for nozzle G16-26.

Figure 5.10 plots cell viability results under varying maximum shear stresses. Cell viability decreases dramatically as maximum shear stress increases due to shear-stress-induced cell damage. The higher the shear stress, the lower the cell viability.

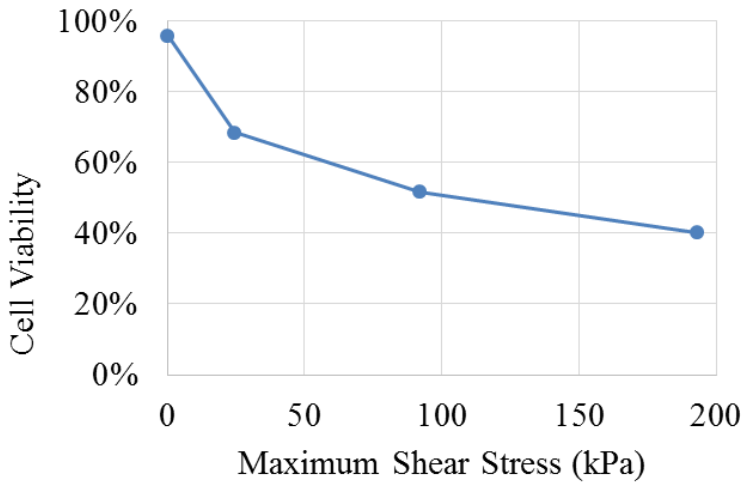

Figure 5.10

Cell viability under different maximum shear stresses.

5.3 Discussion and Conclusion

In this chapter, a dimensional characterization of conduits through studying multiple biomaterials and their dispensing rheology was performed. The biomaterial concentration, crosslinker concentration, biomaterial dispensing pressure, and crosslinker dispensing rate were explored individually to determine their effects on the conduit dimensions. Furthermore, a five-factor factorial design was carried out.

Figure 5.11(a) shows a partially crosslinked alginate conduit that was fabricated with 4% alginate and 2% $CaCl_2$. Due to low Ca^{2+} concentration in the 2% $CaCl_2$ solution, only a small portion of the deposited alginate was crosslinked. This could be alleviated by increasing the concentration of $CaCl_2$. The wall thickness of conduits is critical for their functionality in both delivering perfused media through the lumen and allowing its diffusion for viability of encapsulated cells. The diffusion limit for hydrogels is around 200 µm, which indicates that if the wall thickness of fabricated conduit is smaller than 200 µm, there is a high chance of cell

viability. However, smaller wall thickness is not always desirable. The mechanical and structural integrity of the conduit decreases as the wall thickness decreases [111]. Figure 5.11(b) illustrates a conduit with a thin wall, in which the conduit was collapsed at several locations due to weak mechanical integrity.

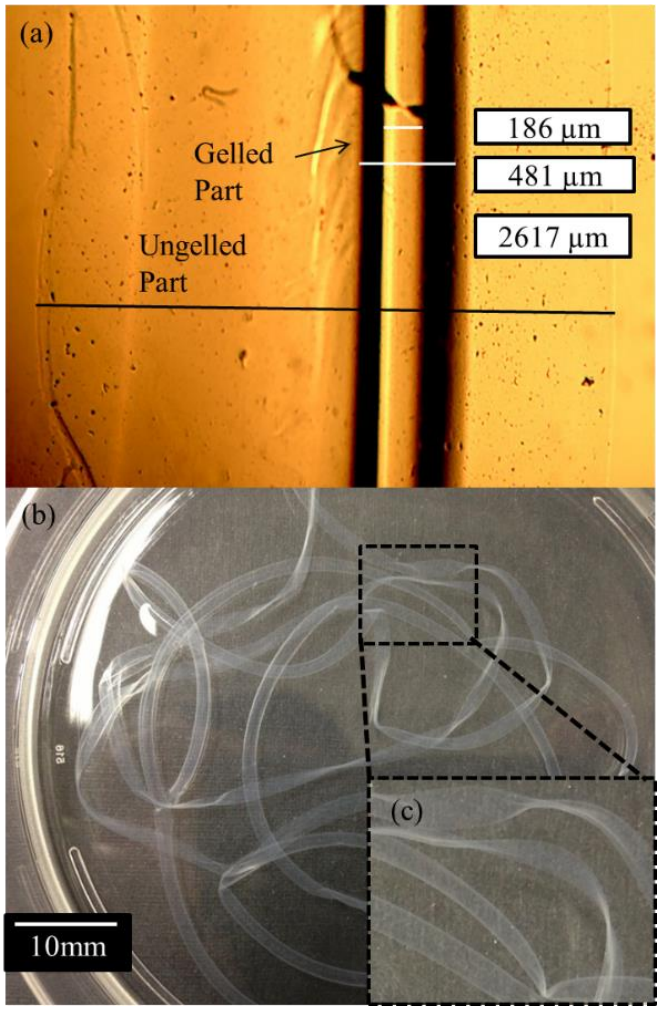

Figure 5.11

Issues in fabrication: (a) partially crosslinked alginate, (b)-(c) relatively weak structure bent and collapsed due to small wall thickness.

The regression model presented in this chapter is a theoretical approach. From a manufacturing point of view, factors have boundaries, and their boundary values are sometimes confined by other factors. For example, the usability of the smallest $CaCl_2$ concentration is confined by alginate concentration, alginate dispensing pressure, and $CaCl_2$ dispensing rate. If one does not take all of these factors into consideration and considers only a few, a printed conduit might not be fully gelled. The printed alginate with limited gelation cannot be used for further purposes, such as printing a conduit in 3D or carrying out perfusion studies. In this case, conduits can be directly extruded into a crosslinker solution to facilitate complete gelation. In addition, changes in some factors may lead to changes in others. For instance, if one wants to get a smaller-diameter conduit and considers using a smaller coaxial needle in order to dispense alginate without clogging the nozzle, either the alginate dispensing pressure must be increased or a lower-concentration alginate must be used. Either option will generate other influences on the resulting conduit diameter.

The main purpose of integrating a biomimetic conduit within engineered tissues is to improve the media exchange rate. Thus, in terms of media transportation, theoretically, the wall thickness of the conduit should be as small as possible. The thinner the wall thickness is, the higher the media exchange rate that can be obtained. In a porous biomaterial network, the media exchange mainly depends on diffusion. The diffusion capability of biomaterial is limited. For hydrogels, the diffusion limit is around 200 μm, which indicates that if the wall thickness of a fabricated conduit is below 200 μm, there will be a greater chance of achieving higher cell viability. However, thin wall thickness can also cause problems because the mechanical properties of conduits decrease as the wall thickness decreases. This can result in mechanical integrity issues such as the collapse or rupture of conduits.

CHAPTER VI

EVALUATION OF MEDIA PERFUSION CAPABILITIES

Although great progress has been made in tissue engineering, there are still limitations with engineering and manufacturing thick tissues. The engineered tissue constructs are limited to a few centimeters in thickness, which is primarily due to the lack of an efficient media exchange system. Embedding perfusable conduit thus has a great potential to increase media exchange capabilities. In this chapter, bioprintable perfusable conduits were fabricated for perfusion testing. The effects of dispensing parameters and media flow characteristics on resulting conduits were experimentally analyzed

6.1 Materials and Method

6.1.1 Materials

Prior to making a hydrogel solution, sodium alginate powder (Sigma Aldrich, United Kingdom), chitosan powder (Sigma Aldrich, Iceland), and calcium chloride powder (Sigma Aldrich, United Kingdom) were treated with UV light for sterilization three times for 30 minutes per cycle. Ultraviolet-sterilized sodium alginate was dissolved in deionized water to make 4% solutions, and UV-sterilized chitosan was dissolved in 1.0 M acetic acid (Fluka Analytical, Germany) to make 3% solutions. Solutions were mixed with a magnetic stirrer (HANNA Instruments, U.S.A.) until homogeneity was reached. Similarly, the crosslinking solution was prepared by dissolving UV-sterilized calcium chloride in ultra-purified water (Invitrogen^{TM} Life Technologies, U.S.A.) at 4% (w/v). 1.0 M sodium hydroxide (Fluka Analytical, Germany) is used to crosslink the chitosan solution.

6.1.2 Fabrication of Conduits for Perfusion

Conduits used for the perfusion experiment were custom designed. In order to insert a needle into the conduit and conduct the perfusion, the conduit should have a relatively large

lumen diameter. Thus, a large calcium chloride dispensing rate was applied. A coaxial nozzle consisting of a 14 gauge (1.54 mm I.D. and 1.83 mm O.D.) outer needle and 23 gauge inner needle (0.33 mm I.D. and 0.65 mm O.D.) was made especially for fabrication of conduits for perfusion experiments. During fabrication, the alginate dispensing pressure was set at 3 psi, and the calcium chloride dispensing rate was set at 16 ml/min. The dimensions of alginate conduits with different alginate concentrations were shown in Figure 2.2B. The 4% alginate conduits had the smallest conduit diameter and lumen diameter. Combinations of several fabrication parameters (alginate dispensing pressure and calcium chloride dispensing rate) were tested to obtain the best match for a 20 gauge flexible-tip needle. The criteria for the fabrication parameter selection is that the lumen diameter of the dispensed conduit should be exactly the same as the 20 gauge flexible-tip needle's outer diameter, such that the needle can be inserted into the conduit tightly and no leakage should be observed at the needle and conduit connection junction.

6.1.3 Media Perfusion System

The main function of a human blood vessel is to provide nutrients and oxygen to surrounding tissues as well as take away the waste. Therefore, it is essential to evaluate the media diffusion capabilities of the engineered conduits. To test the media diffusion and perfusion capability of conduits, a customized system was developed for providing continuous media flow through fabricated conduits. Figure 6.1 demonstrates the experimental perfusion system in a tissue culture incubator (Panasonic Healthcare Company of North America, U.S.A.). It consisted of a compact periodic fluid pump (Cole-Parmer, U.S.A.) to perfuse media and simulate blood flow in nature, a culture media reservoir with 1 liter capacity, and a customized culture chamber with a clear cover to prevent evaporation. Medical-grade rubber tubes (PharMed, U.S.A.) and plastic adaptors (Nordson, U.S.A.) were used to connect the three main components of the system, providing circulated media flow inside this system. Cell media was pumped from the media reservoir, through the pump, into the conduit, and then circulated back to the media reservoir. Flexible tip needles were mounted to the culture chamber to connect conduits with the

tubing system, serving as inlets/outlets for circulating culture media. The size of the needles was selected according to the dimensions of the conduits. Micro-vessel clips were used to tighten the joint between nozzle tips and conduits, preventing possible leakage of media. Eight-hour perfusion experiments were conducted through the perfusion system, and no leakage or occlusion was observed in the conduits. At the connection part of needles and conduit, leakage occurred sometimes due to the needle insertion process and the needle size selection.

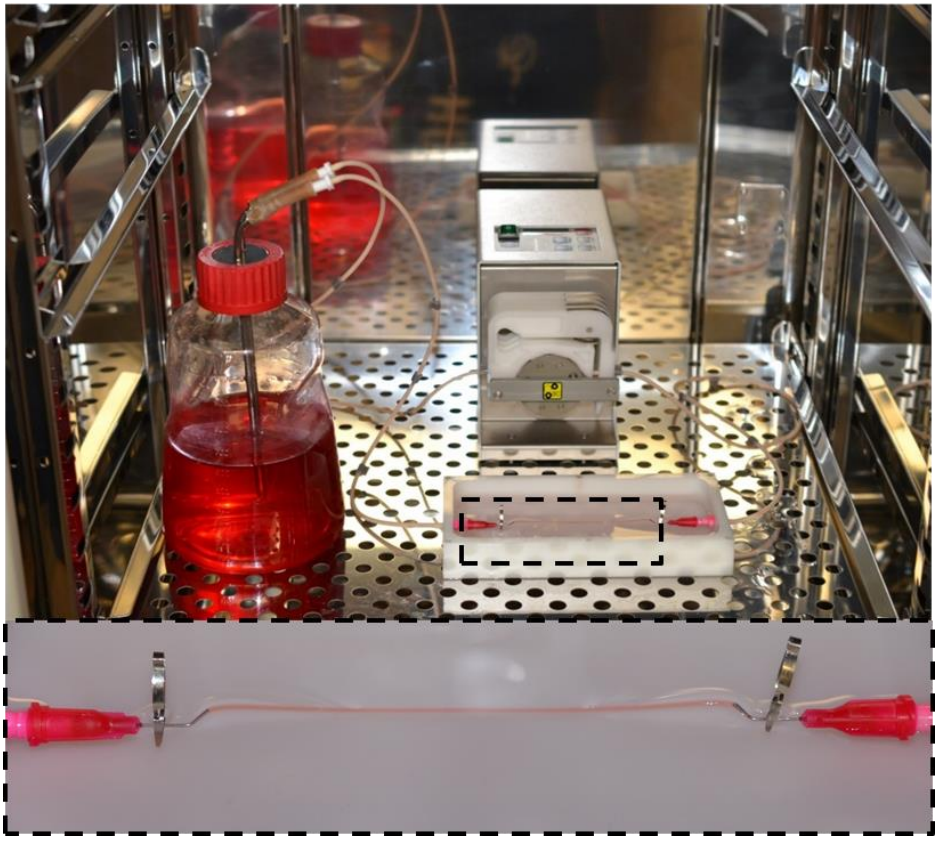

Figure 6.1

Media perfusion system

6.1.4 Perfusion and Diffusion Characterization

The 3%, 4%, and 5% alginate and 4%, 5%, and 6% calcium chloride solutions were used for fabrication and perfusion experiments in order to explore the permeability of conduits. Cell culture media was perfused through an 8 cm conduit. Conduits were collected with a wide-mouth container filled with calcium chloride. After fabrication, conduits were soaked in calcium chloride solution for 12 hours for easy manipulation. The concentration of calcium chloride used to soak conduits was the same as the concentration of the calcium chloride used to fabricateconduits. Directly after printing, conduits were soft and mechanically weak; this made the insertion of needles very difficult. This finding is also consistent with the literature, which pointed out that the elastic modulus of alginate increases as the gelation time increases, within 24 hours [107]. Perfusion experiments in Section 5.2.5 were conducted at 1 hour with a 3 ml/min perfusion flow rate setting. In all perfusion experiments, the original length of conduits was fixed at 8 cm.

6.1.5 Embedding a Vasculature System into Bulk Hydrogel

In order to embed a vasculature system into bulk hydrogels, the vasculature system was fabricated by automatically printing as well as manually patterning. A petri dish was prepared and coated with 3-5 mm 4% alginate solution on the bottom. A coated petri dish was then fixed to a horizontal shaker and underwent 3-5 minutes of shaking to get a uniform distribution with a flat surface. The alginate vasculature system was then printed or manually patterned on top of the alginate-coated petri dish to get a zigzag pattern with arc turns (see Figure 6.2(a)). Another layer of alginate solution was then slowly pulled onto patterned conduits without introducing any air bubbles or clearance between layers (see Figure 6.2(b)). A shaker was also used here to ensure an even surface for the second layer. A 4% calcium chloride solution was then carefully sprayed onto the petri dish to cover the whole surface of the alginate. The entire structure was merged in a calcium chloride solution until gelation was fully completed, after which vasculature system was embedded into bulk alginate gel (see Figure 6.2(c)). A vasculature system embedded in

alginate hydrogel by automatically printing and manually patterning is shown in Figures 6.2(d) and 6.2(e), respectively. The printed vasculature system (Figures 6.2(d)) was better organized than the manually patterned one (Figures 6.2(e)).

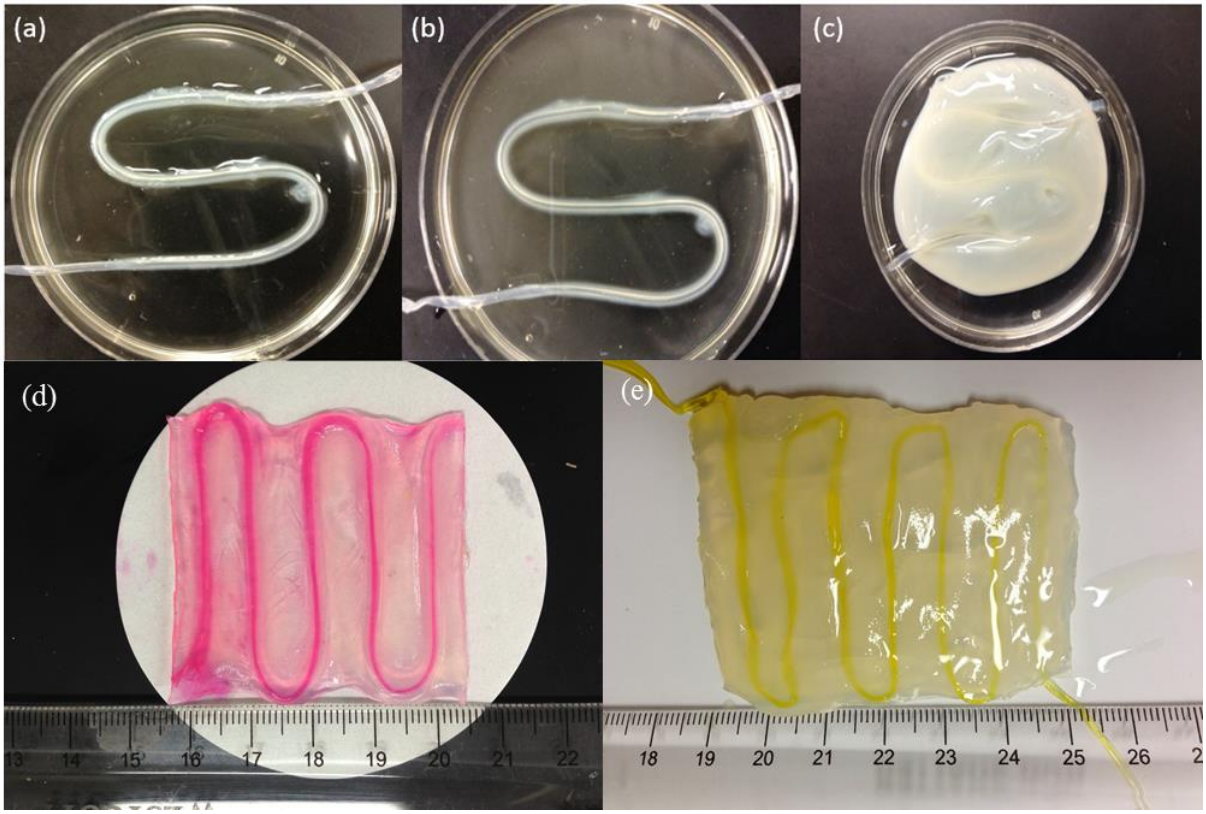

Figure 6.2

Embedding vasculature system into bulk hydrogel: (a-c) the embedding process, and (d-e) embedding vasculature system into bulk hydrogel by (d) automatically printing, and (e) manually patterning.

6.1.6 Quantitative Measurement of Diffusion

The diffusivity of small molecules in alginate hydrogels was measured by perfusing a solution of fluorescein (Sigma Aldrich, United Kingdom) (0.003/L) into the 4% alginate conduits. Alginate conduits were printed into bulk alginate hydrogel as described in the previous section. As soon as conduits were filled, perfusion was stopped and two vascular clips were used at two ends of conduit to prevent solvent solution flow-out. Fluorescent images were taken using a microscope every 1 minute up until 10 minutes. The images were then analyzed by Matlab R2013a to estimate the diffusivity of fluorescent molecules in alginate gel. The diffusivity of fluorescein dye in 4% alginate will be calculated by the method mentioned in the literature [108].

To determine the permeability of alginate conduits, fluorescein dye was dissolved into cell media and pumped through the conduits. The cell media was pumped through conduits at a flow rate of 3 ml/min. A fluorescent image was acquired sequentially every 1 minutes up until 10 minutes using a fluorescent microscope (Leica Microsystems, Germany). The intensity information of fluorescent images was analyzed by Matlab R2012a. The permeability coefficients of 4% alginate conduits were estimated using the equations described in the literature [109].

6.1.7 Statistical Analysis

In dimensional characterization experiments, more than 50 pieces of data were obtained by measuring different conduits and different sections of the perfused conduits. The data shown in those experiments are an average of all 60 pieces of data. The statistically significant difference was determined using the two-tailed student's t-test. Groups with a significance level of $p<0.05$ were considered as significant. In perfusion experiments, with the sample size n=3, the data points shown in the figures were averages of the three.

6.2 Results

6.2.1 Fabrication of Chitosan and Alginate Conduits

The fabricated alginate and chitosan conduits are shown in Figure 6.3. Alginate conduits had relatively better mechanical and structural integrity compared to that of chitosan [111]. The fabricated alginate conduits were continuous and had uniform diameter (see Figure 6.3(a)). As shown in Figure 6.3(b), although uniform chitosan conduits were obtained, their structural integrity was limited so that they were fragile and ruptured easily.

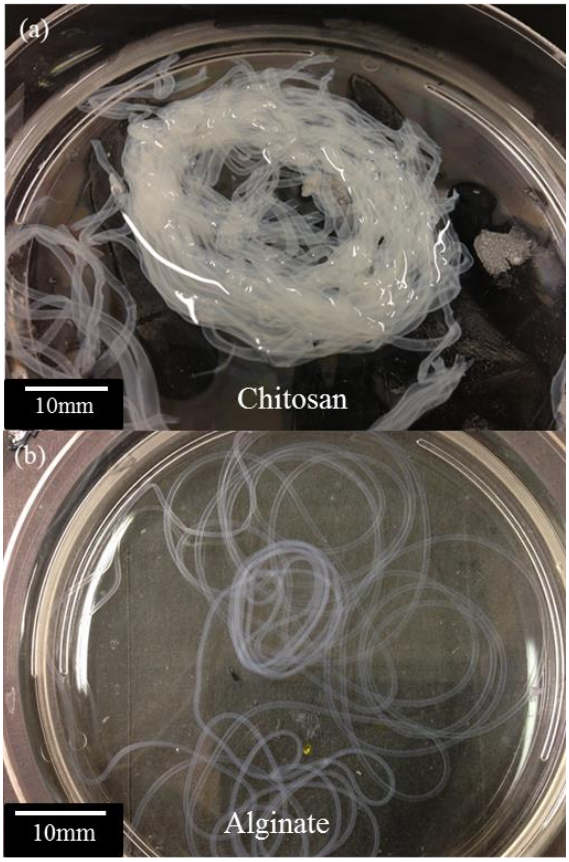

Figure 6.3

Conduits: (a) alginate conduits have acceptable mechanical strength and structural integrity and (b) chitosan conduits are fragile and easy to rupture.

6.2.2 Effect of Perfusion Rate on Conduit Dimensions

The flow rate of cell media was set as 1 ml/min, 2 ml/min, and 3 ml/min, respectively, to determine the influence of media perfusion rate on the fabricated conduit and its diffusion capability. Figure 6.4 shows the media flow rate's influence on conduit dimensions, and Figure 6.4(a) shows the perfusion rate's influence on conduit dimensions. The lumen diameter and conduit diameter increased when the perfusion rate increased. A trend can be observed in Figure 6.4: a higher perfusion flow rate tended to alter conduit dimensions more after 1 hour of perfusion. This phenomenon can be explained by burst pressure. A higher perfusion rate corresponds to a larger burst pressure inside the conduit. A larger burst pressure would enlarge the conduit diameter further. As shown in Figure 6.4(b), perfusion time also had an influence on the conduit dimensions. A 3 ml/min perfusion rate was chosen because a larger perfusion rate is supposed to have more significant results. Cell media was perfused at 3 ml/min for 1 hour and 3 hours. The diameter of the conduit was measured after perfusion. The results show that perfusion flow with a longer perfusion time has a greater influence on conduit dimension changes.

The elongation of a conduit with cell media perfusion was also measured. The differences in elongation for a conduit with cell media perfused inside were not significant. All samples were elongated from the original 8 cm to 8.4 cm. The formation of conduit elongation is mainly due to the weight. Elongation terminated as long as conduits reached the bottom of the perfusion chamber. The perfusion rate and perfusion time had little to no influence on it, which may indicate that shear stress inside the conduit during perfusion was not large enough to have any effect on the conduit dimensions.

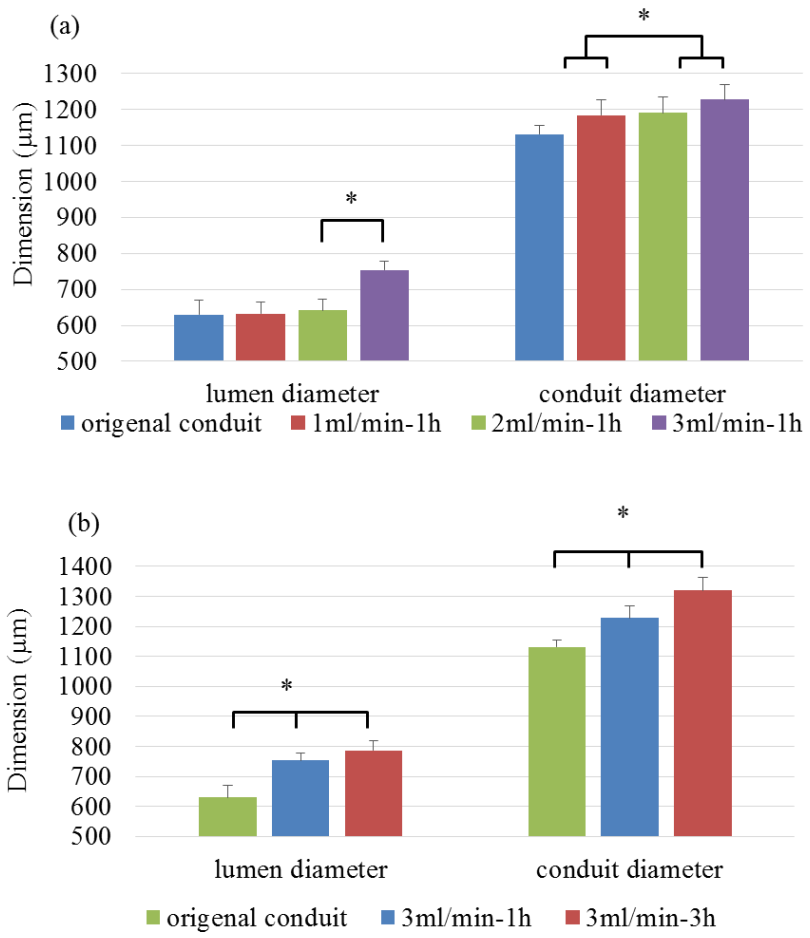

Figure 6.4

Media influence on conduit dimensions: (a) 1 hour perfusion experiment with changing perfusion rate, and (b) the influence of perfusion time on conduit dimensions.

6.2.3 Effect of Media Perfusion Rate on Diffusion Rates

When the conduit dimensions change, the diffusion rate changes accordingly. Figure 6.5 plots the conduit diffusion rate under different perfusion rates. Similarly, Figure 6.5(a) shows the influence of perfusion rate on the diffusion rate. With a higher perfusion rate, the conduit has a higher diffusion rate. Figure 6.5(b) demonstrates the influence of perfusion time on the diffusion

rate. The conduit diffusion rate increased as the perfusion time increased. The diffusion rate shown in Figure 6.5(b) is the average diffusion rate per hour. The filtrated cell media was collected once per hour. The data in the 3 ml/min-2h group only included the cell media diffused through the conduit in the second hour.

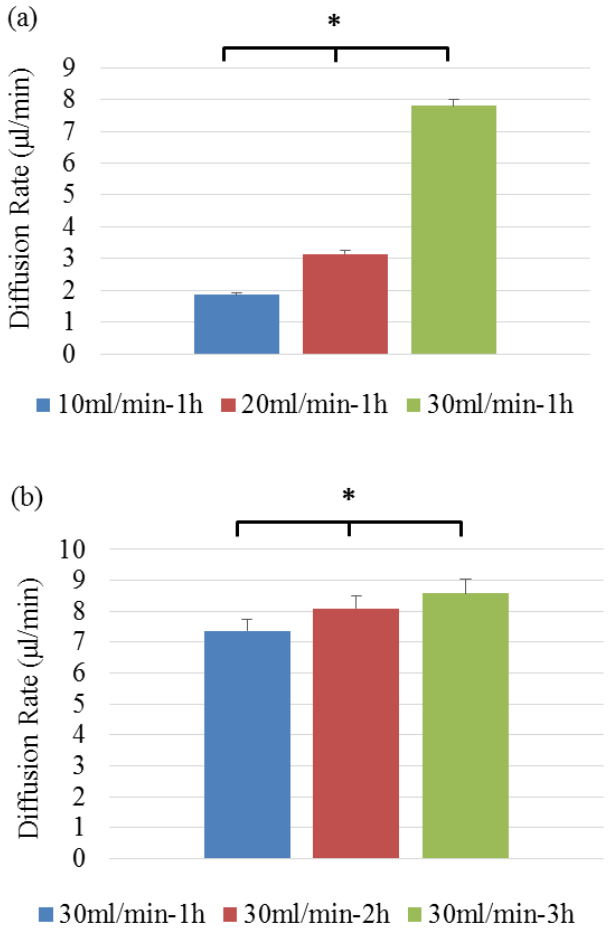

Figure 6.5

Influence of perfusion parameters on conduit dimensions: (a) 1-hour perfusion experiment, and (b) influence of perfusion time.

The main reason for the diffusion rate change is the change in the conduit diameter. Conduits pumped with higher perfusion rates tend to have larger lumen diameter and thinner wall thickness, which increases the diffusion rate. Similarly, because perfusion time also has a significant effect on conduit dimensions, a conduit perfused for a longer time tends to have a larger lumen diameter and smaller wall thickness, thus having a higher diffusion rate.

6.2.4 Perfusion and Diffusional Characterization

Both biomaterial concentration and crosslinker concentration have significant influence on conduit diffusion rate. Figure 6.6 shows the diffusion rate of cell media in 3%, 4%, and 5% alginate conduits crosslinked by 4%, 5%, and 6% $CaCl_2$. The 3% conduits crosslinked by 4% $CaCl_2$ were fragile due to their weak mechanical properties as well as thin wall thickness. They were not suitable for the perfusion experiment, so their data were not included in Figure 6.6. Although the difference in diffusion rate is not significantly different between the conduit groups crosslinked by 5% $CaCl_2$ and 6% $CaCl_2$, the diffusion rate changing trend is clear: as the diffusion rate of conduits decreased as alginate and $CaCl_2$ concentration increased. This result is consistent with a pervious study [51], which also demonstrated the permeability of calcium alginate decreased as calcium concentration increased.

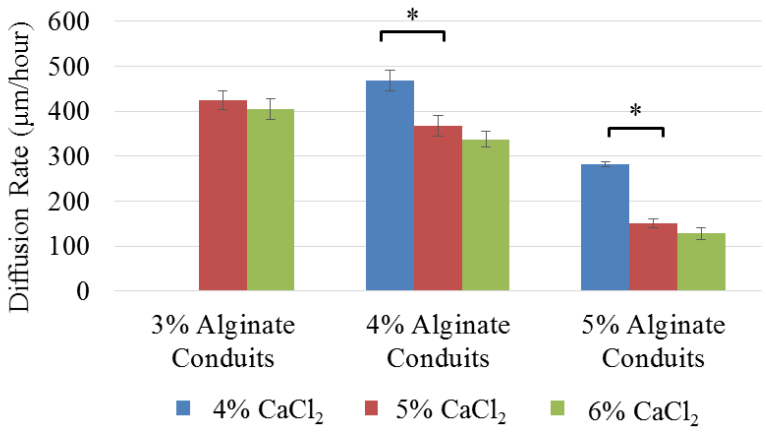

Figure 6.6

Perfusion and diffusional characterization of 3%, 4%, and 5% alginate conduits (the single asterisk (*) indicates significant differences between groups $p<0.05$).

6.2.5 Quantitative Measurement of Small Molecular Diffusivity

In order to calculate the permeability of an alginate vasculature system, measurement of fluorescent diffusivity in alginate is needed. The evaluated diffusivity D is 3.3×10-10 cm^2/s, which is much smaller than the value obtained in the literature [108]. Figures 6.7(a) and (b) show the fluorescent figures of embedded vasculature system filled with fluorescent dye at minutes 0 and 10. The fluorescent dye was successfully diffused into bulk alginate over time (see Figure 6.7(c)).

Fluorescent dye was perfused into the printed vasculature system at a dispensing rate of 3 ml/min. Fluorescent figures of embedded vasculature system at minutes 0 and minute 10 were shown in Figures 6.7(e) and (f), respectively. The fluorescent intensity was increased during the first 3 minutes and remained unchanged thereafter. Because the entire intensity curve cannot be obtained from the experiment, the quantitative permeability coefficient cannot be calculated (see Figure 6.7(d)).

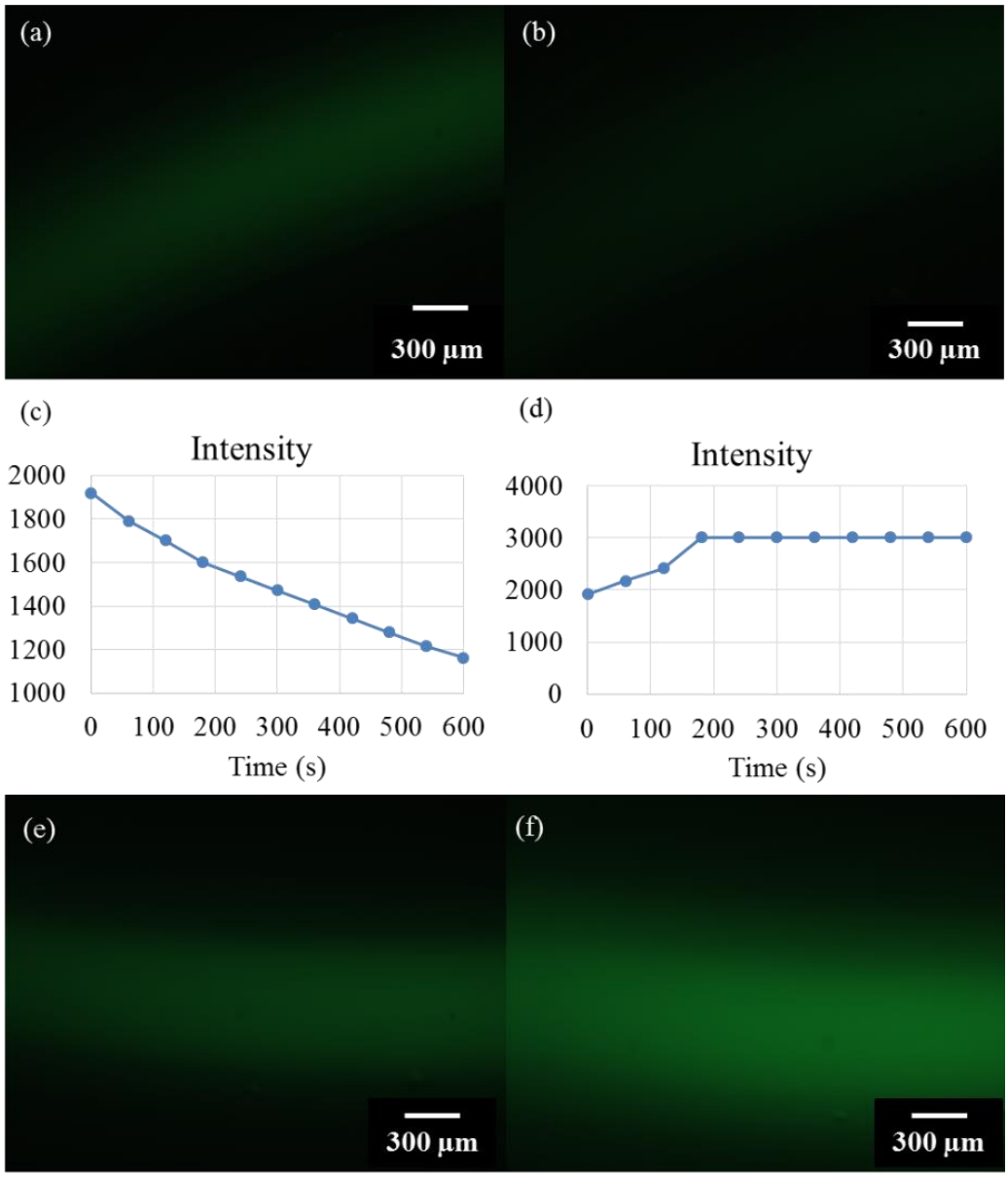

Figure 6.7

Vascular system filled with fluorescent cell media. As soon as the vasculature system was filled, the perfusion was stopped. Fluorescent microscopy images showing the fluorescein intensity: (a) fluorescent image taken at 0 minutes, (b) 10 minutes, and (c) intensity over time. The fluorescent cell media was pumped through the vasculature system at a flow rate of 3 ml/min. Fluorescent microscopy image showing the fluorescein intensity: (d) intensity over time, (e) fluorescent image taken at 0 minutes and (f) 10 minutes.

6.3 Discussion and Conclusion

In this chapter, perfusion capabilities of conduits were studied. The effect of perfusion rate and perfusion time on conduit dimensions and diffusion rate were analyzed. Results showed that a higher perfusion rate resulted in a larger alteration in conduit diameters, which might be due to larger burst pressure. Similar results were also obtained for perfusion time. A longer perfusion time resulted in a larger alteration in conduit diameter. Perfusion experiments were also done to study the diffusion rate changes. With a higher perfusion rate, the conduit had a higher diffusion rate. Also, longer perfusion time resulted in a greater diffusion rate. Theoretically, the diffusion property of one material is fixed and should not be changed over time. However, experiments in this chapter altered the conduit dimensions during perfusion experiments. The change in diffusion rate is due to conduit dimension changes during the perfusion process. Elongation experiments were also performed. No elongation difference was observed in perfused conduits during experiments due to the elongation being terminated as long as the conduit reached to the bottom of the perfusion chamber. Perfusion and diffusional characterization experiments were carried out to understand the diffusional capacity of conduits. The diffusion rate of conduits decreased as the alginate concentration increased. This result also shows that the 3% group had larger pores than the 4% and 5% groups in the polymer network.

Clearance was observed between the alginate vasculature system and bulk alginate (see Figure 6.8), which is due to the residual of Ca^{2+} ions on the alginate vasculature system's outer wall. The clearance between the alginate vasculature system and bulk alginate hydrogel was observed even before the crosslinking process (see Figure 6.8(a)). During the crosslinking process, this clearance was further enlarged because of the shrinkage property of the alginate crosslinking process. In Figure 6.8(b), the alginate vasculature system was manually patterned into bulk hydrogel, and in Figure 6.8(c), the alginate vasculature system was directly printed into bulk hydrogel. Fully crosslinked bulk alginate was sliced and viewed using a light microscope (Leica Microsystems, Germany), as shown in Figure 6.8(c). Vasculature systems printed into bulk alginate still retained their lumen (see Figure 6.8(c)). No obvious deformation was observed

under the microscope. However, the clearance between the alginate vasculature system and bulk alginate hydrogel remains an issue. In Chapter 4, the calculated conduit gelation time ranged from 0.6 min to 12 min. The lumen diameter and vasculature system diameter of printed conduits were 721 μm and 1295 μm, respectively. The calculated minimum gelation time for conduits was 4.82 min. Thus, theoretically, the vasculature system should be able to crosslink with bulk alginate. However, to ensure fabrication of conduits with large and uniform lumen sections into which to insert needles during the perfusion experiment, the $CaCl_2$ solution dispensing rate was set at 16 ml/min. A high pressure was present inside the conduit lumen during crosslinking due to the high dispensing rate of $CaCl_2$. This will greatly accelerate the crosslinking process by increasing the Ca^{2+} diffusion rate. Thus, the directly printed alginate vasculature system cannot be crosslinked with bulk alginate hydrogel, and clearance was observed between them. Comparing Figure 6.8(b) and Figure 6.8(c), vasculature systems that are manually patterned had larger clearance than that of the directly printed one, which is due to more residual of Ca^{2+} ions on the outer wall of the manually patterned conduits. For embedding the vasculature system into bulk hydrogels manually, conduits were printed directly into calcium chloride pools in petri dishes and soaked in the solution for over 30 minutes until they became fully crosslinked, and then they were soaked in $CaCl_2$ solution over one night for easy manipulation. Thus some residual of Ca^{2+} ions existed on the conduit outer wall which resulted in a big clearance between the vasculature system and bulk hydrogel.

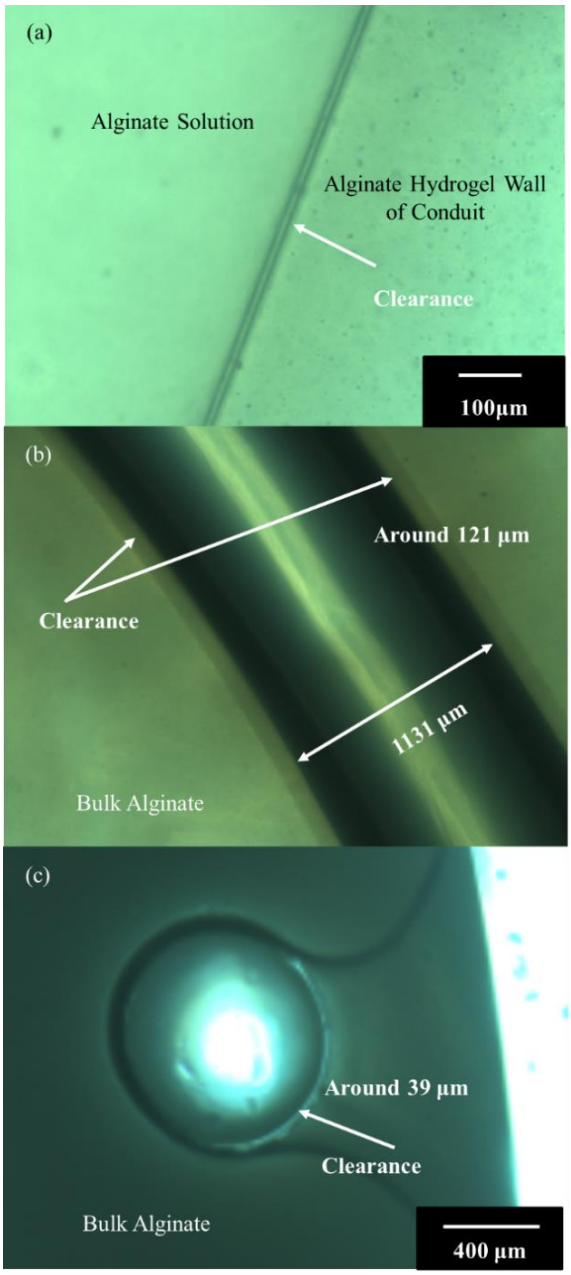

Figure 6.8

Clearance was observed between alginate vasculature system and bulk alginate hydrogel: (a) clearance was observed between alginate solution and alginate vasculature system, (b) manually patterned alginate conduit in bulk alginate hydrogel, and (c) printed alginate conduit in bulk alginate hydrogel. Bulk alginate was sliced and sectioned to show the clearance.

Although the clearance was not very significant compared to the dimension of conduits, it had a great influence on the diffusion process and experiments to characterize the conduits' permeability due to the relatively low diffusion rate. As shown in Figure 6.9, it was observed that,cell media permeated out through alginate wall would not accumulate inside the clearance to fill the entire clearance. Instead, most of them flowed from the two ends of the clearance due to the peristaltic perfusion pumping inside the conduit. The peristaltic perfusion pumping provided a pulsating flow inside conduits, which intermittently enlarged the elastic conduits, and thus expelled the media from the clearance. Very limited media was left inside the clearance that could be further diffused into bulk hydrogel.

Comparing Figure 6.7(c) and Figure 6.7(d), in diffusivity experiments, the fluorescent intensity did not stop changing over time in Figure 6.7(c), whereas in Figure 6.7(d) the fluorescent intensity stopped increasing after 3 minutes. This is because in Figure 6.7(c), as soon as the fluorescent media filled the vasculature system, the peristaltic pump was stopped. The cell media permeating out from conduit walls would not be expelled from the clearance and could be diffused into surrounding bulk hydrogel over time.

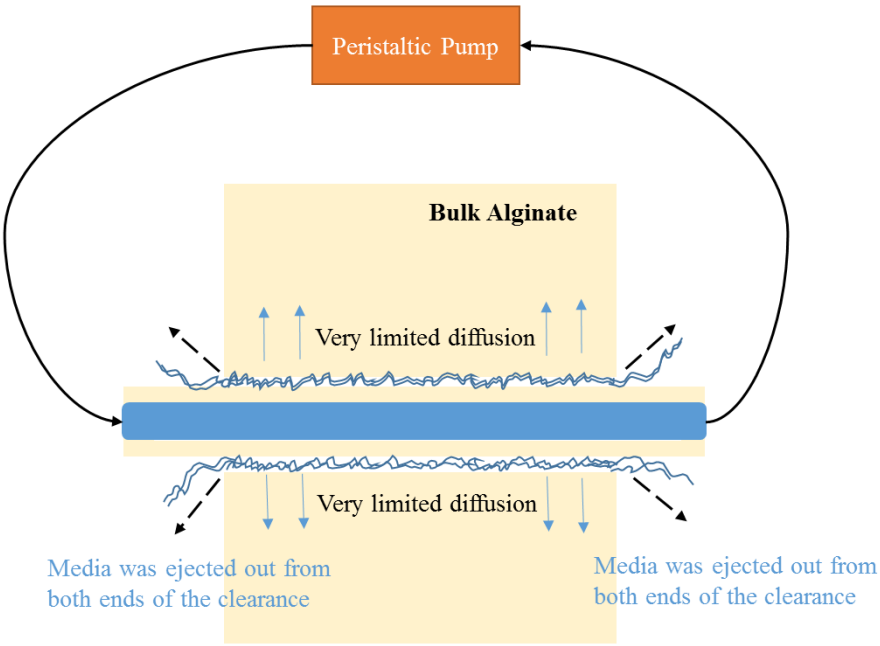

Figure 6.9

A representative figure of the perfusion experiment.

Due to the clearance between the bulk alginate and the vasculature system, the permeability characterization experiment failed; alginate conduits were used directly to perfuse fluorescent dye and characterize their permeability coefficients. The wall thickness of conduits was so thin that the fluorescent dye diffused into the alginate wall immediately and no diffusion process can be observed over time using the available experimental setting. It is also difficult to analytically derive a mathematical model to characterize the flow inside the conduit. The alginate conduit is an elastic conduit with flow-induced deformation. As mentioned previously, the diameter of the conduit was significantly influenced by the perfusion process. The length of the conduit was also changed in the perfusion process due to the weight. Also, during perfusion, the peristaltic pump provided a pulsating flow inside conduits, which made the math model more complex.

CHAPTER VII

DEHYDRATION, SWELLING, DEGRADATION, AND MECHANICAL PROPERTIES AND TISSUE HISTOLOGY TEST

In this chapter, dehydration, swelling, and degradation characteristics of conduits are investigated in detail. The shrinkage rate obtained in dehydration experiments shows the porosity of conduits. Highly porous constructs are strongly desired, as long as constructs can provide enough mechanical support for cells to grow and make their own matrix. Swelling and degradation experiments offered important information about the alginate degradation process. Alginate is a natural biopolymer and is biocompatible and biodegradable. During its degradation process, the mechanical properties of alginate constructs change over time. In order to prevent construct collapse and ensure a reasonable tissue regeneration rate, it is essential to design a tissue engineered construct with a similar biomaterial degradation and extracellular matrix generation rate. However, the degradation rate of natural polymer is not tunable. Knowledge of the construct degradation process and degradation rates is useful. In addition, mechanical properties are an important characteristic of natural vascular systems. Thus, the burst pressure of conduits is also presented and compared with natural vascular systems in this chapter.

7.1 Materials and Method

7.1.1 Materials

Prior to making a hydrogel solution, sodium alginate powder (Sigma Aldrich, United Kingdom) and calcium chloride powder (Sigma Aldrich, United Kingdom) were treated with UV light for sterilization three times for a 30-minute cycle each time. Ultraviolet-sterilized sodium alginate was dissolved in deionized water to make 3%, 4%, and 5% solutions. Solutions were mixed with a magnetic stirrer (HANNA Instruments, U.S.A.) until homogeneity was reached. Similarly, the crosslinking solution was prepared by dissolving UV-sterilized $CaCl_2$ in ultra-purified water (Invitrogen^{TM} Life Technologies, U.S.A.) at 4%, 5%, and 6% (w/v). With the

exception of those in Section 3.5, all alginate conduits used in this paper were fabricated with a 4% calcium chloride solution.

7.1.2 Cell Preparation

Human umbilical vein smooth muscle cells (HUVSMCs) (Invitrogen™ Life Technologies, U.S.A.) were grown in 75 cm^2 cell culture flasks in Dulbecco's modified eagle's medium Medium 231 (Invitrogen™ Life Technologies, U.S.A.), supplemented with 10% FBS, smooth muscle cell growth supplement (Invitrogen™ Life Technologies, U.S.A.), 10 µg/µl penicillin, 10 µg/ml streptomycin, and 2.5 µg/µl fungizone (Invitrogen™ Life Technologies, U.S.A.). Cells were incubated at 37° C in 98% humidity and 5% CO_2. Cell culture medium was changed every 2 days. When the cultures reached 70% confluence, the cells were detached from the flasks using a 0.25% trypsin-EDTA solution, washed twice, and resuspended in 4% sodium alginate solution and gently mixed with alginate solution by a vortex mixer to get uniform distribution. Cells were used at a density of 10×10^6 cells/ml.

7.1.3 Dehydration, Swelling, and Degradation Tests

In dehydration, swelling, and degradation experiments, conduits were soaked in 4% $CaCl_2$ for 30 minutes upon fabrication to ensure crosslinking. Thereafter, conduits were dehydrated at room temperature for 4 days. The dehydrated conduits were then soaked in PBS solution for swelling and degradation studies. The shrinkage rate by weight (SRW) and swelling ratio (SR) were calculated using the following equations:

$$SRW = (1 - \frac{W_d}{W_o}) \times 100\% \tag{21}$$

$$SR = \frac{W_i - W_d}{W_d} \times 100\% \tag{22}$$

where W_o is the original conduit weight right after fabrication, W_i is the instant conduit weight at the measurement moments, and W_d is the dehydrated conduit weight.

7.1.4 Dimensional Characterization of Conduits during Dehydration, Swelling, and Degradation

The conduit dimensions were measured using light microscopy (Motic®, BA310, U.S.A.). Only conduit diameters were measured after dehydration because conduit walls and the lumen side of dehydrated conduits were not distinguishable under the microscope. Conduit dimension measurements were conducted throughout the swelling and degradation tests. The four-hour point was selected as a measurement point because the swelling ratio of 5% conduits reached its maximum value at four hours. The 5% alginate conduits were used in this experiment because their swelling ratio curve started decreasing earliest.

The diameter shrinkage rate (*DSR*) is calculated as:

$$DSR = (1 - \frac{D_d}{D_o}) \times 100\% \tag{23}$$

where D_o is the original conduit diameter after fabrication, and D_d is the dehydrated conduit diameter.

7.1.5 Mechanical Testing

After fabrication, conduits were soaked in a $CaCl_2$ solution for 24 hours. Previous research shows crosslinking time has less influence on alginate elastic modulus after 24 hours

crosslinking [107]. Soaking them in a $CaCl_2$ solution minimized the effect of residence time on samples. A Biotense Perfusion Bioreactor (ADMET, Inc., U.S.A.) was used to evaluate tensile characteristics. Each sample was a maximum of 30 mm long and mounted on rectangular mini sandpaper in order to prevent slippage during the test. Upon applying the mechanical load, conduits were ruptured in the middle or near the edge. Displacement and load information data were recorded by a data acquisition system (MTestQuattro System, U.S.A.). The estimated burst pressure (*BP*) was calculated from ultimate tensile strength (*UTS*) measurements by rearranging the Laplace law for a pressurized thin-walled hollow cylinder [30], where *BP* is the estimated burst pressure (mmHg), *T* represents the wall thickness (μm) of conduits, and *LD* represents the unpressurized lumen diameter (μm) (see Equation 24).

$$BP = 2\frac{UTS \times T}{LD} \tag{24}$$

7.1.6 Tissue Histology

After fabrication, cellular conduits were cultured for a prolonged time period, followed by a histology examination. After six weeks of in vitro culturing in smooth muscle cell differentiation media, frozen conduits were fixed and sectioned at 5 μm for histological examination for markers specific to smooth muscle cells. Verhoeff–Van Giesen staining was used to visualize collagen deposition, where collagen stains a red color. All the procedures were carried out per the manufacturers' instructions. Sample slides were examined under an Olympus BX-61 Brightfield fluorescence microscope (Olympus America, U.S.A.) at different magnifications.

7.1.7 Statistical Analyses

In dimensional characterization experiments, more than 50 pieces of data were obtained by measuring several different conduits at different sections of these conduits. The results shown in those experiments were an average of all 50 pieces of data. The statistical analysis was carried out using Minitab 17. The statistically significant difference was determined using the two-tailed student's t-test. Groups with a significance level of $p<0.05$ were considered significant. Standard error bars in all figures represent standard deviations. In Section 7.2.1 and Sections 7.2.2, for the sample size $n=3$, the data points shown in the figures were averages of the three.

7.2 Results

7.2.1 Fabrication of Conduits

The 5% alginate conduits were dehydrated and shown in Figure 7.1(a). After dehydration, the majority of the 5% conduits remained in conduit shape (see Figures 7.1(b) and (c)). After dehydration, the conduit diameter shrank to 788 μm, which was 54.4% of the original conduit diameter. Figure 7.1(d) is the SRW of conduits made of different alginate concentrations. During the dehydration process, 3% alginate conduits lost more weight than others. The weight shrinkage rate decreased as alginate concentration increased. The *SRW* of the 3%, 4%, and 5% vasculatures were 95.8%, 94.2%, and 90.4%, respectively. Statistical significance was observed between groups.

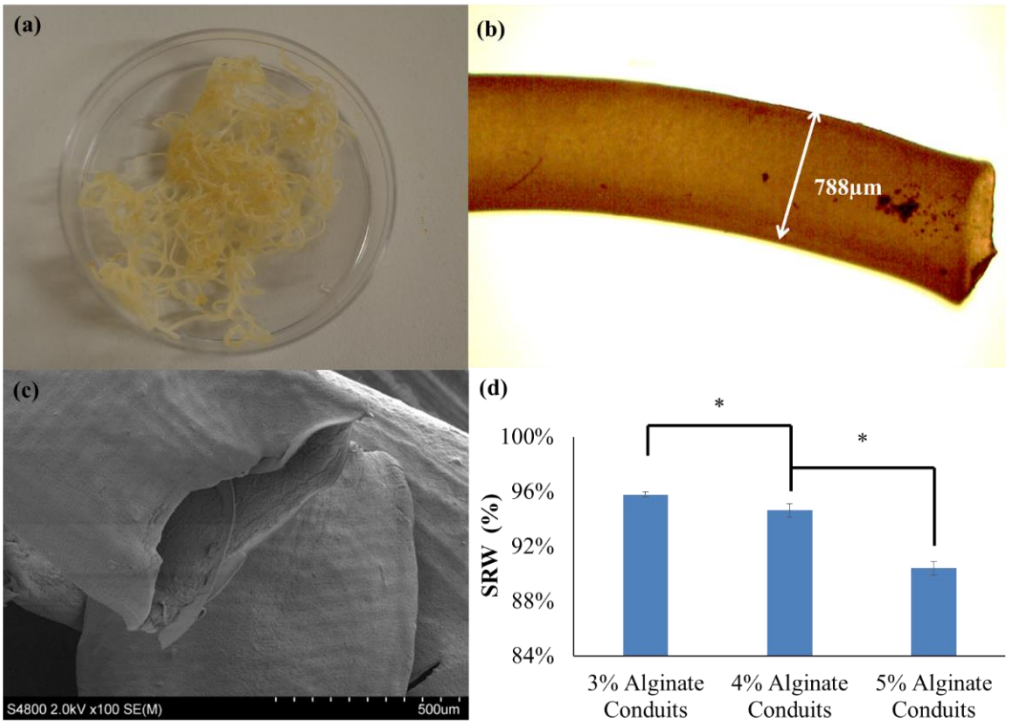

Figure 7.1

5% conduits in dehydration test: (a) dehydrated samples, (b) dehydrated samples under microscope still demonstrating conduit shape, (c) an SEM image of dehydrated conduit, and (d) SRW of different alginate concentrations (the single asterisk * indicates significant difference between groups $p<0.05$).

7.2.2 Dehydration, Swelling, and Degradation Tests

Swelling tests were performed following the dehydration tests. Figure 7.2(a)-(c) shows the swelling ratio curve over time for 3%, 4%, and 5% alginate conduit groups. For conduits made of different alginate concentrations, the swelling ratio curves depict obviously different trends. The initial slope of the swelling ratio curve of the 3% conduits was large, which indicates a high swelling rate. Figure 7.2(d) summarizes the time to reach the maximum swelling ratio (T_{ms}). T_{ms} decreased as alginate concentration

increased. Figure 7.2(e) shows the maximum swelling ratio. The maximum swelling ratio also decreased as alginate concentration increased, and the 3% group had the largest swelling capacity among all groups. Figure 7.2(f) compared the liquid reabsorption capacities (W_{max}/W_o) of the three groups, where W_{max} is the conduits' maximum swelling weight achievable. For conduits made of different alginate concentrations, W_{max}/W_o remained similar, around 33%. This number indicated that dehydrated conduits from all groups "reabsorbed" liquid up to 33% of the original weight, despite their significantly different maximum swelling ratios. The W_{max}/W_o value for the 3%, 4%, and 5% alginate vasculatures were 32.2%, 33.3%, and 33.4%, respectively. Compared to other groups, the 3% alginate vasculature had a smaller W_{max}/W_o value. This was because the value of T_{ms} of the 3% group was much greater (see Figure 6.2(d)) than that of the other groups; it was 42 hours longer than the 4% group and 44 hours longer than the 5% group because it took the 3% alginate group the longest time to reach the maximum swelling weight. So the measurement of W_{max} value of the 3% alginate group was made much later than that of the other groups. The 3% alginate group underwent a relatively rapid degradation process in degradation experiments. The degradation process removed a considerable portion of alginate from the system during these 40 more hours and thus lowered the calculated W_{max}/W_o value.

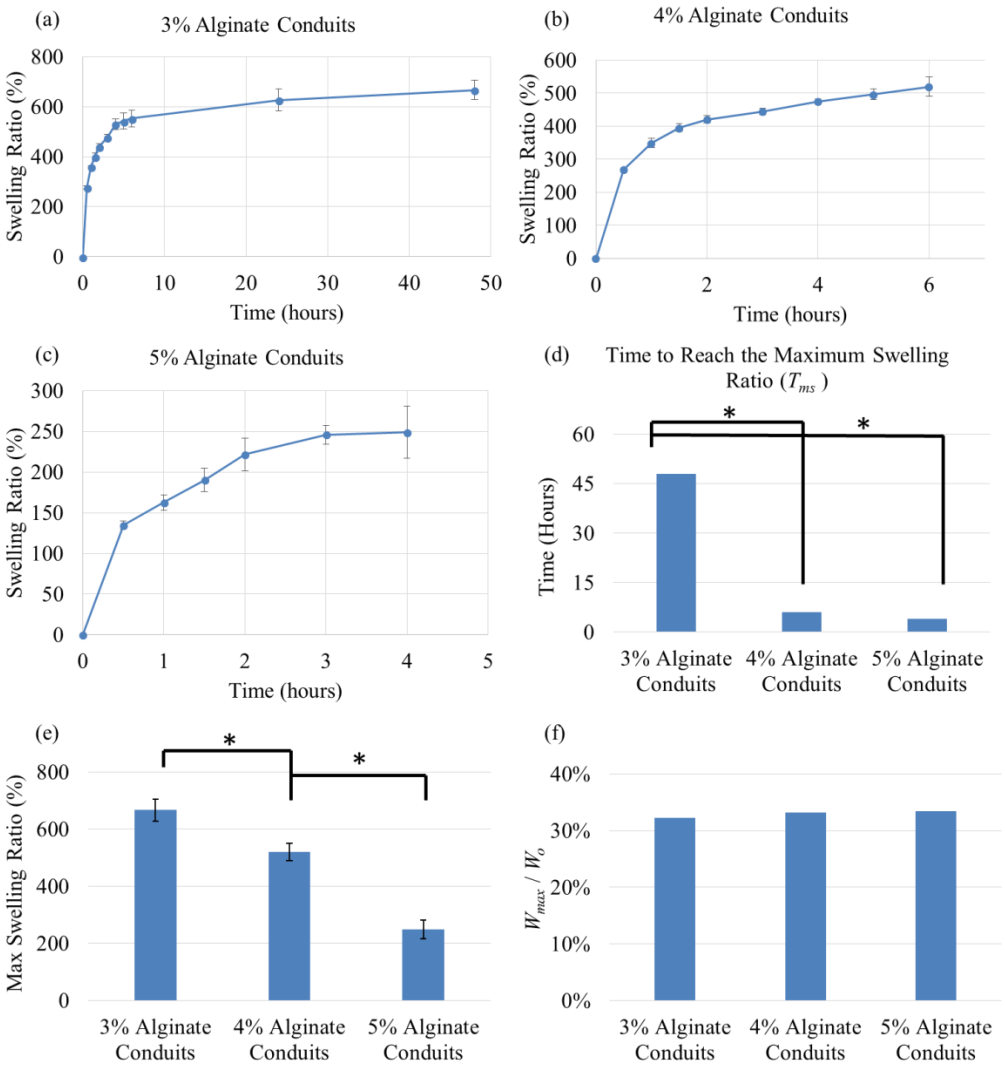

Figure 7.2

Swelling test results of conduits with different alginate concentrations. Swelling ratio curve for (a) 3% alginate conduit, (b) 4% alginate conduit, and (c) 5% alginate conduit, (d) time to reach the maximum swelling ratio (T_{ms}), (e) maximum swelling ratio, and (f) liquid reabsorption capability (W_{maxi}/W_o) (the single asterisk (*) indicates significant difference between groups $p<0.05$).

Figure 7.3 shows the swelling ratio curve of the 3%, 4%, and 5% alginate conduits in degradation tests. The swelling ratio of the 5% alginate group started decreasing earliest, but its degradation process progressed relatively slowly. On the contrary, the swelling ratio of conduits made of the 3% alginate group started decreasing latest but progressed with a fast degradation process. Figure 7.4(a) and (b) show the SEM image of a dehydrated conduit's luminal and outer wall surfaces. The surface of the dehydrated conduit was rough. Figure 7.4(c)-(f) demonstrate the influence of the swelling and degradation processes on conduits' outer surfaces. The 3% alginate conduits were used in this experiment because their degradation progressed relatively quickly, making their degradation phenomena more obvious in shorter time. Figure 7.4(c) was taken directly after fabrication. Under light microscopy, the conduit had a smooth surface with "fish-scale-like" features caused by the bioprinting process. The "fish-scales" on the conduit's surface were perpendicular to the conduit walls. Thereafter, conduits underwent a four-day dehydration process and were soaked in PBS for swelling and degradation tests. Figure 7.4(d) shows the microscopy image of conduits after one day of soaking in PBS. The folds observed on the surface of the samples were caused by shrinkage during the dehydration process. Unlike the "fish-scales," most folds were parallel to the conduit's walls. In Figure 7.4(e), 3% alginate conduits had been soaked in PBS for seven days. Compared with Figure 7.4(d), the folds on the conduit surface became smoother. The small pits observed on the surface were formed due to the degradation process. Further, after 10 days of swelling and degradation, more pits of larger diameter were observed on the conduit surface (see Figure 7.4(f)), while the folds completely disappeared. The disappearance of the folds was good evidence for the existence of swelling, even after conduits soaked in PBS for seven days.

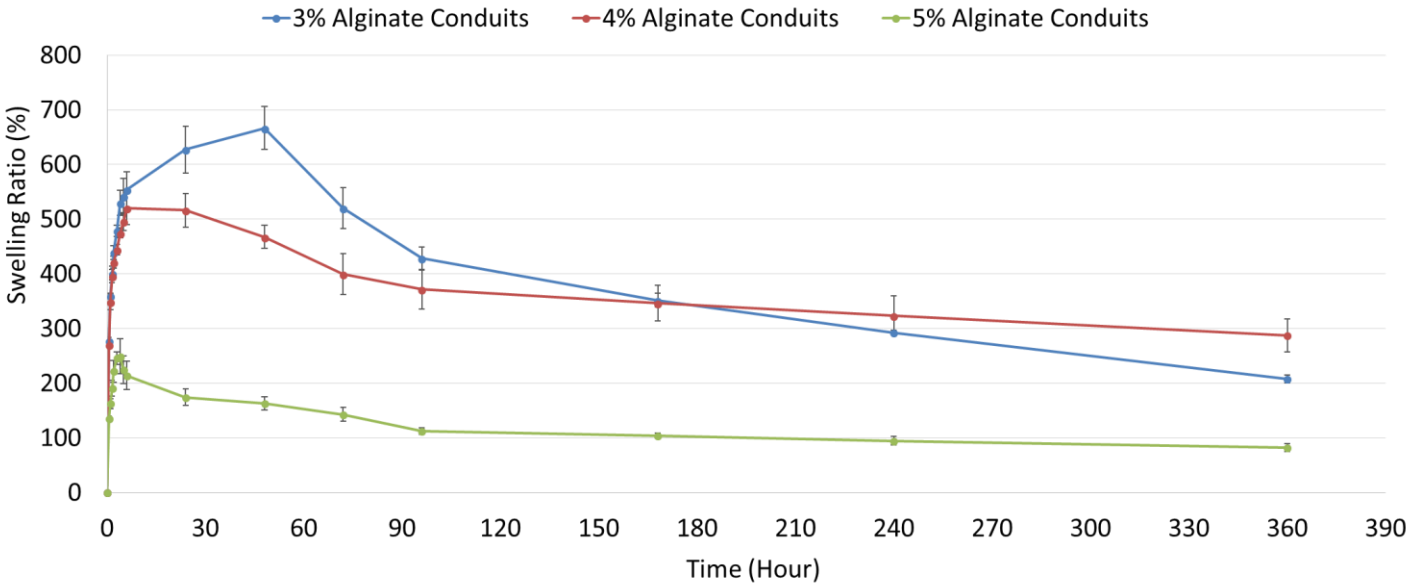

Figure 7. 3
Swelling ratio curve over time.

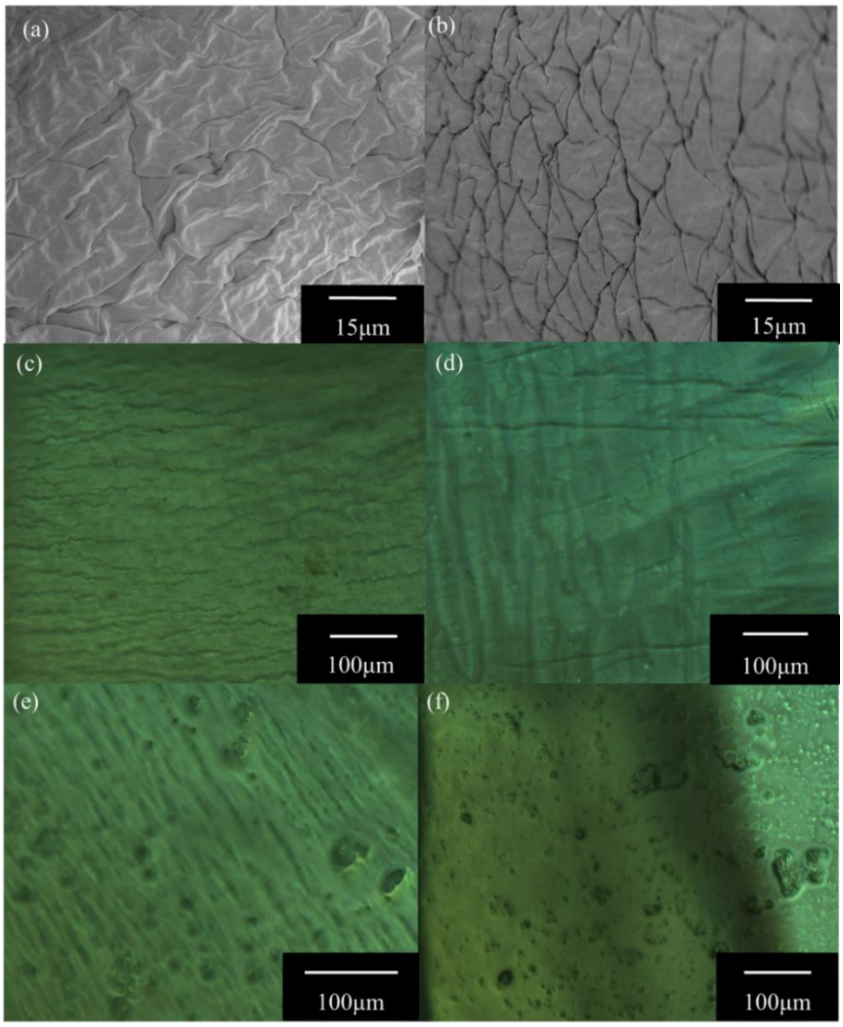

Figure 7.4

Degradation process of vasculature: (a-b) SEM images of dehydrated conduit's luminal and outer surfaces, (c) light microscopy image of 3% alginate vasculature directly after fabrication, (d) at day 1, (e) day 7, (f) and day 10.

7.2.3 Dimensional Characterization

As shown in Figure 7.5(a), alginate concentration had a significant influence on conduit dimensions. Conduits made of 4% alginate had the smallest conduit and lumen diameter. Results

from our previous work support this as well [103]. The conduit diameter after dehydration is shown in Figure 7.5(b). Dehydrated 3% alginate conduits had the smallest diameter, and the diameter of the dehydrated conduits increased as the alginate concentration increased. Figure 7.5(c) shows the *DSR* of conduits made of different alginate concentrations, which was obtained using Equation (23). The *DSR* represents only the shrinkage in the uniaxial direction. If we assume that the ionically crosslinked alginate structure was homogeneous, the shrinkage process should possess isotropic homogeneity, which means that shrinkage rates along all dimensions are the same. Three-dimensional shrinkage rates for the 3%, 4%, and 5% conduits were 96.9%, 93.62%, and 83.9%, respectively. The 3% alginate group had the largest dehydration shrinkage rate and lost more weight and volume than the other groups. Both the *DSR* and *SRW* decreased as the alginate concentration increased. Values of dimensional shrinkage rates and weight shrinkage rates were similar and consistent. Figure 7.5(d) shows dimensional changes of 5% alginate conduit throughout the dehydration, swelling, and degradation experiments. After 4 hours of soaking in PBS, although conduits reached their maximum swelling ratio, the diameter of the swollen conduits was much smaller than the originally fabricated ones. Their diameters were only 64.4% of the originally fabricated ones.

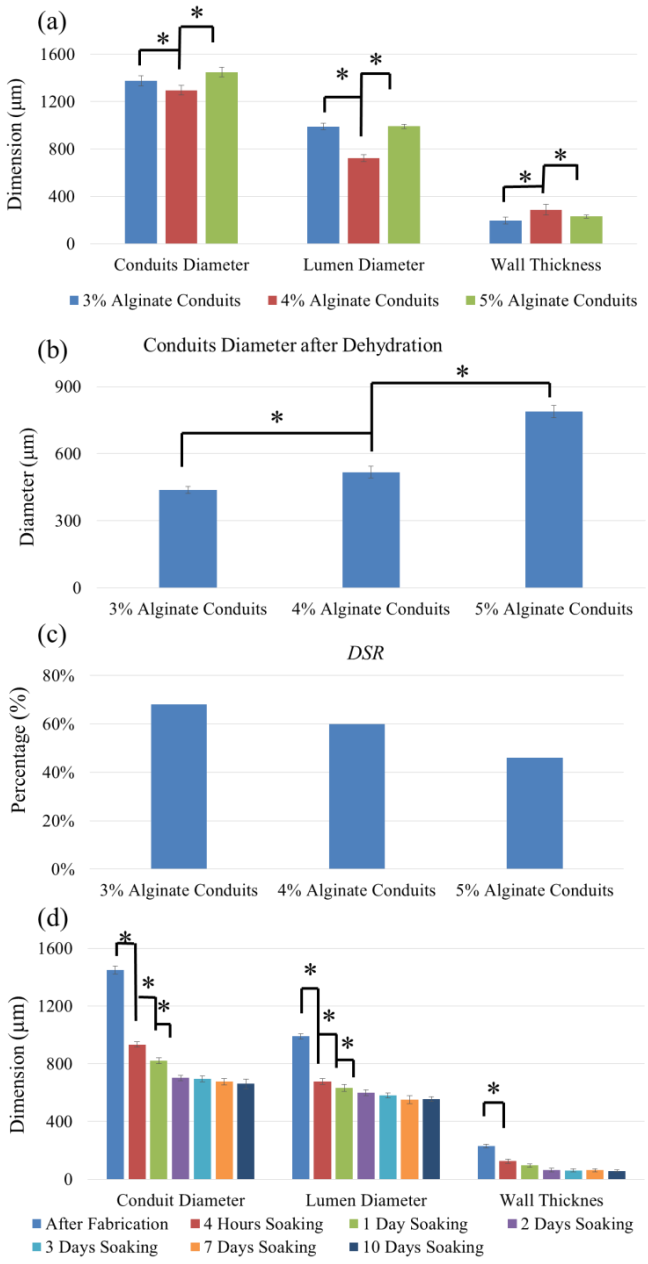

Figure 7.5

Dimensional characterization of the dehydration process: (a) dimension differences of conduits made of different alginate concentrations, (b) conduit diameter after dehydration, (c) diameter shrinkage rate (*DSR*) of conduits made of different alginate concentrations, and (d) conduits' dimensional changes over time (the single asterisk (*) indicates significant difference between groups $p<0.05$).

7.2.4 Mechanical Testing

The mechanical tests were performed to explore the mechanical properties of conduits. Table 7.1 demonstrates the tensile strength, elastic modulus, ultimate strain, and calculated burst pressure of conduits with different alginate concentrations. It illustrates that the tensile strength of the 4% conduits (110±5.8 kPa) was higher than that of the 3% group (382±19 kPa). A higher concentration of alginate resulted in a higher Young's modulus, from 105±7.5 kPa for 3% conduits to 341±23 kPa for 4% alginate conduits. The ultimate strain for the 3% alginate conduits is higher than the 4% alginate conduits, and the evaluated burst pressure increased as alginate concentration increased. The ultimate strain and evaluated burst pressure for 3% conduits were 0.82 ±0.18 and 43.24 mmHg, and for 4% conduits were 0.69 ±0.13 and 303.73 mmHg, respectively. In a summary, the mechanical properties of the 3% conduits were significantly lower than those of the 4% group. A higher concentration of alginate resulted in significantly higher tensile strength, Young's modulus, and burst pressure, along with lower ultimate strain.

The difference between the 3% and 4% groups' estimated burst pressure is much more than that of tensile strength and Young's modulus. This is because burst pressure was estimated from the mechanical testing measurements, and under the same fabrication parameters, the 3% group had greater lumen diameter as well as thinner conduit wall. Although 4% alginate conduits have much higher burst pressure compared with the 3% group, when it is compared with natural blood vessel, in which burst pressure is around 3561 mmHg [112], it is evident that further improvement is needed in future experiments to overcome the inherent weak mechanical properties of natural polymers.

Table 7.1 Mechanical properties of conduits.

Mechanical Tests	*3% Alginate conduits*	*4% Alginate conduits*
Tensile Strength (kPa)	110±5.8	382±19
Young's Modulus (kPa)	105±7.5	341±23
Ultimate Strain	0.82 ± 0.18	0.69 ± 0.13
Burst Pressure (mmHg)	43.24	303.73

7.2.5 Tissue Histology Study

A histology study was performed to evaluate long-term cultured conduits for cell morphology and tissue-specific ECM formation. Printed conduits maintained their structural integrity with a well-defined lumen and conduit wall and ECM deposition in the inner and outer boundaries after six weeks in vitro culture (Figure 7.6(a)). Verhoeff-Van Gieson staining shows collagen deposition around cells and throughout the conduit wall (Figure 7.6(a)-(b), light pink color). Interestingly, thick cell sheets were formed on the peripheral and luminal surfaces with multiple layers of cells (Figures 7.6(c)-(d), dashed boxes), with smooth muscle deposition stained a purple-pink color. Cell sheets were closely attached on the conduit walls. It is possible that cells migrated from their original lacunae towards the gradient of culture media to both the lumen side and the peripheral side, where there were greater oxygen and nutrient supplies. Upon migrating towards oxygen and growth factor gradients, cells started to grow and synthesized smooth muscle, forming an ECM lining. This may suggest that continuous perfusion of culture media through the lumen might facilitate further cell migration and proliferation toward the lumen side in long-term-cultured conduits, potentially increasing smooth muscle formation. The detached cell sheets (Figure 7.6(b)) resulted from the frozen sectioning of some samples during histology sectioning. Encapsulated cells resided in their lacunae and were largely intact, with a rounded stained nucleus and lighter stained cytoplasm (Figure 7.6(d)).

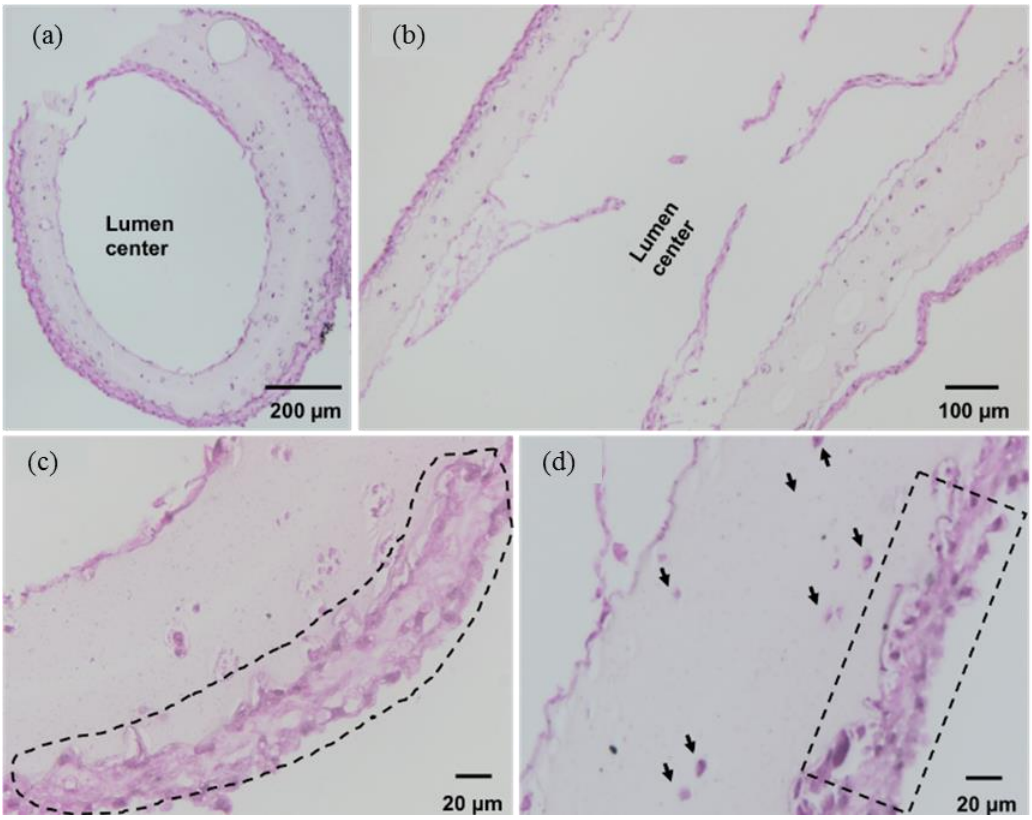

Figure 7.6

Histology test for six-week-cultured conduits: (a) reasonable collagen deposition can be observed on long-term-cultured vasculatures, (b) delamination of cell sheets observed in some samples during histology sectioning process, and (c-d) thick cell sheets were formed on the conduit walls, where arrowheads show intact cells encapsulated in alginate network.

7.3 Discussion and Conclusion

In this chapter, conduits were printed using a new 3D bioprinting system; the conduits can be later integrated into thick tissue fabrication or organ printing. We thoroughly investigated the dehydration, swelling, and degradation process of conduits made of different alginate

concentrations. In the dehydration test, the 3% group had both the largest dimensional and weight shrinkage rate, which indicated it had the largest porosity (porosity is a measurement of void). The greater the porosity, the better, as long as the construct can provide enough mechanical support for attached cells. More porosity means there are more voids and space for cells to grow, proliferate, and make their own extra-cellular matrix. Also, construct with more porosity have a better media exchange rate since there is more space for liquid and gas to penetrate and exchange. In swelling tests, the 3% group had the highest maximum swelling ratio. It took the 3% group the longest time to reach the maximum swelling ratio, and the degradation process of the 3% group was the fastest among all groups. In contrast, the 5% group reached the maximum swelling ratio quickest but underwent a relatively slow degradation process. A rational explanation for this phenomenon is that, compared with the 5% group, the 3% group had more pores (larger shrinkage rate and higher porosity). As a result, the swelling rate of the 3% group was the highest. When conduits were soaked in PBS, the swelling process and degradation process were carried out at the same time. At the early stages of the swelling and degradation experiments, conduits underwent a fast swelling process, which could be supported by the large slope in the swelling ratio curve during the first several hours. Their swelling rate was much greater than the degradation rate. The maximum swelling ratio point is actually not the start time of degradation. It is the time point at which the degradation rate starts to be larger than the swelling rate. After that, the degradation process dominated the change in the structure weight. The swelling rate was fastest at the beginning of the swelling process and then slowed down. The 3% group had a higher swelling rate, and it took more time for the degradation rate to catch up with the swelling rate. At the same time, due to larger-polymer pores, the 3% group was also easier for water to penetrate, so it underwent a faster degradation process. In contrast, the 5% group had fewer pores (smaller shrinkage rate and lower porosity), so it underwent a slower swelling process. The degradation rate quickly became close to the swelling rate.

In dimensional characterization experiments, lumen diameter, conduit diameter, and wall thickness all changed over time during the swelling and degradation process, which was

evidence of the existence of the swelling and degradation processes at the same time. The decrease in conduit diameter could be explained by the presence of the degradation process. The decrease in lumen diameter, on the other hand, was due to the swelling process. On the outer wall of the vasculature, the degradation process dominated the dimensional change. On the inner wall of the conduits, limited liquid could penetrate through pores and get into the lumen section. The degradation rate was slower than the swelling rate, so the swelling process dominated the dimensional change. In terms of wall thickness, changes were an ideal indicator of the relative changes of degradation rate versus swelling rate on the entire structure. The changes of swelling and degradation rates could be observed in the changes of lumen and conduit diameters. When dehydrated 5% alginate conduits soaked in PBS, limited liquid could penetrate the alginate wall and reach the lumen section due to the relatively tight polymer structures of 5% alginate. The degradation rate at the inner wall of the 5% conduit was very low. Thus, the lumen diameter changes could be assumed to be mainly due to the swelling rate. On the other hand, on the outer wall of the vasculature, the swelling and degradation processes occurred at the same time. The decrease in conduit diameters indicates that the degradation rate was larger than the swelling rate on the outer wall of the vasculature, and thus it dominated the dimensional changes. The conduits' dimensional changes were significant during the first several days and became insignificant later on. This illustrates that both the swelling process and the degradation process slowed down over time. The slowdown of the swelling process occurred because the conduit reached the maximum swelling ratio, whereas the degradation process slowed down for a much more complex reason. The degradation of alginate hydrogel was due to loss of Ca^{2+} ions. During the swelling and degradation experiments, PBS was not replenished. Over time, the Ca^{2+} ions in alginate and the PBS reached an equilibrium state, and thus the degradation process slowed down.

Mechanical tests were performed to explore the mechanical properties of conduits. Burst pressure was estimated from the mechanical testing measurements. When it is compared with the natural vascular system, where burst pressure is around 3561 mmHg [112], it is evident that

further improvement is needed in future experiments to overcome the inherent weak mechanical properties of natural polymers. One thing need to mention here is during culturing, those cells encapsulated in alginate conduit walls would make their own ECM and then further greatly increase the mechanical property of engineered construct [113]. Although the mechanical property of printed conduits is weak compared with the natural vascular system and are not suitable to directly implant in animals or the human body, this mechanical property is enough for media perfusion in thick tissue fabrication.

A histology study was also performed on long-term-cultured cellular conduits. Cells were able to grow and maintain their intact morphology as well as make ECM within the conduit wall and form a lining of ECM sheet along the lumen section. It is possible that cells migrated from their original lacunae towards the gradient of culture media to both the lumen side and the peripheral side, where there were greater oxygen and nutrient supplies. Upon migrating towards oxygen and growth factor gradients, cells started to grow and synthesized ECM, which diffused along both sides of the conduits, forming an ECM lining. This may suggest that continuous pumping of culture media (dynamic culture) through the lumen might facilitate further cell migration and proliferation toward the lumen side in long-term-cultured conduits, potentially increasing ECM formation. In addition, because significant cell migrations were observed during long term culture in histology test, and because previous research [113] showed endothelia cells would sort automatically to the lumen of vascular conduit upon dynamic culture, it is possible to fabricate multi-cells type vascular conduit. Endothelia cell and smooth muscle cells could be mixed in a ratio and encapsulated into alginate vasculature conduit. The multicellular vascular conduit would be dynamically cultured with continuous perfusion. Then, over time the endothelia cell might migrate to lumen section and form a continuous endothelia (intima), and we might be able to obtain a conduit having multi-cells type and well-organized cell layers. On the other hand, although reasonable collagen deposition and ECM formed around cells and throughout the conduit wall, compare with other work [114,115], the improvement is not significant. The limited ECM generation might due to the high concentration of alginate. In

lots of researches, alginate solution with 2% or even lower concentration was used to fabricate tissue engineered construct [116-120]. In this work, 4% alginate solution was selected due to the consideration of mechanical property and structure integrity. Figures 7.4 shown the degradation rate of alginate conduit increased as alginate concentration increased. Thus, one possible reason for the limited ECM generation might due to the low degradation rate of 4% alginate hydrogels. Because the alginate biopolymer was degraded to slow, there is no enough space for cells to grow, proliferate and make their ECM, and thus, limited ECM generation rate was observed. Also, because the degradation process happened mainly on the outer surface and inner surface of conduit, most of the ECM deposition was observed on the surface of conduits.

Tissue engineering is a challenging and complex research area. Many criteria need to be taken into consideration during the construct design phase. In general, conduits fabricated by a higher alginate concentration had lower cell viability, slower degradation process, smaller construct porosity, and lower permeability capacity, as well as higher mechanical properties. It is difficult to define an optimization function to determine an optimal result. Selection priority should depend on cell type, application environments, and the most important concerns.

CHAPTER VIII
SUMMARY, CONCLUSIONS AND FUTURE WORK RECOMMENDATIONS

8.1 Summary of Research

This thesis introduced a new 3D-bioprinting technique that can be integrated into thick tissue fabrication or organ printing processes in the near future. The presented system offered several advantages, including that it is perfusable, doesn't need any post-fabrication procedures, and enables direct bioprinting of complex media exchange networks. The fabrication system setup and fabrication process were explained in detail in Chapter 2, and several printed samples were demonstrated. Conduits printed by the proposed system have smooth, uniform, and well-defined walls and can be used to fabricate a branched vasculature system.

This thesis included both theoretical and experimental characterizations of the proposed system and the printed conduits. The theoretical sections included Chapters 3, 4, and 5. In Chapter 3, the dispensing rheology was mathematically modeled. A prediction model for conduit deposition was derived in order to accurately print conduits, and two printed samples were shown. The proposed system can print a vasculature system in any complex pattern. Because shear stress is the main cause of cell death during the fabrication process, in order to understand the cell behavior during the dispensing process, the shear stress distribution inside the coaxial nozzle was analyzed, and the theoretical cell viability distribution on conduit cross section was also explored. Chapter 4 studied the layer-by-layer fabrication strategy for bioprinting. Strong bonds between layers can be obtained by following the strategy discussed in this chapter. Dimensional characterization for conduit was performed in Chapter 5. Five possible influential factors, biomaterial concentration, crosslinker concentration, biomaterial dispensing pressure, crosslinker dispensing rate, and nozzle dimensional factor, and their

effects were explored in this chapter. Two empirical math models, prediction models for the conduit diameter and conduit wall thickness, were obtained for conduit dimension prediction. It is desirable to predict dimensions of printed conduits before fabrication and fabricate conduits with gradually changing dimensions in order to better mimic nature. In addition, influences of fabrication parameters on cell viability were explored in Chapter 5.

Chapter 6 and 7 discussed the experimental characterization of printed conduit, including the conduit perfusion and diffusion properties, mechanical properties, dehydration, swelling, and degradation properties, and long-term-cultured histology test. Designing a tissue engineering product is complex and challenging. The most important criteria for fabricating an artificial blood vessel are shown in Table 8.1. Thus, several tests were presented in this thesis to experimentally characterize printed conduits. We thoroughly investigated the perfusablity and permeability capabilities of conduits in Chapter 6. In addition, experimental characterization was performed for the dehydration, swelling, and degradation properties of conduits along with their mechanical properties in Chapter 7 because these properties are crucial for long-term function in perfusing and delivering media. Histology tests were also conducted to evaluate smooth muscle formation over a six-week culture period.

Table 8. 1

Important criteria to judge an artificial blood vessel

Success Criteria	*Measurement Method*
Good structure integrity, uniform, smooth and well-defined walls	Microscopy Images (Chapter 2)
Good biocompatibility and high cell viability	Cell Viability Test
Enough mechanical properties to support attached cell to grow	Mechanical Test (Chapter 7)
Perfusion and diffusion capabilities	Perfusion Test (Chapter 6)
Enough porosity for cell to grow, proliferate, and generate extra-cellular matrix (ECM)	Dehydration Test (Chapter 7)
Matched biodegradation rate and ECM generation rate (No structure failure in long term e.g. structure collapse or deteriorate structural integrity	Swelling & Degradation Test (Chapter 7) Long-Term Culture Experiment (Chapter 7)
Reasonable ECM deposition	Tissue Histology Test (Chapter 7)
Can be integrated into thick tissue/organ fabrication	
Biomimics the structure of natural blood vessel and can be implanted in vivo	Suture pressure test, burst pressure test (Chapter 7)
Long-term implant patency, without thrombogenic generation	

8.2 Future Work Recommendations

Alginate is a biomaterial derived from brown algae. Despite its good biocompatibility, alginate is composed of inert monomers that inherently lack the bioactive ligands necessary for cell anchoring [69] and cannot promote human cells to grow, proliferate, and make their extracellular matrix. For future work, biological conduits with more native biomaterials, such as collagen or fibrins, should be developed.

Also, conduits made until now include only one type of cells, but the natural vascular systems have multiple layers of structures, including endothelium, a smooth muscle cell layer, and several layers of elastic lamina. Thus, for future work, multi-cellular conduits need to be fabricated to further biomimic nature.

In addition, mechanical properties of fabricated conduits are weak due to the inherent weak property of natural polymers. We used carbon nanotube reinforcement to improve the mechanical property of alginate conduits, since previous studies have shown that carbon nanotube reinforcement was capable of increasing the mechanical strength of materials significantly [121-123]. Several experiments have been conducted to apply carbon nanotubes in tissue engineering [124, 125]. Although carbon nanotube reinforcement increased the mechanical properties of conduits to some extent, compared with natural vascular systems, the improvement is very limited. Carbon nanotube reinforcement did not influence the short-term cell viability of alginate conduits, but long-term culturing showed that carbon nanotube was toxic to cells [126, 127]. Thus, other nanofabrication technologies are needed to reinforce conduits to overcome the weak mechanical properties of natural biopolymer.

In addition, the proposed system can be integrated in thick tissue fabrication easily. In this regard, a Multi-Arm Bioprinter was developed in our laboratory [128] to integrate the bioprintable vasculature network with the rest of the tissue. For future work, cell aggregates and conduits could be printed at the same time for thick tissuefabrication.

REFERNCES

1. R. Lanza, R. Langer, and J. Vacanti, Principles of Tissue Engineering. 3rd edn ed. 2007: New York: Elsevier.

2. F.P.W. Melchels *et al.*, Additive manufacturing of tissues and organs. *Progress in Polymer Science*, 2012. **37**(8): p. 1079-1104.

3. W.L. Mondy *et al.*, Computer-aided design of microvasculature systems for use in vascular scaffold production. *Biofabrication*, 2009. **1**(3).

4. C. Norotte *et al.*, Scaffold-free vascular tissue engineering using bioprinting. *Biomaterials*, 2009. **30**(30): p. 5910-5917.

5. U.S. Department of Health and Human Service. Donate the gift of life. Available from: www.organdonor.gove/index.html (Accessed August 9, 2013).

6. U.S. Department of Health & Human Services. HRSA/OPTN organ procurement and Transplantation Network. Available from: optn.transplant. hrsa.gov/data/.

7. L. Ma *et al.*, Collagen/chitosan porous scaffolds with improved biostability for skin tissue engineering. *Biomaterials*, 2003. **24**(26): p. 4833-4841.

8. L. Mei et al., Preparation, characterization and evaluation of chitosan macroporous for potential application in skin tissue engineering. *International Journal of Biological Macromolecules*, 2012. **51**(5): p. 992-997.

9. S. Böttcher-Haberzeth, T. Biedermann, and E. Reichmann, Tissue engineering of skin. *Burns*, 2010. **36**(4): p. 450-460.

10. C. Paquet *et al.*, Tissue engineering of skin and cornea. *Annals of the New York Academy of Sciences*, 2010. **1197**(1): p. 166-177.

11. C.E. Schmidt and J.M. Baier, Acellular vascular tissues: natural biomaterials for tissue repair and tissue engineering. *Biomaterials*, 2000. **21**(22): p. 2215-2231.

12. T. Aper *et al*., Autologous blood vessels engineered from peripheral blood sample. *European Journal of Vascular and Endovascular Surgery*, 2007. **33**(1): p. 33-39.

13. A. Skardal, J. Zhang, and G.D. Prestwich, Bioprinting vessel-like constructs using hyaluronan hydrogels crosslinked with tetrahedral polyethylene glycol tetracrylates. *Biomaterials*, 2010. **31**(24): p. 6173-6181.

14. S. L. M. Dahl *et al.*, Decellularized native and engineered arterial scaffolds for transplantation. *Cell Transplantation*, 2003. **12**(6): p. 659-666.

15. F. Ozawa *et al*., Electrodeposition of alginate gels for construction of vascular-like structures. *Journal of Bioscience and Bioengineering*, 2013. **115**(4): p. 459-461.

16. L. Zhao *et al*., The integration of 3-D cell printing and mesoscopic fluorescence molecular tomography of vascular constructs within thick hydrogel scaffolds. *Biomaterials*, 2012. **33**(21): p. 5325-5332.

17. Y. Zheng *et al*., Microstructured templates for directed growth and vascularization of soft tissue in vivo. *Biomaterials*. 2011. **32**(23): p. 5391-5401.

18. W. He *et al*., Pericyte-based human tissue engineered vascular grafts. *Biomaterials*, 2010. **31**(32): p. 8235-8244.

19. S.P. Hoerstrup *et al.*, Tissue engineering of small caliber vascular grafts. *European Journal Cardio-Thoracic Surgery*, 2001. **20**(1): p. 164-169.

20. L. Cai *et al*., Vascular and micro-environmental influences on MSC-coral hydroxyapatite construct-based bone tissue engineering. *Biomaterials*, 2011. **32**(33): p. 8497-8505.

21. Y. Naito *et al*., Vascular tissue engineering: Towards the next generation vascular grafts. *Advanced Drug Delivery Reviews*, 2011. **63**(4–5): p. 312-323.

22. J.M. Holzwarth and P.X. Ma, Biomimetic nanofibrous scaffolds for bone tissue engineering. *Biomaterials*, 2011. **32**(36): p. 9622-9629.

23. T.E. Perry *et al*., Bone marrow as a cell source for tissue engineering heart valves. *The Annals of Thoracic Surgery*, 2003. **75**(3): p. 761-767.

24. H. Tian *et al*., Myogenic differentiation of human bone marrow mesenchymal stem cells on a 3D nano fibrous scaffold for bladder tissue engineering. *Biomaterials*, 2010. **31**(5): p. 870-877.

25. T. Chen *et al*., Engineering superficial zone features in tissue engineered cartilage. *Biotechnology and Bioengineering*, 2013. **110**(5): p. 1476-1486.

26. J. Sanchez-Adams and K.A. Athanasiou, Dermis isolated adult stem cells for cartilage tissue engineering. *Biomaterials*, 2012. **33**(1): p. 109-119.

27. L. Stanasel, M. Mirzazadeh, and J. J. Smith Iii, Bladder tissue engineering. *Urologic Clinics of North America*, 2010. **37**(4): p. 593-599.

28. N.F. Davis *et al*., Construction and evaluation of urinary bladder bioreactor for urologic tissue-engineering purposes. *Urology*, 2011. **78**(4): p. 954-960.

29. A. Atala, Tissue engineering of human bladder. *British Medical Bulletin*, 2011. **97**(1): p. 81-104.

30. A.A. Chen *et al*., Humanized mice with ectopic artificial liver tissues. *Proceedings of the National Academy of Sciences*, 2011. **108**(29): p. 11842-11847.

31. J. S. Lee and S-W Cho, Liver tissue engineering: Recent advances in the development of a bio-artificial liver. *Biotechnology and Bioprocess Engineering*, 2012. **17**(3): p. 427-438.

32. R. Baudoin *et al.*, Parallelized microfluidic biochips in multi well plate applied to liver tissue engineering. *Sensors and Actuators B: Chemical*, 2012. **173**: p. 919-926.

33. Shinoka, T. *et al.*, Tissue engineering heart valves: Valve leaflet replacement study in a lamb model. *The Annals of Thoracic Surgery*, 1995. **60(**3): p. S513-S516.

34. A. Bader *et al.*, Tissue engineering of heart valves – human endothelial cell seeding of detergent acellularized porcine valves. *European Journal of Cardio-Thoracic Surgery*, 1998. **14**(3): p. 279-284.

35. R. Gaetani *et al*., Cardiac tissue engineering using tissue printing technology and human cardiac progenitor cells. *Biomaterials*, 2012. **33**(6): p. 1782-1790.

36. D.D.R. Sebinger *et al*., ECM modulated early kidney development in embryonic organ culture. *Biomaterials*. **34**(28): p. 6670-82

37. D.A. Cieslinski and H. David Humes, Tissue engineering of a bioartificial kidney. *Biotechnology and Bioengineering*, 1994. **43**(7): p. 678-681.

38. K.C. Dee, D.A. Pulelo, and R. Bizios, An introduction to tissue biomaterial interactions. 2002: Hoboken, NJ: Wiley-Liss, Publications.

39. E. Carletti, A. Motta, and C. Migliaresi, Scaffolds for tissue engineering and 3D cell culture. *Methods in Molecular Biology*, 2011. **695**: p. 17-39.

40. J.L. Drury and D.J. Mooney, Hydrogels for tissue engineering: scaffold design variables and applications. *Biomaterials*, 2003. **24**(24): p. 4337-4351.

41. F. Intranuovol *et al*., Plasma modification of PCL porous scaffolds fabricated by solvent-casting/particulate-leaching for tissue engineering. *Plasmaprocesses and polymers*, 2013.**11**(2): p. 184–195.

42. D. Sin *et al.*, Polyurethane (PU) scaffolds prepared by solvent casting/particulate leaching (SCPL) combined with centrifugation. *Materials Science and Engineering C*, 2010. **30**(1): p. 78-85.

43. R. Nazarov, H.J. Jin and D.L. Kaplan, Porous 3-D scaffolds from regenerated silk fibroin. *Biomacromolecules*, 2004. **5**(3): p.718-26.

44. F.J. O'Brien, B.A. Harley, I.V. Yannas and L. Gibson, Influence of freezing rate on pore structure in freeze-dried collagen-GAG scaffolds. *Biomaterials*, 2004, **25**(6): p.1077-86.

45. M.G. Haugh, C.M. Murphy and F.J. O'Brien, Novel freeze-drying methods to produce a range of collagen-glycosaminoglycan scaffolds with tailored mean pore sizes. *Tissue Engineering Part C Methods*, 2010. **16**(5): p.887-94

46. H. Yoshimotoa, Y.M. Shina, H. Teraia and J.P. Vacanti, A biodegradable nanofiber scaffold by electrospinning and its potential for bone tissue engineering. *Biomaterials*, 2003. **24**(12): p. 2077–2082

47. V. Mironov *et al.*, Organ printing: promises and challenges. *Regenerative Medicine*, 2008. **3**(1): p. 93-103.

48. E. A. Roth *et al.*, Inkjet-based bioprinting for high-throughput cell patterning. *Biomaterials*, 2004. **25**(17): p. 3707-3715.

49. C. Xu et al., Scaffold-free inkjet-based bioprinting of three-dimensional zigzag cellular tubes. *Biotechnology and Bioengineering*, 2012. **109**(12): p. 3152-60.

50. Y. Zhang *et al.*, Scaffolds for tissue engineering produced by inkjet-based bioprinting. *Central European Journal of Engineering*, 2012. **2**(3): p. 325-335.

51. S. Khalil and W. Sun, Biopolymer deposition for freeform fabrication of hydrogel tissue constructs. *Materials Science and Engineering: C*, 2007. **27**(3): p. 469-478.

52. J. Malda, T. J. Klein, and Z. Upton., The roles of hypoxia in the in vitro engineering of tissues. *Tissue Engineering*, 2007. **13**(9): p. 2153-2162.

53. I.T. Ozbolat, Y. Yu, Bioprinting towards organ fabrication: challenges and future trends. *IEEE Transactions on Biomedical Engineering*, 2013, **60**(3): p. 1-9.

54. Y. Fang *et al.*, Rapid generation of multiplexed cell cocultures using acoustic droplet ejection followed by aqueous two-phase exclusion patterning. *Tissue Engineering*, 2012. **18**(9): p. 647-657.

55. Demirci U, M.G., Single cell epitaxy by acoustic picolitre droplets. *Lab On A Chip*, 2007. **7**(9): p. 1139-1145.

56. B. Guillotin *et al.*, Laser assisted bioprinting of engineered tissue with high cell density and microscale organization. *Biomaterials*, 2010. **31**(28): p. 7250-7256.

57. S. Catros *et al*., Laser-assisted bioprinting for creating on-demand patterns of human osteoprogenitor cells and nano-hydroxyapatite. *Biofabrication*, 2011. **3**(2): p. 025001.

58. Y. Nahmias *et al.*, Laser-guided direct writing for three-dimensional tissue engineering. *Biotechnology and Bioengineering*, 2005. **92**(2): p. 129-136.

59. D.J. Odde and M.J. Renn, Laser-guided direct writing of living cells. *Biotechnology and Bioengineering*, 2000. **67**(3): p. 312-408.

60. Y. Nahmias and D.J.O., Micropatterning of living cells by laser-guided direct writing: application to fabrication of hepatic-endothelial sinusoid-like structures. *Nature Protocols*, 2006. **67**(3): p. 312-408.

61. S. Tasoglu and U. Demirci, Bioprinting for stem cell research. Trends in *Biotechnology*, 2013. **31**(1): p. 10-19.

62. Y. Zhang, Y. Yu., and I.T. Ozbolat, Direct bioprinting of vessel-like tubular microfluidic channels. *Journal of Nanotechnology in Engineering and Medicine*, 2013. **4**(2): p. 021001.

63. Y. Zhang *et al.*, Characterization of printable cellular micro-fluidic conduits for tissue engineering. *Biofabrication*, 2013. **5**(2): p. 025004.

64. J. O. Hollinger, An Introduction to Biomaterial second ed. 2011: CRC Press, Taylor & Francis Group.

65. D.F.J. Williams. Definictions in biomaterials. In Proceedings of a Consensus Conference of the European Society of Biomaterials. Chester: Elsevier. 1987.

66. N.A. Peppsa, Hydrogels in Medicine and Pharmacy. 1987: Boca Raton, FL: CRC Press.

67. S.V. Murphy, A. Skardal, and A. Atala, Evaluation of hydrogels for bio-printing applications. *Journal of Biomedical Materials Research*, 2013. **101**(1): p. 272-284.

68. R.C. Rowe, P. J. Sheskey, and M. E. Quinn, "Adipic Acid", Handbook of Pharmaceutical Excipients (Rowe, Handbook of Pharmaceutical Excipients) (Sixth ed.). 2009

69. J. Sun and H. Tan, Alginate-based biomaterials for regenerative medicine applications, *Biomaterials,* 2013. 6: p. 1285-1309

70. F. Croisier and C. Jérôme, Chitosan-based biomaterials for tissue engineering. *European Polymer Journal*, 2013. **49**(4): p. 780-792.

71. M. Dash *et al.*, Chitosan—A versatile semi-synthetic polymer in biomedical applications. *Progress in Polymer Science*, 2011. **36**(8): p. 981-1014.

72. J. K. Francis Suh and H. W. T. Matthew, Application of chitosan-based polysaccharide biomaterials in cartilage tissue engineering: a review. *Biomaterials*, 2000. **21**(24): p. 2589-2598.

73. Y. Zhang, H. Chen, and I.T. Ozbolat. Characterization of printable micro-fludic conduits for organ printing. *In International Mechanical Engineering Congress & Exposition (IMECE 2012)*, Nov 9-15, Houston, Texas. 2012.

74. Y. Zhang, Y. Yu, and I.T. Ozbolat. Characterization of vessel-like printable cellular microfluidic conduits. *In Proceedings of Annual Industrial and Systems*

Engineering Research Conference, ISERC 2013, May 18-22, San Juan, Puerto Rico. 2013.

75. W. Lee *et al.*, On-demand three-dimensional freeform fabrication of multi-layered hydrogel scaffold with fluidic conduits. *Biotechnology and Bioengineering*, 2010. **105**(6): p. 1178-1186.

76. Y. Ling *et al.*, A cell-laden microfluidic hydrogel. *Lab on A Chip*, 2007. **7**(6): p. 756-762.

77. M.P. Cuchiara *et al.*, Multilayer microfluidic PEGDA hydrogels. *Biomaterials*, 2010. **31**(21): p. 5491-5497.

78. A. P. Golden and J. Tien, Fabrication of microfluidic hydrogels using molded gelatin as a sacrificial element. *Lab on A Chip*. 2007. **7**(6): p. 720-725.

79. S.-N. Offra *et al.*, Laser photoablation of guidance microconduits into hydrogels directs cell growth in three dimensions. *Biophysical Journal*, 2009. **99**(11): p. 4743-4752.

80. S.H. Lee, J.J. Moon, and J.L. West, Three-dimensional micropatterning of bioactive hydrogels via two-photon laser scanning photolithography for guided 3D cell migration. *Biomaterials*, 2008. **29**(20): p. 2962-2968.

81. V. Chan *et al.*, Three-dimensional photopatterning of hydrogels using stereolithography for long-term cell encapsulation. *Lab on A Chip.*, 2010. **10**(16): p. 2062-2070.

82. L. Wang *et al.*, Prototyping chips in minutes: direct laser plotting (DLP) of functional microfluidic structures. *Sensors and Actuators B: Chemical*, 2012. **168**(20): p. 214-222.

83. C. Hnatovsky et al., Polarization-selective etching in femtosecond laser-assisted microfluidic conduit fabrication in fused silica. *Opt. Lett.*, 2005. **30**(14): p. 1867-1869.

84. V. Mironov, G. Prestwich, and G. Forgacs, Bioprinting living structures. *Journal of Materials Chemistry*, 2007. **17**(20): p. 2054-2060.

85. S.N. Nazhat *et al.*, Controlled microconduitling in dense collagen scaffolds by soluble phosphate glass fibers. *Biomacromolecules*, 2006. **8**(2): p. 543-551.

86. Y. Zhang, Y. Yu, and I.T. Ozbolat. Characterization of printable microfluidic conduits for organ printing. *In Proceedings of 8th ASME Manufacturing Science and Engineering Conference*, June 10-14, 2013, Wisconsin, Madison. 2013.

87. R. Landers *et al*., Rapid prototyping of scaffolds derived from thermoreversible hydrogels and tailored for applications in tissue engineering. *Biomaterials*, 2013. **23**(23): p. 4437-4447.

88. C. M. Cheah *et al*., Automatic algorithm for generating complex polyhedral scaffold structures for tissue engineering. *Tissue Engineering*, 2004. **10**(3): p. 595-610.

89. Z. Fang, B. Starly and W. Sun, Computer-aided characterization of effective mechanical properties for porous tissue scaffolds, *Computer-Aided Design*, 2005. **37**(1): p. 65-72.

90. V. Mironov *et al.*, Organ printing: Tissue spheroids as building blocks. *Biomaterials*, 2009. **30**(12): p. 2164-2174.

91. S. Li et *al*., Direct fabrication of a hybrid cell/hydrogel construct by a double-nozzle assembling technology. *Journal of Bioactive and Compatible Polymers*, 2009. **24**(3): p. 249-265.

92. D.M. Courtman *et al.*, Development of a pericardial acellular matrix biomaterial: biochemical and mechanical effects of cell extraction. *Journal of Biomedical Materials Research*, 1994. **28**(6): p. 655-666.

93. H.W. Sung *et al.*, Fixation of various porcine arteries with an epoxy compound. *Artificial Organs*, 1997. **21**(1): p. 50-58.

94. P.B. Canham *et al*., Medial collagen organization in human arteries of the heart and brain by polarized light microscopy. *Connective Tissue Research*.

95. N. L'Heureux *et al*., A completely biological tissue-engineered human blood vessel. *The FASEB Journal*, 1998. **12**(1): p. 47-56.

96. S.P. Hoerstrup *et al.*, Living, autologous pulmonary artery conduits tissue engineered from human umbilical cord cells. *The Annals of Thoracic Surgery*, 2002.

97. A. Salern *et al*., Processing/structure/property relationship of multi-scaled PCL and PCL–HA composite scaffolds prepared via gas foaming and NaCl reverse templating. *Biotechnology and Bioengineering*, 2011. **108**(4): p. 963-976.

98. B.S. Kim *et al*., Optimizing seeding and culture methods to engineer smooth muscle tissue on biodegradable polymer matrices. *Biotechnology and Bioengineering*, 1998. **57**(1): p. 46-54.

99. I.T. Ozbolat and Y. Yu, Bioprinting toward organ fabrication: challenges and future trends. *IEEE Transactions on Biomedical Engineering* (T-BME), 2013. **60**(3): p. 691-699.

100. D. Seliktar, D. Dikovsky, and E. Napadensky, Bioprinting and tissue engineering: recent advances and future perspectives. *Israel Journal of Chemistry,* 2013. **53**(9-10): p. 795-804.

101. Y. Yu, Y. Zhang, and I.T. Ozbolat, Characterization of cell viability and functionality in bioprintable cellular vessel-like microfluidic conduits. *Journal of Biomechanical Engineering,* 2013. **135**(9): p. 901011-9.

102. R.P. Chhabra and J.F. Richardson, eds. Non-Newtonian Flow and Applied Rheologu. Second Edition 2008.

103. T. Norton, F. Spyropoulos, and P. Cox., Practical food rheology an interpretive approach 2011: Ames, Iowa : Blackwell

104. S.J. Shin *et al.*, "On the Fly" Continuous Generation of Alginate Fibers Using a Microfluidic Device. *Langmuir*, 2007. **23**(17): p. 9104-9108.

105. A.C.F. Ribeiro *et al*., Diffusion coefficients and electrical conductivities for calcium chloride aqueous solutions at 298.15 K and 310.15 K. *Electrochimica Acta*, 2008. **54**(2): p. 192-196.

106. T.R. Cuadros, O. Skurtys, and J.M. Aguilera, Mechanical properties of calcium alginate fibers produced with a microfluidic device. *Carbohydrate Polymers*, 2012. **89**(4): p. 1198-1206.

107. S. Khalil, Deposition and Structure Formation of 3 D Alginate Tissue Engineering. 2006, Drexel University.

108. N.W. Choi *et al*., Microfluidic scaffolds for tissue engineering. *Nat Mater*, 2007. **6**(11): p. 908-915.

109. Y. Zheng *et al.*, In vitro microvessels for the study of angiogenesis and thrombosis. *Proceedings of the National Academy of Sciences*, 2012.

110. R. Gauvin *et al*., Mechanical properties of tissue-engineered vascular constructs produced using arterial or venous cells. *Tissue Engineering*, 2011. **17**(15-16): p. 2049-59.

111. Y. Zhang, Y. Yu, and I.T. Ozbolat, Direct bioprinting of vessel-like tubular microfluidic conduits. *Journal of Nanotechnology in Engineering and Medicine,* 2013. **4**(2): p. 021001.

112. G. Konig *et al*., Mechanical properties of completely autologous human tissue engineered blood vessels compared to human saphenous vein and mammary artery. *Biomaterials,* 2009. **30**(8): p. 1542-1550.

113. M. Francoise *et al.*, Toward engineering functional organ modules by additive manufacturing. *Biofabrication,* 2012. **4**: p. 022001-12.

114. Z. Wang *et al.*, The effect of thick fibers and large pores of electrospun poly(ε-caprolactone) vascular grafts on macrophage polarization and arterial regeneration. *Biomaterials,* 2014. (in press)

115. J.D. Roh *et al.*, Small-diameter biodegradable scaffolds for functional vascular tissue engineering in the mouse model. *Biomaterials,* 2007. **29**(10): p. 1454-1463.

116. C. Wang *et al*., A highly organized three-dimensional alginate scaffold for cartilage tissue engineering prepared by microfluidic technology. *Biomaterials,* 2011. **32**(29): p. 7118-7126.

117. S. Lee *et al*., Fabrication of 3D alginate scaffold with interconnected pores using wire-network molding technique. *Tissue Engineering and Regenerative Medicine*, 2013. **10**(2): p.53-59.

118. S. Khalil *et al*., Bioprinting Endothelial Cells With Alginate for 3D Tissue Constructs. *Journal of Biomechanical Engineering*, 2009. **131**(11): p. 111002

119. M.S. Ikuko *et al*., Evaluation of Three-Dimensional Porous Iron-Cross-Linked Alginate as a Scaffold for Cell Culture, *ISRN Biomaterials*, 2014.

120. C. Ceccaldi *et al*., Alginate Scaffolds for Mesenchymal Stem Cell Cardiac Therapy: Influence of Alginate Composition. *Cell Transplantation*, 2012. **21**(9): p1969-84.

121. M.P. Mattson, R.C. Haddon, and A.M. Rao, Molecular functionalization of carbon nanotubes and use as substrates for neuronal growth. J*ournal of Molecular Neuroscience*, 2000. **14**(3): p. 175-182.

122. H. Hu *et al.*, Chemically functionalized carbon nanotubes as substrates for neuronal growth. *Nano letters*, 2004. **4**(3): p. 507-511.

123. A.O. Lobo *et al*., Cell viability and adhesion on as grown multi-wall carbon nanotube films. *Materials Science and Engineering: C*, 2008. **28**(2): p. 264-269.

124. A. Mazzatenta, M. Giugliano, and S. Campidelli, Interfacing neurons with carbon nanotubes: electrical signal transfer and synaptic stimulation in cultured brain circuits. *Journal of Biomedical Materials Research Pa*rt A 2009. **88**(1): p. 65-73.

125. R. Verdejo *et al.*, Reactive polyurethane carbon nanotube foams and their interactions with osteoblasts. *Journal of Biomedical Materials Research Part A*, 2009. **88**(1): p. 4818-4827.

126. F. Dolati, Y. Yu, Y. Zhang, A. De Jesus, E. Sander, I.T. Ozbolat, In vitro evaluation of carbon-nanotube-reinforced bioprintable conduits, *Journal of Nanotechnology*,2014, **25**(14): p. 145101.

127. Y. Zhang, Y. Yu, F. Dolati, and I. T. Ozbolat, Effect of multiwall carbon nanotube reinforcement on coaxially extruded cellular conduits, *Journal of Materials Science and Engineering: C*, 2014, **39**(1), p. 126-133.

128. I. T. Ozbolat, H. Chen and Y. Yu, Development of 'Multi-arm Bioprinter' for hybrid biofabrication of tissue engineering constructs, *Robotics and Computer-Integrated Manufacturing*, 2014. **30**(3): p. 295-304.

APPENDIX A: CONDUIT SAMPLE PREPARATION PROCEDURE FOR SEM MICROSCOPY

A scanning electron microscope (SEM) obtains images by scanning samples with a focused beam of electrons. An SEM can achieve a resolution of better than 1 nm, depending on the conductivity of samples. Metal samples get the best results. For biosamples or other specimens with low conductivities, special treatments are needed. In addition, because specimens are put in a high vacuum environment, dehydration of the sample is required before loading it into the viewing chamber.

Conduit sample preparation procedures involved dehydration and coating. After fabrication, conduits were soaked in a 4% calcium chloride solution for 12 hours to increase mechanical properties first. Fixed cells, if any, were encapsulated. The cell fixation and dehydration processes are listed below:

1) Cut a long conduit into short sections randomly.
2) Completely rinse cell media off the conduits with PBS (this step is optional; needed only if cells are encapsulated in conduits).
3) Fix cells in conduits at room temperature for 2 hours with SEM fixative. (Optional)
4) Rinse 3 times using the same buffer used for the fixative for 10 minutes each rinse. (Optional)
5) Post-fix for 1 hour in 1% osmium tetroxide in the same buffer. (Optional)
6) Rinse 2 times using the same buffer for 30 minutes each rinse.
7) 25% ethanol – 15 minutes (1 time)
8) 50% ethanol – 15 minutes (1 time)
9) 75% ethanol – 15 minutes (1 time)
10) 95% ethanol – 15 minute (2 times)
11) 100% ethanol – 30 minute (2 times)

12) Chemically dry using HMDS – first time 30 minutes, second time leave bottle open until sample is dry.

After dehydration, the sample was taken out and put on the SEM holding stage. In order to increase signal/noise ratio and improve the picture quality, platinum was coated on top of the sample.

APPENDIX B: VALUES OF Λ

Table B.1

Values of λ, which locates the position at which the velocity is at its maximum

n	Value of σ								
	0.10	0.20	0.30	0.40	0.50	0.60	0.70	0.80	0.90
0.10	0.3342	0.4687	0.5632	0.6431	0.7140	0.7788	0.8389	0.8954	0.9489
0.20	0.3682	0.4856	0.5749	0.6509	0.7191	0.7818	0.8404	0.8960	0.9891
0.30	0.3884	0.4991	0.5840	0.6570	0.7229	0.7840	0.8416	0.8965	0.9492
0.40	0.4052	0.5100	0.5912	0.6617	0.7259	0.7858	0.8426	0.8969	0.9493
0.50	0.4193	0.5189	0.5970	0.6655	0.7283	0.7872	0.8433	0.8972	0.9493
0.60	0.4312	0.5262	0.6018	0.6686	0.7303	0.7884	0.8439	0.8975	0.9494
0.70	0.4412	0.5324	0.6059	0.6713	0.7319	0.7893	0.8444	0.8977	0.9495
0.80	0.4498	0.5377	0.6093	0.6735	0.7333	0.7902	0.8449	0.8979	0.9595
0.90	0.4572	0.5422	0.6122	0.6754	0.7345	0.7909	0.8452	0.8980	0.9495
1.00	0.4637	0.5461	0.6147	0.6770	0.7355	0.7915	0.8455	0.8981	0.9596

Source: R.P. Chhabra and J.F. Richardson, eds. Non-Newtonian Flow and Applied Rheologu. Second Edition 2008.

APPENDIX C: MEASUREMENT OF FLOW RATE AND PRESSURE GRADIENT

Table C.1

Dispensing rheology: flow rate and pressure gradient of 3% alginate solution

Pressure (psi)	Average Flow Rate (ml/second)			*-ΔP/L*		
	G 16-23	G 16-23	G 18/25	G 18-23	G 18-25	G 18-25
0	0	0	0	0	0	0
1	0.020	0.010	0.002	145081513.8	242076682.6	471846287.5
2	0.046	0.025	0.004	272476077.7	485721542.7	975394465
4	0.140	0.060	0.012	636629250.7	944817457.9	2115306187
6	0.247	0.110	0.02	948289522.3	1497653686	3410783916
8	0.320	0.175	0.003	1193282483	2131384858	4598152164
10	0.400	0.230	0.045	1413822455	2623409667	5776130586

APPENDIX D: SHEAR STRESS VALUE OF DIFFERENT LOCATIONS INSIDE COAXIAL NOZZLE TIP

Table D.1

Shear stress inside coaxial nozzle (G 16-23)

	shear stress		
r	5 psi	10 psi	20 psi
0.470588	-69846.7	-94377.7	-169586
0.490588	-63303.7	-85537.2	-153701
0.510588	-57125.8	-77189.5	-138701
0.530588	-51271.5	-69279	-124487
0.550588	-45705.5	-61758.1	-110973
0.570588	-40397.5	-54585.8	-98084.7
0.590588	-35321.2	-47726.7	-85759.5
0.610588	-30453.9	-41149.9	-73941.8
0.630588	-25775.7	-34828.6	-62583.2
0.650588	-21269.2	-28739.4	-51641.5
0.670588	-16919	-22861.3	-41079.2
0.690588	-12711.5	-17176.1	-30863.5
0.710588	-8634.74	-11667.4	-20965.1
0.730588	-4677.88	-6320.84	-11357.9
0.750588	-831.387	-1123.39	-2018.6
0.770588	2913.347	3936.769	7073.582
0.790588	6564.04	8869.454	15937.44
0.810588	10127.65	13684.68	24589.86
0.830588	13610.48	18390.73	33046.13
0.850588	17018.21	22995.33	41320.08
0.870588	20356.03	27505.45	49424.28
0.890588	23628.65	31927.47	57370.16
0.910588	26840.35	36267.19	65168.16
0.930588	29995.08	40529.91	72827.81
0.950588	33096.72	44720.5	80357.83
0.970588	36147.67	48843.42	87766.26
0.990588	39151.88	52902.75	95060.44
1	40550.15	54792.12	98455.42

APPENDIX E: PRINTING PLAN CALCULATION

For a square network with width W shown in figure E.1, the printing structure comprises two parts, straight conduits and U-turn curvature. As stated previously, the distance between conduits is l^*, and the outer radius and the inner radius of the curvature (as shown in Figure E.1) can be calculated as follows:

$$R = \frac{l^* + D_O}{2} \tag{E.1}$$

$$r = \frac{l^* - D_O}{2} \tag{E.2}$$

Thus, the length of the straight conduits can be calculated as:

$$L_{straight} = W - 2R = W - (l^* - D_O) \tag{E.3}$$

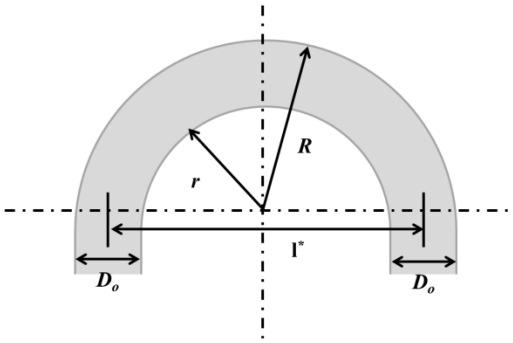

Figure E.1

U-turn curvature.

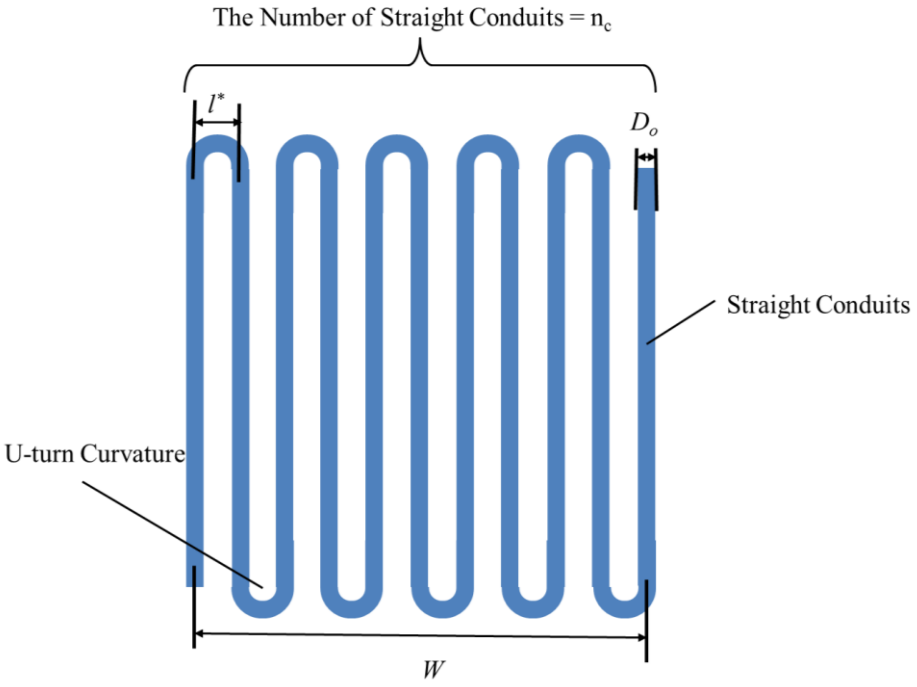

Figure E.2

One layer of conduit network.

As shown in Figure E.1, the number of straight conduits is n_c, thus the length of all the straight conduits is as $n^* L_{straight}$. The length of every curvature is half the perimeter of a circle with a radius of l^*. In total, the number of curvature in each layer is n_c -1. Thus, the length of a vasculature network can be calculated as:

$$n_c\left(W-\left(D_0+l^*\right)\right)+\left(n_c-1\right)\frac{\pi l^*}{2} \tag{A.4}$$

Appendix F: FACTORIAL DESIGN RESULT

Table F.1

Factorial design result and predicted gelation time

	Factors					*Results*			
Run Order	X_1	X_2	X_3	X_4	X_5	Conduit Diameter (μm)	Lumen Diameter (μm)	Wall Thickness (μm)	Gelation Time (min)
1	4	4	6	3	540	1322.29	439.57	441.36	6.78
2	4	4	3	2	540	1283.19	460.67	411.26	5.98
3	4	4	3	3	190	947.21	736.81	210.49	1.48
4	4	4	6	2	190	835.40	360.73	237.34	2.37
5	4	5	3	3	540	1106.70	678.39	213.96	3.18
6	4	5	6	2	540	1424.47	253.24	585.61	8.19
7	4	5	6	3	190	1021.82	364.92	328.45	3.80
8	4	5	3	2	190	736.77	155.49	290.49	2.16
9	3	4	3	3	540	1665.31	385.71	639.80	10.94
10	3	4	6	2	540	1753.78	378.15	687.82	12.22
11	3	4	6	3	190	976.70	457.98	259.26	3.10
12	3	4	3	2	190	845.24	467.86	188.69	2.06
13	3	5	6	3	540	1579.85	317.63	631.11	9.98
14	3	5	3	2	540	1303.04	330.43	486.70	6.72
15	3	5	3	3	190	983.85	409.15	287.35	3.34
16	3	5	6	2	190	957.30	312.60	322.35	3.41